UNIVERSITY OF SOUTHAMPTON

# Modification of glasses and optical waveguides using high electric fields

by

francesco paolo mezzapesa

A thesis submitted in partial fulfillment for the
degree of Doctor of Philosophy

in the
Faculty of Engineering, Science and Mathematics
Optoelectronics Research Centre

May 2007

UNIVERSITY OF SOUTHAMPTON

ABSTRACT

FACULTY OF ENGINEERING, SCIENCE AND MATHEMATICS
OPTOELECTRONICS RESEARCH CENTRE

Doctor of Philosophy

by francesco paolo mezzapesa

This thesis describes work done towards establishing efficient and reproducible second harmonic generation in thermally poled novel high-index bismuth-borate glass structures. According to the rectification model, glass with higher $\chi^{(3)}$ values than silica would permit $\chi^{(2)}$ to scale up proportionally, for a given frozen-in electric field strength. The fundamental research on poling induced nonlinearity has been extended to investigate several compositions of $Bi_2O_3ZnOB_2O_3$ glass systems, whose refractive index is measured to increase with the $Bi_2O_3$ content. Intrinsic third-order optical nonlinearity $\chi^{(3)}$ up to thirty times higher than silica have been measured in bismuth-based compounds, and even larger values are potentially achievable.

In this thesis, a reliable procedure to induce large and stable second order nonlinear coefficient $\chi^{(2)}$ in bismuthate glasses has been established along with the understanding towards efficient generation of second harmonic power in waveguiding layers. Characterization methods to determine the nonlinear formation dynamics and resolve nonlinear thickness and profile has been optimized to quantify the magnitude and distribution of second order nonlinearities in thermally poled bismuthate glasses. The development of a new poling procedure, where the applied voltage is varied during the cooling phase, instead of being kept constant, has allowed a record value of $\chi^{(2)} = 2.3\,pm/V$ in 12.5% $Bi_2O_3$ bulk samples to be achieved. The control of nonlinear region evolution gained by establishing the innovative time-varying voltage poling procedure has led to the first demonstration of second-order nonlinearity value as high as $2\,pm/V$ induced by thermal poling in bismuthate sputtered slab waveguides.

These achievements opened new investigations towards realizing efficient monolithic structures leading to high performance active devices based on poled bismuth-based glass waveguides. In particular, an all-glass electro-optic modulator and a frequency doubler have been targeted, based on sputtering and femtosecond laser direct writing, respectively.

# Contents

# List of Figures

# List of Tables

# Acknowledgements

I would like to start the acknowledgments with a warm GRAZIE to all people at the ORC, people I have been working with, who shared with me their know-how gained in years of experience in the field. I am extremely grateful to my supervisors, James and Peter, Isabel and Costa for their indispensable support to the project, the integrated-optics and poling groups for deep and inspiring discussions. Many thanks to Dave Sager, Neil and all 'workshop guys' for introducing me to sample fabrication and processing. Together with them I expecially thank people I have been collaborating with, Koichi and the NSG, Albert, Weijia, Katia, Marco among others, Olivier Deparis, George Chen, the research group of the Prof. Gomes in Brasil. At the Universite des Sciences et Technologies in Lille, I had a very fruitful collaboration with Alexander Kudlinski, Yves Quiquempois and Gilbert Martinelli, whom I would like to thank for experimental support and scientific discussion. Thanks to Walter Margulis and Dave Shepherd for careful reading of the present thesis.

Of course I cannot leave out George, Rob, Marty, Paulo, Daniel, and whoever has contributed to the recreational and mentally stimulating opportunities which this enjoyable adventure has given me. Finally, I wish to thank Lucia, my family and Lorenzo for invaluable support in every way.

*Thanks to you all folks for making my albionic experience so absolutely amazing!!*

# *Declaration of Authorship*

*I, francesco paolo mezzapesa, declare that the thesis entitled 'Modication of glasses and optical waveguides using high electric fields' and the work presented in it are my own. I confirm that:*

- *this work was done wholly while in candidature for a research degree at this University;*
- *where any part of this thesis has previously been submitted for a degree or any other qualification at this University or any other institution, this has been clearly stated;*
- *where I have consulted the published work of others, this is always clearly attributed;*
- *where I have quoted from the work of others, the source is always given. With the exception of such quotation, this thesis is entirely my own work;*
- *I have acknowledged all main sources of help;*
- *where the thesis is based on work done by myself jointly with others, I have made clear exactly what was done by others and what I have contributed myself;*
- *parts of this work have been published as shown in the List of Publications;*
- *due to the uncontrollable loss of fabrication and characterization facilities, a complete analysis of the poled Mach-Zehnder interferometer (Chapter 6) was not possible.*

*Signed: .....*

*Date: .....*

# *List of Publications*

- *A.S.L. Gomes, E.L. Falco Filho, C.B. de Arajo, D. Rativa, R.E. de Arajo, K. Sakaguchi, F.P. Mezzapesa, I.C.S. Carvalho, and P.G. Kazansky. Third-order nonlinear optical properties of bismuth-borate glasses obtained by conventional and thermally managed eclipse Z-scan. J. Appl. Phys., 101(033115), 2007.*

- *F.P. Mezzapesa, I.C.S. Carvalho, P.G. Kazansky, O. Deparis, M. Kawazu, and K. Sakaguchi. Bleaching of sol-gel glass film with embedded gold nanoparticles by thermal poling. Appl. Phys. Lett., 89(183121), 2006.*

- *I.C.S. Carvalho, F.P. Mezzapesa, P.G. Kazansky, O. Deparis, M. Kawazu, and K. Sakaguchi. Dissolution of embedded gold nanoparticle in sol-gel glass film. Materials Science and Engineering C, EMRS 2006 Symposium A, ID 107SL, 2006.*

- *T.R. Oliveira, L. de S. Menezes, E.L. Falcao-Filho, A.S.L. Gomes, Cid B. de Arajo, K. Sakaguchi, F.P. Mezzapesa, I.C.S. Carvalho, and P. G. Kazansky. Optical limiting behavior of bismuth oxide-based glass in the visible range. Appl. Phys. Lett., 89 (211912), 2006.*

- *A. Canagasabey, F.P. Mezzapesa, C. Corbari, P.G. Kazansky, and M. Ibsen. 75% enhancement of the second order nonlinearity in twin-hole fibres through voltage assisted cooling during poling. Proc. CLEO, 2006.*

- *F.P. Mezzapesa, I.C.S. Carvalho, C. Corbari, P.G. Kazansky, J.S. Wilkinson, and G. Chen. Voltage-assisted cooling: a new route to enhance $\chi^{(2)}$ during thermal poling. Proc. CLEO, 1(1):408410, 2005.*

- *O. Deparis, F.P. Mezzapesa, C. Corbari, P. G. Kazansky, and K. Sakaguchi. Enhancing the second-order optical nonlinearity induced in bismuthate glasses by thermal poling. Proc. LEOS Benelux, 2005.*

- *O. Deparis, F.P. Mezzapesa, C. Corbari, P. G. Kazansky, and K. Sakaguchi. Origin and enhancement of the second-order non-linear optical susceptibility induced in bismuth-borate glasses by thermal poling. J. Non-Cryst. Sol., 351(36):21662177, 2005.*

- *F.P. Mezzapesa, C. Corbari, O. Deparis, P.G. Kazansky, and J.S. Wilkinson. Second-order nonlinearity profile in thermally poled twin-hole fibre. Proc. CLEO, 2004.*

# Chapter 1

# Introduction

## 1.1 Optical nonlinearity in glass-based active devices

Unlike their related quartz crystalline phase, amorphous glass media display inherent lack of second order optical nonlinearity ($SON$) which has prevented their wide-spread use as active photonic components, such as electro-optic modulators, memory, switches, wavelength converters, parametric oscillators and electrically tunable Bragg gratings, which would ideally be monolithically integrated with the available silica-based technology. However, glass guarantees good interfacing to planar waveguides and fibers and can also be readily fabricated in any shape. Its thermal stability, heat resistance and high damage threshold are some advantages with respect to nonlinear polymers, easily adaptable to optical devices. The superiority as an optoelectronic material compared to single crystals and polycrystals lies in the fact that glass-based devices show excellent optical properties, such as isotropy, high transmittance in a broad wavelength range, ultralow linear optical losses, short cut-off wavelength, low manufacturing cost. However, their main drawback is a macroscopic inversion symmetry, which in turn forbids any even nonlinear process.

Extensive scientific and commercial interest has been devoted over the last two decades to the development of a reliable procedure to induce a large and stable $SON$ coefficient $\chi^{(2)}$ in centro-symmetric materials. It was initially discovered that a frequency broadening could be measured in optical fibers due to self-phase-modulation (Stolen and Lin, 1978). Fujii et al. (1980) reported that a second order nonlinear grating could be photo-induced in a silica fibre if a high power pump beam was launched into the fibre along with a much weaker second-harmonic ($SH$) seed. Osterberg and Margulis (1986) demonstrated self-generated grating nonlinearity as high as $\approx 10^{-4} - 10^{-3} pm/V$ in Ge-doped silica fibre pre-treated by an optical field. Using $1064\,nm$ pump light with input intensities of $100 - 200\,GW/cm^2$, the authors found conversion efficiencies as high as 5% in silica fibre less than one meter long after $532\,nm$ harmonic light had built up over many hours.

The interaction between the intrinsic third order susceptibility $\chi^{(3)}$ and the static field, spatially modulated along the fibre by the photogalvanic effect, was claimed to break the glass matrix symmetry and generate the $SH$ signal (Dianov et al., 1989). Stolen and Tom (1987) proposed that the $SHG$ was due to electric-field induced nonlinearity in which the field arose from a third-order optical rectification process, as described in Section 2.3.1. Although Bergot et al. (1988) demonstrated large permanent enhancements in the second order optical nonlinearity in germanosilicate fibre by application of a transverse $DC$ electrical poling field in the presence of high-intensity light, $SHG$ signals in silica fibre exhibited $SON$ levels typically three to four orders of magnitude lower than in nonlinear crystals such as $LiNbO_3$. In 1991, however, Myers et al. (1991) managed to induce a second order nonlinear coefficient $\chi^{(2)}$ as high as $1\,pm/V$ into bulk commercial fused-silica by means of the thermal poling treatment. During this poling process, silica-based devices, being bulk, fibre or planar waveguide, were subjected to a strong field while simultaneously excited by heat (Kazansky and Russell, 1994). Other suitable perturbations such as $UV$ light irradiation (Fujiwara et al., 1995) were also applied. Corona (Okada et al., 1992), all-optical (Lopez-Lago et al., 2001) and electron-beam implantation poling (Liu et al., 2001) were also proposed in the literature. Nevertheless, none of the latter techniques seems at the moment as reliable as thermal poling, which has been proved to be the most successful in creating stable nonlinearity in glass among the available methods. Although a $SON$ approaching $25\,pm/V$ has been reported for $UV$ poled Ge-doped silica (Khaled et al., 2000), this value has still to be reconfirmed and anyway does not match the largest coefficient of the $SON$ in $LiNbO_3$, which is $\chi^{(2)}_{33} = 82\,\mathrm{pm/V}$ (Boyd, 1992).

The relevant research advances carried out on poling glass are briefly reviewed in this chapter in order to provide a guideline toward the development of silica-based devices with non-zero second order nonlinearity. In the next section a brief review on $\chi^{(2)}$ formation is presented, with a particular emphasis on what is still limiting the $\chi^{(2)}$ peak value in silica and what strategy is adopted throughout this thesis to enhancing it.

### 1.1.1 $\chi^{(2)}$ induced by thermal poling

Since Myers' demonstration of $1\,pm/V$ by thermal poling (Myers et al., 1991), achieving a further increase of the nonlinearity in glass material has become a priority, along with clarifying the physical origin and mechanism behind poling, which remain not fully understood.

Various studies have explored the evidence of a relationship between $SON$ appearance and alterations in the matrix of the glass. Interesting results were achieved when the thermal poling procedure was combined with the exposure of the sample to a variety of light sources. Among others, Corbari et al. (2002) demonstrated thermal poling of silica glass modified by femtosecond laser irradiation. The author speculated that local

multiphoton absorption process would induce permanent structural modifications (i.e. volume defects) whose orientation could contribute to the second-order susceptibility. Furthermore, ultraviolet laser pulses (Kameyama et al., 2002) and x-ray radiation before poling (Kameyama et al., 1997) were shown to introduce and destroy point defects which acted as active sites in the generation of second-order optical nonlinearities in high-purity silica glasses ($\chi^{(2)} \cong 0.5\,pm/V$). As a confirmation, no $SHG$ could be observed when high-purity silica was conventionally poled. The characteristics of the generation process depended not only on the $(= Si - OH)$, $O_2$, and $H_2$ contents of the glass, which are introduced during the synthesis process, but also on the sequence of thermal poling and pulse irradiation. Similarly, a second-order optical nonlinearity as large as $\chi^{(2)} \cong 0.71\,pm/V$ was generated in synthetic silica glasses by a thermal poling procedure following KrF excimer laser exposure (Kameyama et al., 2001).

However, the state of the art of understanding thermal poling in silica glass is that the second order nonlinearities are essentially due to the creation of a frozen-in space charge distribution (Kazansky et al., 1996), strongly supported by evidence of nonlinearity in a thin layer underneath the glass surface (Alley and Brueck, 1998). Thermally activated conductivity of glass is well known in solid-state ionics and has been studied in various $SiO_2$ systems (Alley et al., 1998). When a high static field is applied to the glass at elevated temperatures, "impurity" ions are believed to drift toward the cathode where they are neutralised by incoming electrons, leaving behind them a negatively charged depletion region near the anodic surface. The depletion region moves deeper into the glass as the ion migration proceeds further. To visualize how this works, a simplified picture of the space charge dynamics is shown in Figure 1.1.

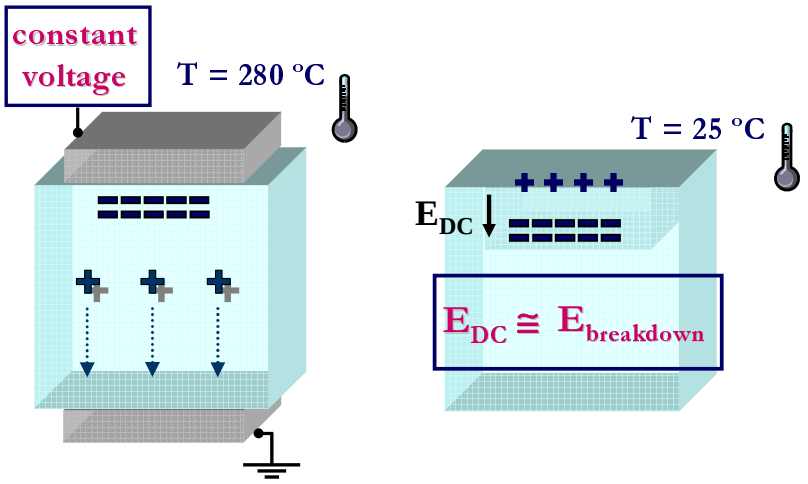


FIGURE 1.1: Mobile charge carriers in thermally poled silica. $\chi^{(2)}$ is located in a thin layer underneath the anodic surface where a permanent built-in electric field, $E_{DC}$, is induced by charge migration.

During poling, a charge distribution layer is created underneath the anodic surface across which the voltage, $V$, drops. When the glass is cooled with the voltage still applied, the

ions freeze in their positions and an electrostatic field, $E_{DC}$, is thus stored in the glass depth, whose peak value ($E_p$ in Figure 1.2) is much higher than $E_0$, the uniform field in the absence of charge motion.

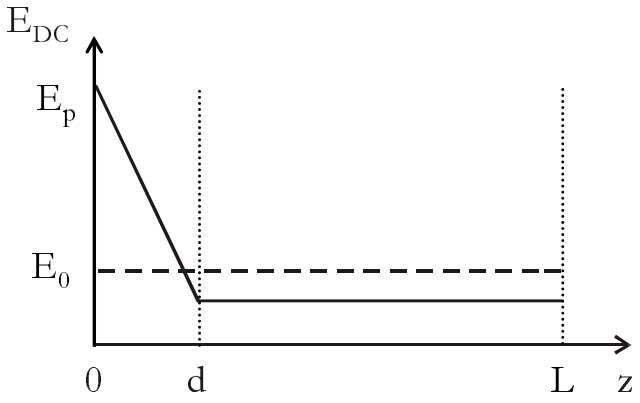


FIGURE 1.2: The depth distribution of the electric field during poling (*solid line*) and the uniform field distribution $E_0 = V/L$ in the absence of charge motion (*dotted line*) through the sample length, $L$, are sketched in a simplified picture of the poling process. The charge front, $d$, separates the depletion region and the neutral region.

At the steady state, the electric-field distribution $E_{DC}(z)$ is assumed to follow the zero-potential condition (Quiquempois et al., 2005a):

$$\int_0^L E_{DC}(z)dz = 0 \tag{1.1}$$

where $L$ is the total thickness of the sample and $z$ is the position across it. The intrinsic third-order nonlinear susceptibility of the glass would then be rectified by such a built-in electrostatic field, according to:

$$\chi^{(2)} \propto \chi^{(3)} E_{DC} \tag{1.2}$$

to induce a non-vanishing second-order nonlinear susceptibility. The induced nonlinearity is located underneath the glass surface in contact with the anodic surface, in the thin space-charge layer left by ion migration. In principle, under the action of this artificially frozen-in field the orientation of dipoles may also take place. However there are indications that such a contribution to the nonlinearity is negligible in thermally poled glass (Kazansky and Russell, 1994), as explained in Section 2.3.

### 1.1.2 Intrinsic limit of $\chi^{(2)}$ in silica

Poled glass is an attractive material for practical application in optical communications and integrated optics allowing use of second-order nonlinear optical effects, such as electro-optic ($EO$) modulation and second-harmonic generation. In thermally poled

silica-based devices, the rectification of the intrinsic third-order nonlinear optical susceptibility $\chi^{(3)}$ by the electrostatic field recorded in the glass, accounts for the major part of the induced second-order nonlinearity. The nonlinearity is spatially confined in a few micron thick layer beneath the anodic surface, a feature that is compatible with planar waveguide designs and optical fibre geometries. However, the frozen-in field mechanism described in Section 1.1.1 sets an upper limit to $\chi^{(2)}$ values achievable for a given glass compound. The limit is given by the dielectric breakdown strength of the material.

Taking in account that $\chi^{(3)}$ in silica is $2 \times 10^{-22}\,\mathrm{m^2/V^2}$ (Adair et al., 1987) and Alley et al. (1998) measured its dielectric breakdown strength being $\approx 2\times10^9\,V/m$, $\chi^{(2)}$ values up to $\sim 1\,pm/V$ would be predicted by Equation 1.2, as indeed measured in poled fused silica. The massive interest aroused in the scientific community by thermal poling in glass is thus explained, as the figure of $1\,pm/V$ is comparable with widely used frequency doubler nonlinear crystals. As a comparison, the values of the $SON$ susceptibility tensor elements reported for KDP are $\chi^{(2)}_{14} = 1\,pm/V$ and $\chi^{(2)}_{36} = 0.92\,pm/V$, for quartz $\chi^{(2)}_{11}$ is $0.6\,pm/V$ (Hagimoto and Mito, 1995) and finally beta barium borate (BBO) has a $\chi^{(2)}_{11}$ equal to 3.8 pm/V.

Research carried out to increase the value of second order nonlinearity induced by poling in silica is reported in this thesis. According to the rectification mechanism in Equation 1.2, high-index glass systems are promising candidates towards engineering efficient prototypes of all-glass $EO$ modulator and frequency converter. In particular, several compositions of bismuth-borate glasses are chosen for investigation, whose refractive index is predicted to scale with the bismuth oxide content, thus offering $\chi^{(3)}$ values up to two order of magnitude higher than silica.

This study has included the development of a new poling procedure (Mezzapesa et al., 2005), where the voltage is varied during the cooling phase, instead of keeping it constant. In this way, control of the nonlinear region evolution is gained by modifying the standard constant-voltage poling procedure. This feature provides benefits for the integration of nonlinearity in waveguiding regions, as verified in poled twin-hole fibres. Moreover, the frozen-in electric field measured in both Herasil and Infrasil samples exhibits significant enhancement in comparison with the traditional procedure, for identical conditions at the start of it. Finally, evidence of in-built $\chi^{(2)}$ strengthening is also demonstrated in bismuthate compounds, in which a second order nonlinearity peak value $\chi^{(2)} = 2.3\,pm/V$ is reported.

In summary, the $\chi^{(2)}$ value so far recorded in silica is intrinsically limited by the dielectric breakdown point of the material. According to Equation 1.2, glasses with higher $\chi^{(3)}$ values than silica would in theory permit $\chi^{(2)}$ to scale up proportionally. Diverse solutions are currently under study by the thermal poling community and vast effort is made in the attempt to increase the second order susceptibility in glass based devices.

The strategy for achieving $\chi^{(2)}$ values as high as $5 - 10\,pm/V$ in thermally poled glass is based on two complementary approaches:

- to increase the frozen-in field
- to increase the $\chi^{(3)}$ of the glass

In the next section, the approach adopted in the present thesis is outlined.

### 1.1.3 Strategy to enhance $\chi^{(2)}$ in glass

The historical background of thermal poling given in the previous section is the foundation of our main research target and provides a starting point toward enhancing $\chi^{(2)}$. Bearing in mind the charge migration model introduced in Section 1.1.1, a glass candidate to improve the $\chi^{(2)}$ values should be chosen with accurate knowledge of ion mobility and any electronically polarizable entities in the system. Furthermore, the rectification model (Equation 1.2) suggests that $\chi^{(2)}$ would increase in proportion to the third order nonlinear coefficient, provided that a permanent electrostatic field of sufficiently high strength could be built in high-index glasses; ideally, $E_{DC}$ should be at least of the same order of magnitude as that induced in silica. The linear and third-order nonlinear optical susceptibilities $\chi^{(1)}$ and $\chi^{(3)}$ are related to each other, in *esu* units, according to the Miller's rule (Boyd, 1992):

$$\chi^{(1)} = \frac{n^2 - 1}{4\pi} \tag{1.3}$$

$$\chi^{(3)} = \left[\chi^{(1)}\right]^4 \cdot 10^{-10} \tag{1.4}$$

where $n$ is the refractive index. For the sake of clarity, $\chi^{(x)}_{SI}/\chi^{(x)}_{esu} = 4\pi/(10^{-4} \cdot c)^{(x-1)}$, where $x$ is the susceptibility order and $c$ the speed of light.

It is expedient to define the $\chi^{(3)}$ enhancement factor, $\Phi$, as the ratio given by:

$$\Phi = \frac{\chi^{(3)}}{\chi^{(3)}_s} = \left[\frac{n_h^2 - 1}{n_s^2 - 1}\right]^4 \tag{1.5}$$

where $\chi^{(3)}_s$ is the third order susceptibility in silica, $n_h$ and $n_s$ are the refractive indexes of high-index glass and silica, respectively. It follows that an increase in $\chi^{(3)}$ of two orders of magnitude is predicted for glasses which have a refractive index equal to 2.1, as illustrated in Figure 1.3. As a consequence, research on thermal poling is progressively

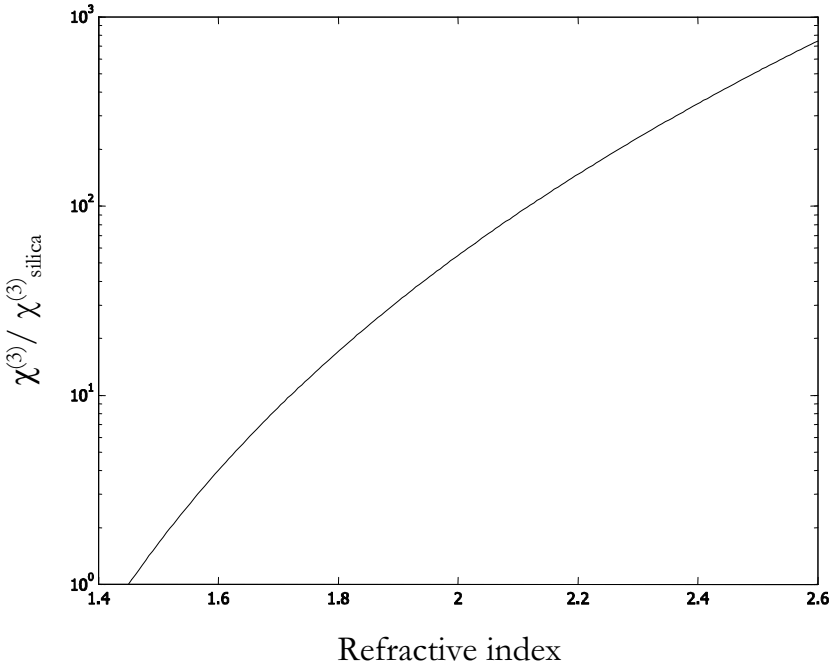


FIGURE 1.3: $\chi^{(3)}$ enhancement factor (with respect to silica) as a function of refractive index of high-index glasses. The refractive index of silica is taken equal to $n_s = 1.45$

moving from silica-based to high-index glass systems. However, these higher second-order nonlinearities have not yet materialized and the experimental procedures to pole high-index glass systems are often different from silicate compounds.

In the literature, poling treatment on soft glass ($BK7$) confirmed the generation of bulk and near-surface second-order nonlinearity for longer poling time and higher temperature than silica (Qiu et al., 2002). In particular, the saturation time was $\approx 43\,h$ for a $d_{33}$ value of $0.2\,pm/V$. However, the authors reported the occurrence of temporal decay of $SON$, which could be reduced but not eliminated by poling at lower temperature. Although the decay of $\chi^{(2)}$ is intrinsically related to the poling mechanism, as it relies on thermally activated migration of ions, high thermal stability is crucial for applications of poled glasses. $\chi^{(2)}$ stability strongly depends on the glass chemical composition (Deparis et al., 2004a): in soft glass, an inference could be drawn to connect this to either the loss rate of charges owing to the glass electric conductivity or the rate of the charge escape from traps at room temperature.

Xu et al. (2000b) reported a detailed investigation of thermally poled heavy-metal glass. Their experimental results on $PbO/B_2O_3$ revealed a second harmonic signal coming from both near-surface and bulk regions, which was in turn strongly influenced by the negative charge layer frozen in the anodic area. The calculated nonlinear coefficient near the edge of anode side was $d_{eff} = 0.04\,pm/V$, less than that induced in silica, whose nonlinear depth is in turn 10-fold smaller than in these borate glasses. Furthermore, the maximum second-harmonic intensity was obtained at different optimal poling temperature ($T_p$)

for each different glass composition (Xi et al., 2002). Clear evidence of a relationship between $T_p$ and $T_g$, the glass transition temperature, was also reported.

Such a correlation was also revealed by Tanaka et al. (2000a) in poled $TeO_2$-based glasses, highly attractive for their optical third-order nonlinear susceptibility ($\chi^{(3)} \cong 10^{-12} esu$, larger by two orders of magnitude than silica) as well as their wide wavelength range of gain as optical amplifiers. The induced second-order nonlinearity in poled $30ZnO \cdot 70\,TeO_2$ glass exhibited a peak value of $\chi^{(2)} \cong 2.1\,pm \cdot V^{-1}$ (Tanaka et al., 2000a) and the relaxation time for its decay was measured to follow the Arrhenius dependence and was found to be as long as 9 years at room temperature (Narazaki et al., 1999). Surface structure modifications and relaxation phenomena were also investigated on thermally poled $20WO_2 \cdot 80\,TeO_2$ (Narazaki et al., 2002) and $15Nb_2O_5 \cdot 85TeO_2$ glasses (Tanaka et al., 2000b). In the latter, x-ray photoelectron spectroscopy ($XPS$) unexpectedly revealed penetration of $Na^+$ into the anode-side surface of the sample, kept sandwiched between two commercial borosilicate glass wafers throughout poling. The authors concluded that the incorporation of $Na^+$ not only lowered the glass transition temperature of the anode-side surface, allowing $Nb^{5+}$ migration from the anode-side surface into the bulk as well, but was responsible for the decay of second harmonic intensity after poling. Qiu et al. (1999b) had previously attempted to dope the anodic face of high purity pieces of silica with sodium ions and verified that the neutralization of the accumulated negative charges with the injected $Na^+$ caused a decreasing of the $SH$ signal.

In summary, the response of these novel glasses to the poling treatment is reported to differ significantly from that of silicon dioxide, depending on the ions at work, their mobility and their concentrations. Moreover, their dielectric breakdown strengths seem to be lower than expected, likely because of their higher electrical conductivity, the latter inhibiting a permanent space charge to freeze into their matrix. These factors contribute to make the strategy of raising the values of $\chi^{(2)}$ a complex and interesting task.

### 1.1.4 Scope of the thesis

Thermal poling of new high-index glass compounds plays a key role in this thesis project towards realizing efficient all-optical active devices. In particular, $\chi^{(2)}$ peak values higher than silica are demonstrated in bismuth-borate glass systems $Bi_2O_3ZnOB_2O_3$, in which $\chi^{(3)}$ increases with increasing $Bi_2O_3$ content, as detailed in Chapter 4. Highly nonlinear optical-guiding media have been widely employed for all-optical signal processing applications. Bismuthate glasses are experiencing growing commercial interest owing to not only their inherently high nonlinear refractive index, but also their good mechanical, chemical and thermal stability, which allows preform fabrication for low-loss fibre drawing (Ebendorff-Heidepriem et al., 2005). Moreover, Ohara et al. (2003) reported high power and high conversion efficiency amplifiers using fusion-spliceable $Bi_2O_3$-based

erbium doped fibre. Among the high-nonlinearity compound glasses, bismuthate glass has the additional advantage of not containing toxic elements such as $Pb$, $As$, $Se$ and $Te$.

An overview of the main achievements is reported, along with a detailed history of the work to guarantee experimental reproducibility through careful optimization of both glass composition and poling conditions. A conductivity model is also proposed, indicating that the high electronic conductivity of bismuthate glass may be responsible for the induced nonlinearity value being lower than expected. By taking into account ion injection and glass ionization, a poling mechanism is finally suggested which relies on proton migration (Deparis et al., 2005b). The know-how acquired during this initial research led to a preliminary study of thermal poling in thin dielectric films with high third-order susceptibility, which has already been verified as promising approach in $WO_3$-$TeO_2$ (Tanaka et al., 2000a) and in $As_2S_3$ chalcogenide glass thin films (Quiquempois et al., 2000b). A peak second order susceptibility $\chi^{(2)} \cong 2\,pm \cdot V^{-1}$ was generated in an asymmetric bismuth-based slab waveguide on top of a borosilicate substrate, showing the feasibility of developing competitive electro-optic modulators. Moreover, efficient poling was performed on waveguiding channels written by femtosecond pulses in bismuthate bulk samples: this achievement is at the basis of the demonstration of integrated wavelength converter devices.

Finally, as a further investigation on materials with high third-order nonlinearity, poling of nanocomposite silicate glass was investigated. In particular, higher $\chi^{(2)}$ values are expected through a resonant enhancement of $\chi^{(3)}$ close to the surface plasmon resonance of gold nanoparticles randomly distributed in a low conductivity sol-gel glass film on a soda-lime glass substrate (Mezzapesa et al., 2006). Although no $SHG$ was measured, the electric-field-assisted dissolution of gold nanoparticles was demonstrated, broadening the application of thermal poling in optical device fabrication.

## 1.2 Thesis outline

This thesis is intended to provide a comprehensive account of the nonlinear phenomena induced in glass materials by thermal poling. Broadly speaking, Chapters 1-3 describe the background to the the research and Chapters 4-7 describe the main original contributions.

Chapter 2 provides an essential insight into the context of the nonlinear optics along with a broad overview of the historical background in which thermal poling has developed. The most plausible explanations of the mechanism behind the $SON$ formation in glass are also reported. Finally, the discussion focuses on how poling-induced nonlinearity may be employed to realize competitive integrated all-optical guiding circuits.

Chapter 3 examines more closely the characterization methods adopted to measure the poling induced nonlinearity. A comparison of the results obtained when three different techniques are employed yields accurate knowledge of the thickness, profile and dynamics of thin nonlinear regions. The procedure emphasizes the need to quantify these critical parameters which characterize the poling process, in order to engineer efficient active glass-based devices.

Chapter 4 introduces new high-index glass compounds to thermal poling treatment, as the second-order optical nonlinearity is predicted to be enhanced in proportion to the intrinsic third-order optical nonlinearity. In particular, a variety of bismuth-borate glasses, $Bi_2O_3$-$ZnO$-$B_2O_3$, are investigated in this chapter. Poling conditions and current dynamics are very different from those in silica and change dramatically with $Bi_2O_3$ content. The $\chi^{(2)}$ value is indeed shown to scale with $\chi^{(3)}$, which in turn increases with increasing bismuth oxide content. However the performance of these high refractive index glasses are limited by their dielectric breakdown strength. This latter result demonstrates the importance of selecting glass compositions on the basis of both $\chi^{(3)}$ and dielectric breakdown to succeed in enhancing second order nonlinearity. A novel mechanism based on proton migration is finally described to explain the experimental results.

In Chapter 5 a refined version of the standard thermal poling technique is introduced, which consists of increasing the voltage during the cooling phase, when the dielectric breakdown point of the material progressively increases. The first section overviews the experimental evidence of in-built electric field strengthening by adopting the new poling procedure. Moreover, control of the spatial distribution of the nonlinearity is gained as well, which is expected to be very useful for optimizing the spatial distribution of nonlinearity in waveguiding regions. The last section considers the work done on finding the optimized poling conditions best tailored to the bismuth-based glass compounds.

Chapter 6 describes the results achieved toward the development of a device based on the second-order nonlinearity induced in bismuth-based novel material by thermal poling. Two device designs are proposed, an electro-optic modulator and a frequency doubler, based on poling waveguides fabricated by sputtering and femtosecond laser direct writing, respectively. The first demonstration of second-order nonlinearity induced by thermal poling in sputtered glass film is also given. This route opens the new opportunity of realizing more complex on-chip structures for high performance integrated all-optical devices.

As a further investigation on materials with high third-order nonlinearity, in Chapter 7 thermal poling is employed on nanoncomposite silicate glasses to enhance second-order nonlinearity, as doping with metal nanoclusters increases the $\chi^{(3)}$ of the glass host by hundreds of times at wavelengths close to the surface plasmon resonance. Although no *SHG* signal was detected after poling, the electric-field-assisted dissolution of gold

nanoparticles embedded in a low conductivity sol-gel glass film on a soda-lime glass substrate is demonstrated. Thermal poling is employed to destroy randomly distributed gold nanoparticles (15 $nm$ in diameter) with a volume filling factor as small as 2.3% within the sol-gel film. The surface plasmon absorption band at 520 $nm$ is suppressed in the region covered by the anodic electrode.

Finally, in Chapter 8 the conclusion of this thesis is outlined. A summary of the major achievements is given along with proposals for the most profitable avenues to pursue towards engineering and developing bismuth-based active optoelectronics components.

# Chapter 2

# Physical origin of the nonlinearity in thermally poled glass systems

## 2.1 Introduction

An overview of the theoretical background of thermal poling is given in this chapter, with an insight into the relevant aspects of nonlinear optics offered in the next section. Some of the most plausible explanations of the mechanism behind the $SON$ formation in glass are also provided. Inspired by the applications already proposed on poling waveguiding geometries, a final emphasis is put on results and progress towards realizing competitive integrated all-optical active devices.

## 2.2 From nonlinear optics to thermal poling

The polarization, $\vec{P}$, of a dielectric medium subjected to an external optical electric field, $\vec{E}$, with frequency $\omega$, can be expanded in a power series of the electric field:

$$\vec{P} = \epsilon_o \chi^{(1)} \vec{E}(\omega) + \epsilon_0 [\chi^{(2)} \vec{E}(\omega)\vec{E}(\omega) + \chi^{(3)} \vec{E}(\omega)\vec{E}(\omega)\vec{E}(\omega) + \ldots] = \vec{P_l} + \vec{P_{nl}} \qquad (2.1)$$

where $\epsilon_o$ is the vacuum permittivity, $\chi^{(1)}$ is the linear susceptibility which accounts for the linear optical index and $\vec{P_l}$ the polarization term which is proportional to the applied field. The nonlinear polarization term, $\vec{P_{nl}}$, proportional to higher-order terms of the applied electric field, becomes not negligible in the presence of high input light intensity. In particular, the second order optical nonlinear effects include second harmonic generation ($SHG$) and the linear electro optic ($LEO$) effect. The magnitude of the susceptibilities is dependent on the frequency of the electric field, so the frequency has to

be indicated when stating the magnitude of the susceptibility, although this is omitted throughout this discussion.

Using the second order nonlinear optical process as an example, the frequency dependence is conventionally indicated as

$$\chi^{(2)}(-\omega_3;\omega_1,\omega_2)\vec{E_1}(\omega_1)\vec{E_2}(\omega_2) \tag{2.2}$$

in which two electric fields of different frequency, $\vec{E_1}(\omega_1)$ and $\vec{E_2}(\omega_2)$, act simultaneously on the medium to produce an electric field of frequency $\omega_3$.

- For second harmonic generation this notation becomes $\chi^{(2)}(-2\omega;\omega,\omega)\vec{E}(\omega)\vec{E}(\omega)$
- For the *LEO* effect the susceptibility is rather expressed as $\chi^{(2)}(-\omega;\omega,0)\vec{E}(\omega)\vec{E}(0)$

Amorphous materials, such as liquid and glasses, inherently show no even-order optical nonlinearity due to their macroscopic inversion symmetry. Therefore, all components of the second-order susceptibility tensor are zero and second harmonic generation is consequently forbidden, in the electric dipole approximation. Nevertheless, Myers et al. (1991) demonstrated that it is possible to induce permanent second harmonic generation (*SHG*) in bulk glass by thermal poling treatment, as discussed in Section 1.1.1. During the poling process, the sample is heated in order to thermally activate the conduction. In flame-fused silica glass ($10^{-4}\,wt\%\,Na$), alkali metal ion impurities form, in general, weak bonds with the lattice structure such as negatively charged nonbridging oxygen centers. As a result, the negative charges are relatively motionless compared to sodium ions, whose activation energy for migration is about $1\,eV$ at temperature above $200^oC$ (Mukherjee et al., 1994). The externally applied field causes these mobile charge carriers to drift toward the cathode where they are neutralized by injected electrons. Such a migration leads to the creation of a negatively charged depleted region by a dissociation process. The lack of mobile charges there implies higher resistivity compared to the rest of the sample. In this scenario (Alley et al., 1998), the charge front, $d$, separating the depletion region from the neutral region, evolves through the sample depth according to the following formulae:

$$d(t) = w \cdot \tanh\left(\frac{t}{2\tau}\right) \tag{2.3}$$

with

$$\tau = \frac{L}{\mu}\sqrt{\frac{\epsilon}{2qNV}} \tag{2.4}$$

and

$$w = \sqrt{\frac{2\epsilon V}{qN}} = 2\tau\mu E_0 \tag{2.5}$$

where the steady-state thickness of the nonlinear layer is $w$ and $\tau$ is the time constant related to its formation; $q$ is the electron charge; $N$ and $\mu$ are the ion concentration and mobility, respectively; $L$ and $\epsilon$ are the width and permittivity of the glass sample; $V$ is the applied voltage and $E_0 = V/L$ is the uniformly distributed field in the absence of charge motion.

The motion of the charge front can be measured using the current flowing through the glass, where the current density ($J = I/S$) is given by:

$$J(t) = \frac{2qNw}{\tau} e^{-\left(\frac{t}{\tau}\right)} \left[ \frac{\left(1 - e^{-\left(\frac{t}{\tau}\right)}\right) \frac{w}{L} + \left(1 + e^{-\left(\frac{t}{\tau}\right)}\right)}{\left(1 + e^{-\left(\frac{t}{\tau}\right)}\right)^3} \right] \tag{2.6}$$

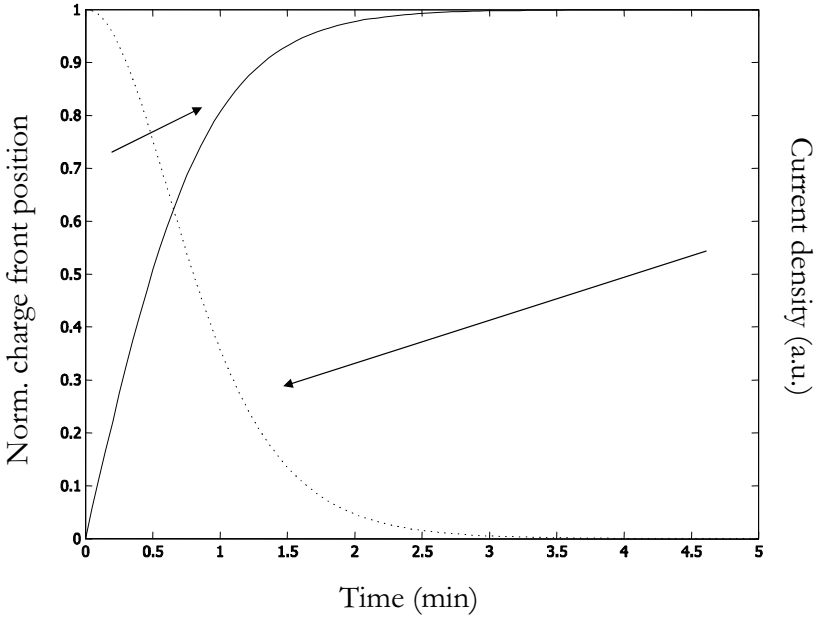


FIGURE 2.1: Typical temporal evolutions of the charge front (*line*) and the current density (*dotted line*) resulting from the migration of $Na^+$, taking $N_{Na^+} = 5.79 \times 10^{16} cm^{-3}$, $\mu_{Na^+} = 5 \times 10^{-15} m^2/Vs$, $\epsilon = 3.8$, $L = 200 \mu m$, $E_0 = 2 \times 10^7 V/m$ [$N = d_s W_p N_A / (100 \times W_A)$, where $d_s$ is the density of silica ($2.203\, g \cdot cm^{-3}$), $W_p$ is the weight percentage of sodium ($10^{-4} wt\%$ or $1\, ppm$ in weight), $W_A$ is the atomic weight of sodium and $N_A$ is Avogadro's number].

The ionic movement in Figure 2.1 progressively slows down, since most of the applied voltage becomes dropped across the depletion region owing to its increasing resistivity. At the same time, the nonuniform charge separation gives rise to an induced electric field within the glass sample, $E_{DC}$ in Figure 1.1, whose magnitude and distribution depend on the concentration/distribution of dissociated charges. This internal electric field, in turn, counteracts the applied voltage, shields the bulk of the sample and is finally frozen inside the glass when it is cooled with the *DC* bias still applied.

The intrinsic third-order nonlinear susceptibility in the depleted region ($0 < z < d$) experiences rectification by such a built-in electrostatic field, so to permit an otherwise vanishing second-order nonlinear susceptibility $\chi^{(2)}$ in glass matrices. In this simple model, the electric field peaks at the surface which is in contact with the anode, decreases linearly across the depletion region, and increases with time according to:

$$E(z,t) = \frac{V}{L} - \frac{qN}{\epsilon}\left[z - d(t) + \frac{1}{2L}d(t)^2\right] \tag{2.7}$$

In the steady state, the electric field underneath the anode quickly reaches extremely high values, close to the dielectric breakdown strength of silica ($\approx 2 \times 10^9\, V/m$) (Alley et al., 1998) and its peak value is given by

$$E_p = E(0,\infty) = \frac{qNw}{\epsilon} \tag{2.8}$$

Finally, the temporal evolution of the electric field strength inside the glass cross section is plotted in Figure 2.2.

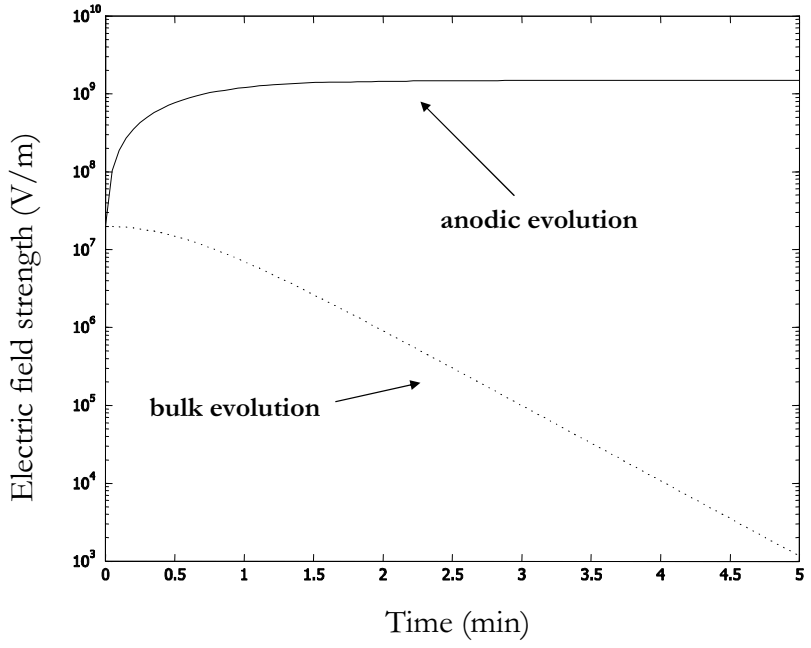


FIGURE 2.2: Temporal evolutions of the electric field strength at the anodic surface (*line*) and in the electrically neutral region ($d < z < L$), when the electric field is spatially uniform and vanishes with time according to $E(t) = \frac{V}{L}\left[1 - \left(\frac{d(t)}{w}\right)^2\right]$ (*dotted line*). Parameters of the model are the same as in Figure 2.1.

To summarize, this simplified picture of the actual space charge dynamics allows us to capture the essential features of the poling process, as far as the frozen-in field mechanism is involved. The result is that the glass centrosymmetry is locally broken by the poling

treatment and a thin optically nonlinear layer, about $10-15\,\mu m$ in thickness, is usually induced near the surface close to the positive electrode. The most cited models proposed in literature to explain the macroscopic generation of the second harmonic signal in glass are summarized in the next section.

## 2.3 From thermal poling to nonlinear optics: overview of mechanisms

As described in Section 2.2, the generation of a second harmonic signal implies a lack of inversion symmetry, but it should be stressed that understanding of the exact physical mechanism behind the occurrence of non-linearity in bulk glass is far from complete. An overview of the most frequently mentioned mechanisms in the literature is given in this section to explain the growth and decay of $SHG$ in thermally poled glass.

### 2.3.1 The rectification model

A variety of systematic investigations aimed at exploring the onset of second order nonlinearity in a glass matrix have been seeking the physical explanation of what looked to be an exception to the rule of nature. Among the others, neutron diffraction and inelastic scattering measurements (Cabrillo et al., 1998) have shown that the glass structure of poled silica becomes anisotropic and differs significantly from that of native samples. From those data, crystallization of part of the glassy matrix into a cristobalite polymorph of silica appeared as a reasonable possibility. Direct evidence of deep structural alterations induced by thermal poling in silica by means of inspection of poled and native samples by electron microscopy was also provided by Cabrillo et al. (2001) . The electron diffraction patterns of a poled silica glass revealed the presence of a large amount (of order 10%) of crystallites showing patterns consistent with partial crystallization of the silica matrix. The possibility that the $\chi^{(3)}$ of the samples was enhanced by such a partial crystallization seemed therefore plausible (Xu et al., 2000a). Garcia et al. (2003) measured $\chi^{(3)}$ enhancement of a factor of 2 after poling a channel waveguide, as Quiquempois et al. (2005b) did in Infrasil glass. This, in turn, would enhance the $\chi^{(2)}$ induced by the frozen-in field, as postulated in the Equation 1.2. Yet, recent Rutherford backscattering investigations, as well as elastic recoil detection and resonant nuclear reaction have shown peculiar features introduced in silica by thermal poling.

Nonetheless, the most widely accepted explanation for the generation of $SON$ in glass does not invoke structural modifications within the glass to accomplish the breakdown of its radial symmetry. In a model first proposed by Stolen and Tom (1987) to explain self-induced second-harmonic generation, the nonlinear second-order $\chi^{(2)}$ susceptibility

was stated as rectified by the intrinsic nonlinear third-order $\chi^{(3)}$ susceptibility according to:

$$\chi^{(2)} \cong \frac{3}{2} \cdot \chi^{(3)} E_{DC} \tag{2.9}$$

where $E_{DC}$ represent the permanent built-in electric field induced by charge migration (Figure 1.1), and 3/2 accounts for the degeneracy factor which arises from the convention chosen to express the electric field in Equation 2.1. Assuming that this microscopic adjustment is responsible for the $\chi^{(2)}$ susceptibility in poled silica glass, alkali metal ions constitute the only positive charge carriers. As mentioned in Section 1.1, this mechanism was supported by the fact that a nonlinearity of about $1\,pm/V$ was measured with a typical sodium weight percentage of $1\,ppm$, whereas it was considerably reduced in synthetic silica and not observed at all in poled high-purity silica glasses which included negligible content of metallic impurities (Kameyama et al., 2001).

Evidence of an upper limit on $\chi^{(2)}$ set by the breakdown electric field were copiously given for silica-based glasses, as described in Section 1.1.2. To account for larger second-order susceptibilities, one must invoke the dipole orientation mechanism, well known in organic nonlinear optical materials and commonly used in poled polymers (Suarez and Puma, 1998). Such a mechanism, along with formation of micro-crystallites, was also adopted to explain the origin of the nonlinearity induced in glass by $UV$ poling (Fujiwara et al., 2000). In glass, dipoles take the form of polar bonds, defects or highly polarizable entities which could be oriented with the external electric field. The freezing of oriented dipoles would break the symmetry and lead to a second-order nonlinearity no longer forbidden in the whole bulk of the glass (Figure 2.3).

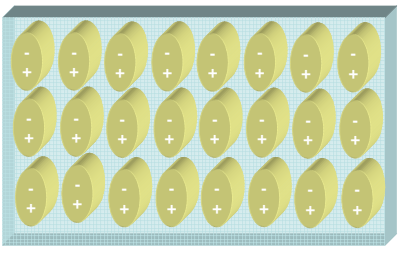

FIGURE 2.3: Oriented dipoles: $\chi^{(2)}$ located in the whole bulk

In this case, the $\chi^{(2)}$ susceptibility would proportionally depend on the second-order hyperpolarizability tensor $\beta$ according to:

$$\chi^{(2)} \propto N \cdot L(E) \cdot \beta_{eff} \tag{2.10}$$

where $\beta_{eff}$ can be written as a linear combination of $\beta$ tensor coordinates, $N$ is the concentration of hyperpolarizable entities, and $L(E)$ is an orientation factor $(0 < L < 1)$

under the total electric-field, $E$, within the material. If one assumes that the concentration of hyperpolarizable entities is sufficiently small so that the depolarization field is several orders of magnitude smaller than the charge migration field, the two models can be solved independently and the charge migration model determines the total electric field during the poling process.

According to Mukherjee et al. (1994) a combination of the two different mechanisms may be responsible for the induced second order nonlinear effect in thermally poled silica. The authors proposed a model based on charge transport of single mobile ions creating a depletion region, followed by reorientation of dipoles, as suggested by Kazansky and Russell (1994). The permanent induced second order nonlinearity can be expressed as the sum of both effects:

$$\chi^{(2)} \propto \chi^{(3)} E_{DC} + (\beta/5kT) E_{DC} \tag{2.11}$$

The first term in Equation 2.11 is related to the interaction between the residual electric field $E_{DC}$ inside the material and the third order nonlinearity. The second term is the resulting macroscopic second order nonlinearity induced by reorientation of polar bonds during the poling treatment, each of them with a permanent dipole moment and microscopic hyperpolarizability ($\beta$) corrected by the local field which is effectively seen by each dipole. An external electric field, of at most $5\,kV/mm$, may or may not create a large permanent dipole moment in the silica glasses with the same order of second-order hyperpolarizability as that of the crystals. It could be concluded that the main contribution to the effective $\chi^{(2)}$ in poled silica came from the nonlinear phase confined in a few microns below the anodic face, where Lesche et al. (1997) finally measured a large space-charge field by in-situ interferometric direct inspection during $HF$ etching.

### 2.3.2 Multiple-charge carrier drift during $SON$ formation

Secondary ion mass spectroscopy ($SIMS$) and energy dispersive spectrometry ($EDS$) were employed to map the charge distribution in thermally poled fused silica (Alley et al., 1999) and thus to confirm the drift of cations from the anodic side (Garcia et al., 1998). However, investigations made by Mukherjee et al. (1994) showed a complex spatial distribution of nonlinearity under the anode that was incompatible with the single mobile species model. To understand the dynamic aspect of the nonlinearity creation, one needs to take into account both internal charges initially present in the sample ($Na^+, H^+, K^+, \ldots$) and the charge injection ($H^+, \ldots$) due to ions and/or water present in the atmosphere.

Kazansky and Russell (1994) proposed that thermal poling occurs in two stages. In the first stage, alkali metal ions, mainly $Na^+$, or $H^+$, move toward the cathode leaving

behind negative charge below the anode. During the second stage, still at temperatures as high as $280°C$, high field ionization occurs near the anode owing to an enhanced ionic mobility. Initially proposed for a way to preserve displaced space charge in thermally poled glass, this mechanism effectively involved a three-species movement. Another variant (Takebe et al., 1996) proposed the first stage as above; however, in the second stage, negatively charged oxygen ions or electrons associated with the depleted cations were the third charge carriers. Further developments (Kazansky et al., 1997) indicated that in this second stage, electrical breakdown occurred and, therefore, electrons were most likely to be the predominant charge carriers, as the high field near the anode would draw surface electrons into the anode.

These features were qualitatively explained with a model, proposed by Alley et al. (1998), incorporating two mobile ionic species with drastically different mobilities: fast moving $Na^+$ ions followed by the next most mobile $H^+$ ions in silica, having a relative difference of $10^3 - 10^4$ in ionic mobilities at temperatures of $230°C$. After the removal of sodium ions, the high electric field in the anodic depleted region would break the macroscopic centrosymmetry and lead to ion-exchange between $Na^+$ and $H^+$ ions, associated with water or other mobile cations. These injected ions could also interact with bridging bonds in the glass and induce the breaking of these bonds, giving rise to non-bridging hanging oxygen. Sodium mobility was reported to vary markedly, ranging from $1 \cdot 10^{-15}\, m^2V^{-1}s^{-1}$ to $5 \cdot 10^{-13}\, m^2V^{-1}s^{-1}$ for concentrations of $1\, ppm$ at $270°C$, and brought about by variations in both ionic or total impurity concentrations and distributions (Figure 2.4). As a result, the electric field peak would move in from the anodic surface and the width of the $Na^+$ depletion region would progressively adjust to maintain the overall voltage drop across the sample. Therefore, a double layer of positive and negative charges would be created during the poling process and the distribution of the electric field would show a triangular profile, with a peak value located inside the glass rather than on the anodic surface, as pictured in Figure 2.4.

In an attempt to interpret differences between air and vacuum thermal poling, Pruneri et al. (1999b) asserted that the near-surface $SON$ displayed a positive-negative-positive structure formed at the anodic region of a poled silica glass. Thus, the movement of two cations was considered: fast $Na^+$ ions moving toward the cathode, followed by a constant $H^+$ injection at the anodic surface penetrating the silica, either due to atmospheric moisture or to hydrogenated glass surfaces. Again, the high electric field in the depletion region would force electrons and negatively charged oxygen ions to move. Temporally, supposing $[Na^+]$ to be of the order of $1\, ppm$ and a typical poling current of $I = 10\, \mu A$, the impurity in a thickness of $10\, \mu m$ would disappear after only $16\, msec$. However, the poling time required for the second-order nonlinearity to appear was found to be longer than $30\, sec$ (Quiquempois et al., 2000a). Hence, some other participating ions from the air, either positive such as $H^+$ and hydronium $H_3O^+$, or negative such as $O_2^-$ and $OH^-$, must be taken in account to induce the positive and the negative currents

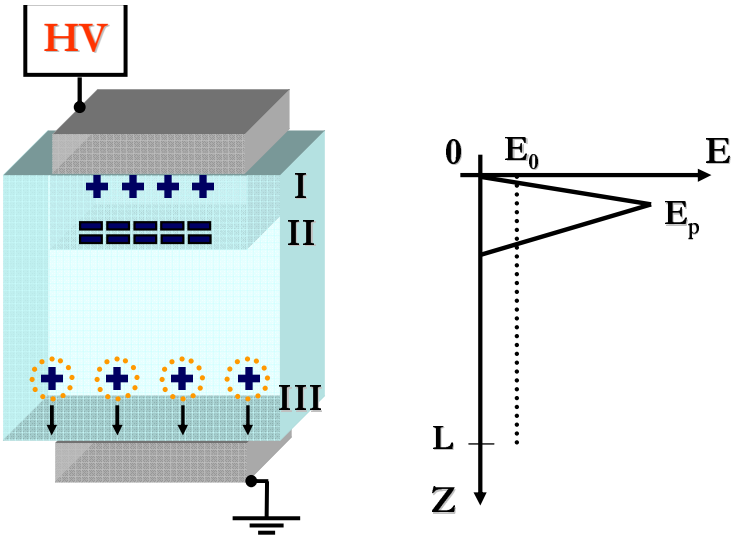


FIGURE 2.4: Multiple carrier model. The positively charged region due to electron ejection and/or $H^+$ cation injection ($I$), the negatively charged region due to $Na^+$ depletion ($II$), and the neutral region ($III$). The distribution of the electric field is shown while the voltage is still on.

(Alley and Brueck, 1998). Alley et al. (1999) reported indications of other ionic species playing a vital role in the resultant $SON$, such as $Li^+$ or $K^+$ in fused silica.

A two charge separation model with a single ionic charge carrier was proposed by LeCalvez et al. (1997) to determine the magnitude and the evolution of the total electric field within the sample during the poling process. The basic assumption was that the applied electric field would be totally screened by the high concentration of negative charges in the cation-free region near the anodic surface of the sample, hence equal to zero in the bulk of the sample. As a consequence, the non-zero electric-field would be confined in a thinner layer, its thickness depending on the initial positive carrier concentration. In this case, bond orientation, if it occurred, could only be induced near the surfaces. However, this model also predicted that a nonlinear $\chi^{(2)}$ susceptibility should be always induced whatever the value of the poling electric field. Quiquempois et al. (2002) introduced a more realistic charge migration model to take into account charge recombination and charge dissociation mechanisms occurring during the poling process. The authors proved that there was a voltage threshold below which no $\chi^{(2)}$ could be induced. Furthermore, they pointed out the existence of a nonzero electric field within the bulk of the sample, contrarily to the hypothesis of LeCalvez et al. (1997). To test experimentally the validity of this model, they poled $1\,mm$ thick Infrasil silica slabs using voltages ranging from 0 to $4\,kV$ and reported experimental evidence of a poling voltage threshold of $900\,V$ in these samples. The strength of such a nonzero electric field could be enough to orient hyperpolarizable dipoles which might contribute to the $\chi^{(2)}$ nonlinearity. It would be easier to detect the effect of these dipoles in thinner samples, where the volume electric field is higher, being inversely proportional to the

sample thickness. However, several tests on silica glasses verified that the magnitude of the induced nonlinearity was determined essentially by the poling voltage and the total concentration of charges present in the glass sample. Too high poling voltage or cation concentration would lead in fact to partial electric breakdown near the sample surface where the electric-field distribution would rather assume a trapezoidal shape.

In the light of these outcomes, only in certain, and rather elusive, conditions was it possible to claim nonlinearity values beyond $1\,pm/V$. It can be concluded that more systematic investigations are therefore required to look deeper into the poling process in order to clarify some discrepancies and validate the theoretical model for the generation of second order nonlinearity in glasses. In particular, the next section describes how a careful optimization of all the poling parameters would finally permit the achievement of the optimum frozen-in electric field, to which the dielectric breakdown intrinsically fixes the limit. Furthermore, this study will also allow the evolution of the nonlinear thickness and coefficient in poled samples to be monitored, and demonstrate the possibility of tailoring the nonlinear layer to match different waveguide geometries.

### 2.3.3 Approaching breakdown by optimizing the poling parameters

Second-order susceptibility induced by the formation of a space-charge region is now widely accepted as the predominant effect of thermal poling, although various studies in the literature show continuing investigations on how to refine the treatment parameters. Liu et al. (2000), for example, published their results on the existence of an optimum poling temperature for an extremely high applied voltage in silica. In a sample poled in vacuum atmosphere at $400°C$ with $20\,kV$ applied, a $d_{33}$ of $0.7\,pm/V$ was measured, twice as large as in identical samples poled under standard conditions ( $275°C/ \approx 5\,kV$). The authors claimed that the increases in the poling temperature would lead to increasing the molecular agitation, which is necessary to facilitate ion migration, whereas increases in the poling field should lead to an increase in the internal force that orients dipoles and/or separate the space charge, having as a result a nonlinear region with a greater width and buried depth.

Many glass materials have been tested for different ranges of poling time (Alley et al., 1999), temperature (Triques et al., 2000), atmosphere (Pruneri et al., 1999b), but very few have yet been carried out on modifying the dynamics of the standard procedure. To be cited are the investigations made by Martinelli et al. (2002) when performing thermal poling under square alternating voltages at variable frequency on Suprasil-I samples. Experimental results exhibited a 13 times increase compared to a continuous voltage poling in the second harmonic signal generated within a sample poled at the frequency of $1\,mHz$ (resonance peak): the authors reported also on spatial modification of the charge distribution depending on the voltage frequency.

In this context, the results collected during this project when adopting a newly developed version of the standard poling treatment are reported in Chapter 5, where it is shown how increasing voltage during cooling significantly enhances the in-built electric field strength compared to constant-voltage poling procedure. At the same time, the innovative poling technique is established to gain control on the nonlinear region evolution, crucial parameter to integrate nonlinearity in waveguiding regions. The thickness of the second-order nonlinear layer in poled glass becomes in fact an important property to study in mechanisms and applications of the $SHG$, among which are active waveguiding devices.

A review of research into thermally-poled guiding devices is provided in the next section, in preparation for the original contribution reported in Chapter 6 of this thesis, where the results obtained on poled bismuth-based slab waveguides are presented.

## 2.4 How thermal poling may affect waveguides in glass

Silicate glass waveguides are amongst the frontrunners for realization of multifunctional, low-cost planar lightwave circuits. Besides being one of the dominant materials in information technology because of its low fabrication cost compared to ferroelectric crystals and semiconductors, glass is also superior for optical properties (see Section 1.1) and high compatibility with existing fibre-based networks. Thermal poling has opened up new perspectives in exploring the integration of $SON$ otherwise prohibited in glass-based guiding systems.

Throughout this section, achievements toward developing novel material processing for optoelectronic devices are addressed, with a particular accent on those applications typically restricted to crystals, such as parametric frequency conversion and electro-optic modulation. The ability to modulate a material's refractive index with an applied field is necessary for making optical switches and electric field sensors. Frequency conversion of coherent radiation through parametric processes, such as second harmonic and sum or difference frequency generation, is also desirable to produce a large range of wavelengths and for the construction of tunable laser sources. Hence, glass-based channel and planar waveguides are promising candidates in numerous applications of active nonlinear optical components.

In 1994, Liu et al. (1994) demonstrated electro-optic phase modulation in a thermally poled fused-silica channel waveguide: a phase shift of 32 mrad was measured at 633 nm for a device interaction length of 4.8 mm and an applied electric field of $7.3\,V/\mu m$ in the channel waveguide. Based on a thermally poled $GeO_2$ doped channel waveguide geometry, Abe et al. (1996) demonstrated the first switching-voltage measurement from an integrated Mach-Zehnder interferometer ($MZI$). A custom-made unbalanced $MZI$ was also adopted by Garcia et al. (2003) both to measure directly the induced electric

field after poling and gain further insights on the dc-Kerr coefficient effect upon the electro-optic modulation.

However, the coexistence of waveguide fabrication and thermal poling may be difficult to reconcile, depending on the technology adopted. In particular, in an ion-exchanged waveguide process, the high temperature and high field needed to achieve the poling-induced ion migration, may affect the profile of the waveguide and/or deteriorate its optical performance. If the sample is poled first instead, the fabrication steps required for light to be guided, could modify or erase the charge distribution that gives rise to the frozen-in internal field.

Margulis and Laurell (1996) found that single mode channel waveguides could be directly realized by applying a thermal poling process to soda-lime glass substrate ($280°C/2.5\,kV$) by using a deposited aluminum film anode in which narrow channels were opened by photolithography. There, the guided light interacted with the poling induced nonlinearity through the evanescent field. Waveguide formation implied that the refractive index was lowered not only under the electrodes on either side of the channel, but also under the channel itself. This could partly be attributed to fringing fields, but it was also likely that the field line distribution, and thus the current flow, evolved during the poling process to deplete cations on the region under the channel as well. Indeed, the refractive index of the glass was measured to be reduced by 1.5 percent due to the depletion of sodium ions, making possible the formation of waveguides in a depressed cladding configuration. It was speculated that glass under the electrodes suffered from some structural rearrangement and compaction, both likely to increase the refractive index of the depleted region.

More recently, self-created planar waveguides were demonstrated by employing constant-current thermal poling in soda lime glasses containing more than one species of alkali or alkaline-earth ion (Brennand and Wilkinson, 2002). Near the anode, the $DC$ electric field applied to the substrate separated the mobile cations into regions according to their mobility, each one presenting a different refractive index. Although no $SHG$ was measured, the depth of the waveguide was shown to depend significantly on poling time, temperature, and bias voltage, making it possible to design to some extent the resulting profile. Nevertheless, the measured index change ($> 10^2$) was large enough to suggest that waveguides could be formed by poling even in glasses with lower alkali-content than soda lime glass.

Since these preliminary outcomes, researchers' efforts have converged on engineering device configurations which allow guided light to be propagated within the high field region, thereby efficiently exploiting the induced nonlinearity. To optimize the efficiency of the $SON$ in waveguide devices and the overlap between the nonlinear and waveguiding regions, along with the $d_{33}$ optimization, Faccio et al. (2001b) studied the temporal evolution of both the second-order nonlinear coefficient and of the nonlinear thickness

in thermally poled silica-glass slides. By devising a high-resolution all-optical technique called the 'noncollinear Maker fringe technique', a dependence of the measured quantities on sample thickness was also reported which could be ascribed to the different internal electric fields in the depletion region. However, the thickness was experimentally shown to increase at a rate that differed significantly from that reported for the corresponding ionic charge fronts. Those results were substantially inconsistent with those obtained in Section 2.2 on the basis of only positive charge migration, implying that other factors ought to be taken into account, in particular when poling multi-layered guiding structures.

As a confirmation, Faccio et al. (2001a) reported on the effect of the interface between core and cladding during thermal poling of D-shaped fibre. Ion migration was measured to be significantly hindered in the heavily doped region, thus limiting the thickness of the depletion region and, therefore, of the nonlinear layer. On the other hand, the authors claimed that the nonlinearity ($d_{33}$ between $0.2 - 0.4\,pm/V$) was concentrated in the overcladding layer closer to the positive electrode. There, the cations responsible for the formation of the depletion region during thermal poling were significantly slowed down or trapped at the boundary, thus limiting the extent of the nonlinear layer. As this effect would depend on the thickness of the $GeO_2$ doped layer, the core region was engineered to be as small as compatible with the device specification. Furthermore, increasing the ion mobility by poling at higher temperature and voltage effectively reduced the dielectric barrier encountered at the overcladding interface and thus allowed the nonlinearity to move much deeper into the sample.

These speculations were in agreement with the findings concerning thermal poling of PECVD Ge-Si-N waveguides (Arentoft et al., 2000b). After poling, *SIMS* measurements revealed an accumulation of sodium and silver ions at the cladding-core and the core-buffer interfaces. In that case, however, very large second-harmonic signals ($\chi^{(2)} \cong 22 \pm 8\,pm/V$) from thermally positively poled silica waveguide samples were reported (Arentoft et al., 2000a), due to the much thinner layers the nonlinear region had to penetrate. In contrast, the peak value for the negatively poled sample was only $\chi^{(2)} \cong 0.6 \pm 0.2\,pm/V$ and small linear electro-optic ($EO$) effects were detected. Poling of samples with a negative bias rather than a positive one would reduce both the risk of electrical breakdown and the injection of cations into the waveguides from the top electrode during poling. Poling induced diffusion of $Ag$ from the electrode may lead to higher propagation losses in the waveguides and locally increase the $\chi^{(2)}$ value, due to the resonant enhancement of the linear and nonlinear optical properties at the surface plasmon frequency. Thus, the large difference between $EO$ and $SHG$ effects for the positively poled sample was explained by the introduction of silver from the electrode. In the light of these results, Ren et al. (2002) presented a systematic investigation of the

poling-induced electro-optic effect in germanium and nitrogen codoped channel waveguides. After the treatment, the poled waveguide samples were characterized electrooptically using a fibre-based Mach-Zehnder interferometer, showing almost polarization independent $EO$ effect ($r_{TM}/r_{TE} \approx 1.1 \pm 0.03$); low linear loss ($< 1\,dB/cm$) and polarization dependent loss $< 0.2\,dB/cm$, which demonstrated great technological potential. Furthermore, an optimum poling temperature ($T_{opt} = 357^oC$) was shown to exist for a given poling voltage, setting the maximum $EO$ coefficient at $r \cong 0.076\,pm/V$ with a negative applied field of $208V/\mu m$. The deduced $\chi^{(2)}$ was $\cong 0.2\,pm/V$ if $\chi^{(2)} \cong rn^4/2$, the latter being correct in case of no dispersion of $\chi^{(2)}$ and perfect overlap between the waveguide mode and the nonlinear area.

For exploitation in a device, the confinement of the light and the spatial modulation of $\chi^{(2)}$ along the waveguide has to be optimized. Quasi-phase matching for efficient wavelength mixing is achievable only if the induced $\chi^{(2)}$ is integrated over the profile of the relevant guided mode or modes, the fundamental and second-harmonic modes respectively. A periodically poled frequency-doubler with the record-high normalized conversion efficiency of $1.4 \times 10^{-3}\%/W/cm^2$ was recently demonstrated by Pedersen et al. (2005) on planar silica-on-silicon technology, which is almost an order of magnitude higher than that achieved on periodic poling of D-shaped fibre (Pruneri et al., 1999a). The corresponding nonlinearity was $\chi^{(2)} = 0.13\,pm/V$, obtained by applying $+2.5\,kV$ at $T_{opt} = 365^oC$ on silicon oxynitride buried waveguides with soft top cladding consisting of borophosphosilicate glass. Internal interfaces could be detrimental for the poling stability since undesired charge transport may occurr, even if the authors claimed a loss-less, high-quality waveguiding multilayer structure. Several glass combinations and waveguide geometries are to be tested to gain further control over the quasi phase-matching wavelength and bandwidth of similar devices.

## 2.5 Conclusion

The current state of art of the thermal poling has been assessed. Starting from a simplified ion-migration mechanism responsible for the nonlinearity formation, an overall understanding of the role played by the poling conditions has been achieved, with more emphasis on which parameters (poling time and voltage, temperature, material composition, glass conductivity and refractive index, etc.) may be crucial for significant enhancement of $SO$ nonlinearities in glass-based systems. Refined characterization techniques are necessary to obtaining information on nonlinear thickness, dynamics and profile without ambiguity and to engineer integrated devices based on phase and amplitude modulation and parametric frequency conversion processes.

# Chapter 3

# Techniques for evaluation of $\chi^{(2)}$

## 3.1 Introduction

Before proceeding to describe fundamental research on refining the poling procedure and the strategy to devise the most suitable glass compounds, the characterization methods which are typically employed to investigate the poling induced nonlinearity are described. It is now well established that obtaining an accurate knowledge of the thickness, profile and dynamics of the thin nonlinear region is crucially important in optimizing all the critical parameters affecting the poling process and thus to engineering efficient active glass-based devices. Three different characterization techniques are shown in detail in this section, the Maker Fringe method, the layer peeling procedure and scanning optical microscopy, respectively. The results will be compared with the aim to point out their relative advantages and drawbacks when employed to characterize thin nonlinear films.

## 3.2 Measurement of poling induced SON - limits of the standard Maker Fringe Technique

Thermally poled glass can be considered as an isotropic dipole system with uniaxial symmetry. Due to symmetry properties, the second-order nonlinear susceptibility tensor, $\vec{d} = \chi^{(2)}/2$, has six non-zero elements $d_{ij}$ which are related by $d_{31} = d_{32} = d_{24} = d_{15}$. Moreover, the tensorial components $d_{33}$ and $d_{31}$ are assumed related to each other by $d_{33} = 3d_{31}$. It follows that only one second order nonlinear coefficient, for example $d_{33}$, is needed in order to quantify the effective second order nonlinearity confined in a thin layer underneath the anodic surface. The value of $d_{33}$ may be determined by Maker fringe ($MF$) measurements (Maker et al., 1962).

The experimental layout required by the $MF$ technique is displayed in Figure 3.1. The glass sample is placed on a rotation stage and is probed with $p$-polarised light from a Q-switched and mode locked $Nd$:$YAG$ laser operating at the wavelength of $1.064\,\mu m$.

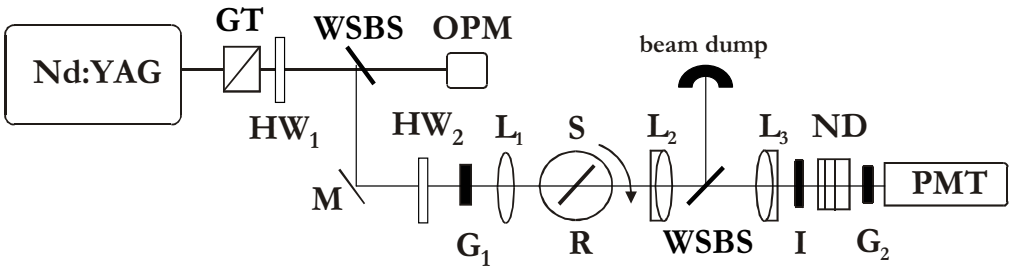


FIGURE 3.1: Maker fringe set-up. $OPM$: optical power metre; $PMT$: photomultiplier tube; $GT$: Glan-Thomson polariser; $HW_1$, $HW_2$: half-wave plates; $L_1$, $L_2$, $L_3$: lenses; $G_1$, $G_2$: blocking and narrow pass-band green ($0.532\,\mu m$) filters, respectively; $I$: infrared ($1.064\,\mu m$) blocking filter; $ND$ : neutral density filters; $R$: rotation stage; $S$: sample; $M$: mirror; $WSBS$: wavelength selective beam splitter.

Second-harmonic light ($\lambda = 0.532\,\mu m$) is generated while the fundamental light propagates inside the nonlinear region of the poled glass, as pictured in Figure 3.2. The intensity of the second-harmonic ($SH$) light which exits the sample is measured as a function of the angle of incidence by rotating the sample. From the spacing and position of the peaks in the second harmonic signal one can infer the nonlinear thickness $w$, whereas the nonlinear coefficient can be estimated by normalizing the $SH$ with respect to a reference sample of known nonlinearity.

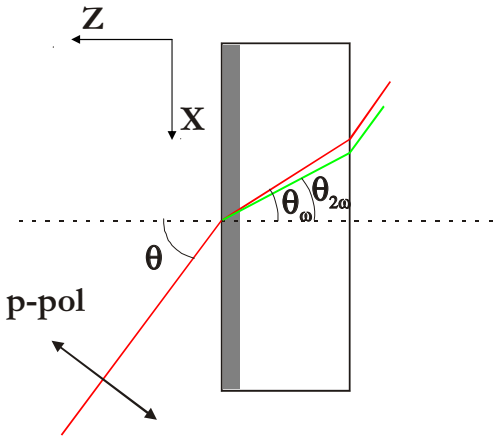


FIGURE 3.2: Geometry used for Maker fringe measurements. The $p$-polarised fundamental light beam impinges on the sample surface at an angle of incidence ($\theta$). The nonlinear region of the poled glass (*in gray*) is located in a thin layer underneath the glass surface which is in contact with the anode during poling. The sample is rotated perpendicularly to the plane of incidence ($ZX$), with the nonlinear region facing the incident light beam. $\theta_\omega$ and $\theta_{2\omega}$ are the angles at which the fundamental light and the $SH$ light propagate inside the glass, respectively.

In particular, the second harmonic power, $P_{2\omega}$, is expressed as a function of the incident angle $\theta$ by:

$$P_{2\omega} = K\frac{aT}{n_{2\omega}\, n_{\omega}^{2}}\left(d_{eff}\right)^{2}\left(\frac{w}{cos\theta_{2\omega}}\right)^{2} sinc^{2}\left(\varphi\right) \tag{3.1}$$

where

$$K = \frac{8\pi^{2}}{\Lambda\lambda^{2}\epsilon_{o}c}\left(P_{\omega}\right)^{2} \tag{3.2}$$

$$T(\theta) = T_{2\omega}\left(T_{\omega}\right)^{2} \tag{3.3}$$

$$a(\theta) = \frac{cos\theta\, cos\theta_{2\omega}}{cos^{2}\theta_{2\omega}} \tag{3.4}$$

$$\varphi(\theta) = \frac{\Delta k}{2}\frac{w}{cos\theta_{2\omega}} = \frac{\pi}{2}\frac{w}{l_{c}\, cos\theta_{2\omega}} \tag{3.5}$$

$$\Delta k = \frac{4\pi}{\lambda}\left(n_{2\omega} - n_{\omega}cos\left(\theta_{\omega} - \theta_{2\omega}\right)\right) \tag{3.6}$$

$$d_{eff} = d_{33}\left(\frac{1}{3}cos\theta_{2\omega}sin\left(2\theta_{2\omega}\right) + sin\theta_{2\omega}\left(\frac{1}{3}cos^{2}\theta_{\omega} + sin^{2}\theta_{\omega}\right)\right) \tag{3.7}$$

In Equation 3.1 - Equation 3.7, $P_{2\omega}$ is the voltage output from the photomultiplier tube, in turn proportional to the $SH$ signal, $\lambda$ and $\Lambda$ are the wavelength and beam area of the fundamental light, respectively; $\epsilon_o$ is the vacuum permittivity; $c$ is the light velocity in vacuum; $P_{\omega}$ is the pump power; $n_{\omega}$ and $n_{2\omega}$ are the refractive indexes of the glass at fundamental and $SH$ wavelengths, respectively; $\theta_{\omega}$ and $\theta_{2\omega}$ are the angles at which the fundamental light and the SH light propagate inside the glass, respectively; $T_{\omega}$ and $T_{2\omega}$ are the Fresnel transmission factors for the $p$-polarised fundamental light at the air-glass interface and for the $p$-polarised $SH$ light at the glass-air interface, respectively; $a$ is defined as the beam size correction factor; $w$ is the thickness of the nonlinear layer; $l_c$=$\pi/\Delta k$ is the coherence length of the nonlinear interaction with $\Delta k$ being the wave vector mismatch projected along the propagation direction of the $SH$ light; $d_{eff}$ is the effective $SON$ coefficient, defined as the projection of the nonlinear polarization vector along the direction of the second harmonic electric field. At a fixed incident angle, the $SH$ power increases with increasing values of the nonlinear thickness, provided that the latter is lower than the coherence length, the distance over which the $SH$ field and the $SH$ polarization wave, proportional to the square of the fundamental field, become $\pi$ radians out of phase. If the nonlinear thickness is longer than the coherence length,

the $SH$ power may increase or decrease as function of the thickness (Figure 3.3). This oscillating behavior is due to the $sinc^2$ factor in the right-hand side of Equation 3.1. Alternatively, for a thickness larger than the coherence length, the angular dependence of the $SH$ power exhibits a fringe pattern (Maker et al., 1962).

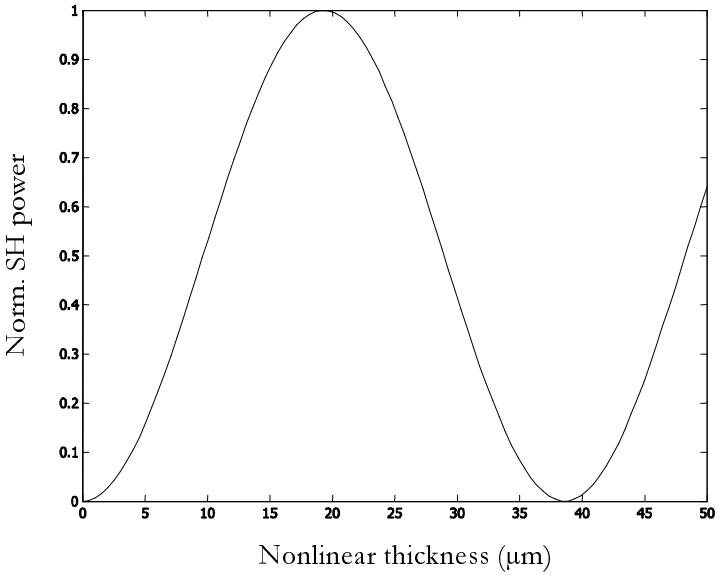


FIGURE 3.3: Normalised $SH$ power $P_{2\omega}$ as a function of the nonlinear thickness $w$. The incident angle $\theta$ is equal to 60°. The refractive index values are taken equal to those of silica, whose coherence length, $l_c$, is equal to $24\,\mu m$.

In Figure 3.4 the $SH$ power from a $1\,mm$ thick Herasil silica glass ($HE1$), poled in air at $280°C$, $4\,kV$ for $30\,min$ is recorded as a function of the incident angle.

The $SH$ power increases as the path length in the nonlinear layer increases, in other words the incident angle increases, reaches a maximum around 60°, and then decreases sharply because of Fresnel losses (J. Jerphagnon, 1970). The $SH$ power vanishes at normal incidence, as imposed by the angular dependence of the effective $SON$ coefficient (Equation 3.7). No fringe pattern can be observed, thus the thickness of the nonlinear region must be shorter than the coherence length ($l_c = 24\,\mu m$): typically the nonlinear thickness ranges between $1\,\mu m$ to $15\,\mu m$ in silica. The nonlinear coefficient can be determined by calibrating the measured power (dotted in Figure 3.4) with respect to a similar measurement performed on a reference $1\,mm$ thick quartz sample of known $d_{11} = 0.3\,pm/V$. The measured curve is then fitted to Equation 3.1, by assuming the best suited theoretical nonlinearity profile.

Two important remarks concerning the determination of $\chi^{(2)}$ from Maker fringe measurements are made. First, the knowledge of the refractive index and its dispersion is crucial. The dispersion of the refractive index will affect the coherence length, which is smaller in high-index glasses than in silica. From Equation 3.1, the measured $SH$

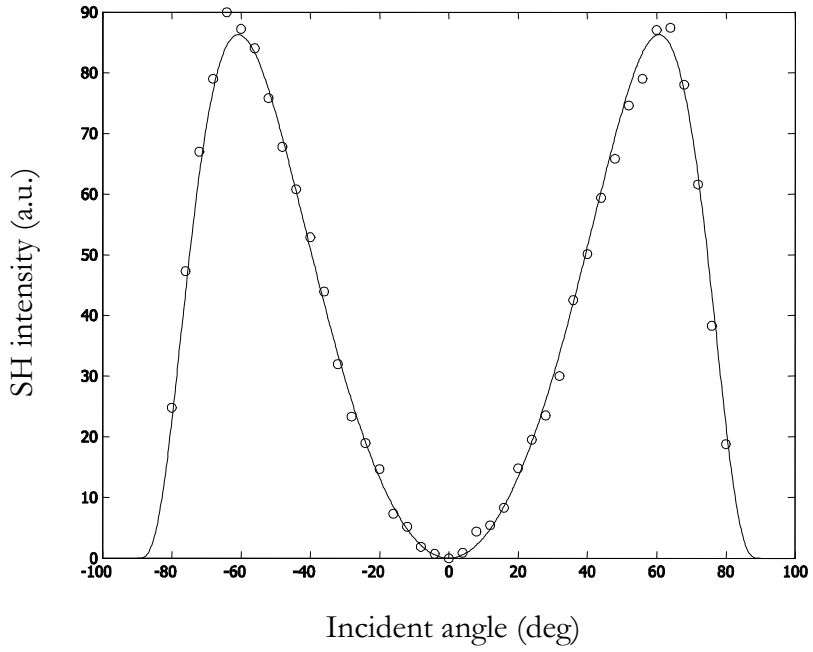


FIGURE 3.4: Maker fringe measurement (*circles*) and best fit to the theoretical curve given by Equation 3.1 (*line*) for a $1\,mm$ thick Herasil, poled in air at $280°C$, $4\,kV$ for $30\,min$.

power, neglecting dispersion, is inversely proportional to the cube of the refractive index. This means that, for a similar measured $SH$ power, the $\chi^{(2)}$ value induced in high-index glasses would be much higher than in silica. This will become more evident in Chapter 4, where the results obtained on poling bismuth-borate glasses are presented.

Second, the Maker Fringe procedure fails to fully characterize the poling induced nonlinear film when its depth is smaller than $l_c$, which often is the case in silica. More precisely, the minimum measurable value of the nonlinear thickness is limited by total internal reflection ($TIR$) in the sample and given by $w = l_c \cdot cos(\vartheta_{TIR})$, that is about $18\,\mu m$ for silica. An independent measurement of the nonlinear thickness, or at least an estimate of it, is therefore required. Typically, the thickness of the nonlinear region is determined by etching the poled area for different etching times, measuring the $SH$ power $P_{2\omega}$ at a fixed external angle and fitting the data, assuming a linear reduction in $SHG$ as a function of depth $z$. However, chemical etching causes permanent damage at the sample surface.

Less destructively, Faccio et al. (2000) introduced the two beam noncollinear Maker fringe technique to demonstrate how the generation of a polarisation wave at $2\omega$ from the overlapping of two identical fundamental beams carries information from nonlinear depths as small as $\leq 2\mu m$ with sub-micron resolution. It has to be pointed out, however, that an accurate retrieval of $\chi^{(2)}$ profile relied on quite critical alignment and *ad hoc* theoretical best-fit to the data.

The nonlinear thickness could also be inferred by interference between the $SH$ light beams generated from two identically poled samples stacked together (Corbari et al., 2003). In this case, the value of $w$ was given by:

$$w = \frac{2l_c}{\pi} cos\left(\theta_{2\omega}\right) \arcsin\left(\frac{\sqrt{P^{stack}/P}}{2}\right) \tag{3.8}$$

where $P$ and $P^{stack}$ are the $SH$ powers measured at an external angle $\theta$ at the output of the sample and at the output of the sandwich, respectively.

Ozcan et al. (2003) first employed an inverse Fourier transform algorithm to recover the second order nonlinearity profile from data collected in the same experimental configuration as above, along with a cylindrical lens assisted $MF$ technique, to avoid total internal reflection. Specifically, the Maker Fringe curve of two nonlinear films sandwiched together was shown to yield both magnitude and phase of the nonlinearity profile itself. As an application, Ozcan et al. (2004b) reported on a precise characterization of the nonlinearity profile in low-loss germano-silicate thin films grown onto fused silica substrates. In contrast to Khaled et al. (2000) $UV$ poled Ge-doped silica cited in Section 1.1, the authors succeeded to induce a permanent $\chi^{(2)}$ with a peak value as high as $1.6\,pm/V$. Furthermore, they presented a cross-sectional map of the second order nonlinear optical coefficient, whose distribution is required to optimize the overlap with optical modes.

A direct measurement would be preferable for a study which aims to both understand the fundamental mechanism of poling and to fully characterize poled components.

In what follows, the layer peeling algorithm is therefore introduced (Kudlinski et al., 2003a). This method has been firstly adopted by the research group of Prof. Gilbert Martinelli at the Universite des Sciences et Technologies in Lille to directly measure the $\chi^{(2)}$ spatial distribution in the depth of poled samples, with a submicron resolution. The evolution of the second harmonic signal is monitored while the nonlinear region is chemically etched off. Although the sample becomes locally damaged after characterization, the reconstructed $\chi^{(2)}$ profile does not depend on an *a priori* hypothesis as in all the $MF$-derived techniques. An alternative way to achieve a precise map of the nonlinear distribution is given by the second harmonic scanning optical microscopy presented in Section 3.4, which allows direct inspection with resolution less than $1\,\mu m$ and, consequently, spatially resolved investigation of second order nonlinear distributions.

## 3.3 Reconstructing the $\chi^{(2)}$ profile: layer peeling algorithm

Experimental investigations of the second order nonlinearity by layer peeling technique on poled glasses are carried out in collaboration with Alexander Kudlinski, Yves

Quiquempois and Gilbert Martinelli at the Universite des Sciences et Technologies in Lille.

An accurate determination of the nonlinear distribution within the first microns from the anodic surface of a poled sample is directly accessible by the layer peeling technique (Kudlinski et al., 2003a). This powerful characterization method consists of recording the *SH* signal as generated in a classical Maker fringe setup while the nonlinear thickness is peeled off by etching and measured using an interferometric optical method (Margulis and Laurell, 1996). The thickness $w$ of the total nonlinear layer is set by the signal threshold in the interferometric detection.

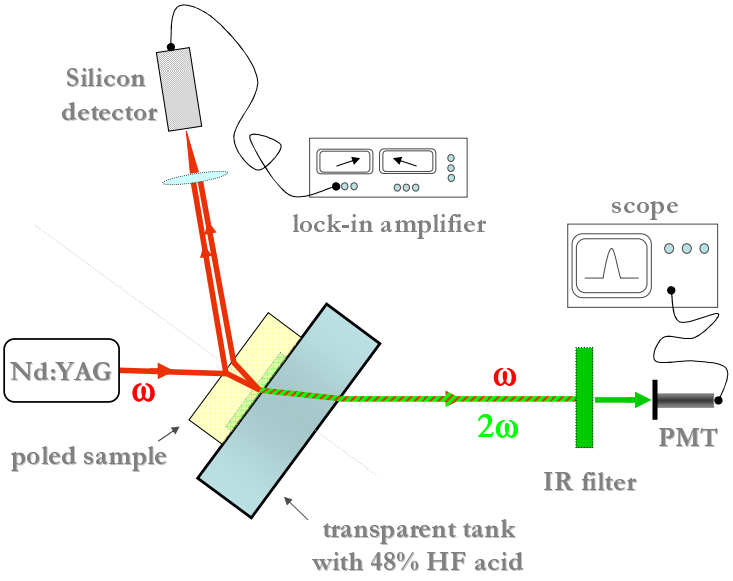


FIGURE 3.5: Layer peeling apparatus. The fundamental light beam ($\omega$) impinges on the sample surface at a fixed angle of incidence. The nonlinear region of the poled glass (*in green*) faces the tank with diluted hydrofluoric acid ($HF$) in. The fundamental light is filtered out before the $SH$ light ($2\omega$) gets detected by the photomultiplier ($PMT$).

The sample inclination angle in Figure 3.5 is conveniently fixed to maximize the contrast of the interference fringes. By simultaneously recording the time evolution of the $SHG$ signal out of the photomultiplier and the signal which comes from the interference of the two reflected $IR$ pump beams at the top and bottom surface of the sample, the removed thickness can be quantified. The evolution of the $SH$ power is thus tracked in real time with a resolution of below $1\,\mu m$, and its amplitude and sign allows a full reconstruction of the nonlinear coefficient, $d$, versus the depth, as follows:

$$P_{2\omega}(z) \approx K_{lp} \left| \int_0^w d(z) exp\left( i \frac{pi}{l_c cos(\vartheta)} z \right) dz \right|^2 \tag{3.9}$$

where

$$K_{lp} = \frac{8\pi \cdot T(\theta_\omega)}{\lambda^2 \epsilon_o c n_{2\omega} n_\omega^2} \left( \frac{P_\omega tan(\theta_\omega)}{\Lambda^2} \right)^2 \tag{3.10}$$

In Equation 3.9 and Equation 3.10, $\lambda$ and $\Lambda$ are the wavelength and beam area of the fundamental light, respectively; $\epsilon_o$ is the vacuum permittivity; $c$ is the light velocity in vacuum; $P_\omega$ is the pump power; $n_\omega$ and $n_{2\omega}$ are the refractive indexes of the glass at fundamental and $SH$ wavelengths, respectively; $\theta_\omega$ is the angle at which the fundamental light and the SH light propagate inside the glass; the angular envelope $T(\vartheta)$ takes in account the Fresnel transmission factors; $w$ is the thickness of the nonlinear layer; $l_c$ is the coherence length. The approximated Equation 3.9 holds in the hypothesis of both pump and $SH$ beams being co-directional and assuming that the remaining nonlinear distribution is unaffected by the etching in progress.

The normalized $SH$ power recorded from two couples of $0.5\,mm$ thick Infrasil silica disks ($\phi = 1\,in$), identically poled for $5\,min$ in air at $250°C$, with $3\,kV$ (*blue*) and $5\,kV$ (*green*) respectively applied to silicon ($p-type$) pressed-on electrodes, are compared in Figure 3.6. The solid lines display the characterization performed *in situ* with the sample continuously etched by layer peeling procedure. A very good agreement is demonstrated when the samples are mounted at the same fixed angle ($53^o$) on the Maker Fringe jig in Figure 3.1 and successive etching steps are repeated at accurate time intervals (dotted in Figure 3.6). The thickness removed each time is thus carefully measured by $\alpha$-step profilometer inspection of the etched area. The normalized $SH$ signal decreases during the etching and reaches the detection threshold for a total removed silica thickness of about 13 and $20\,\mu m$, respectively. The difference in depth is quantitatively predicted by Equation 2.5, where the nonlinear thickness grows with the poling voltage. For the sake of comparison, the relative Maker Fringe patterns are also reported in the inset, giving evidence of similarities in the $\chi^{(2)}$ spatial distribution.

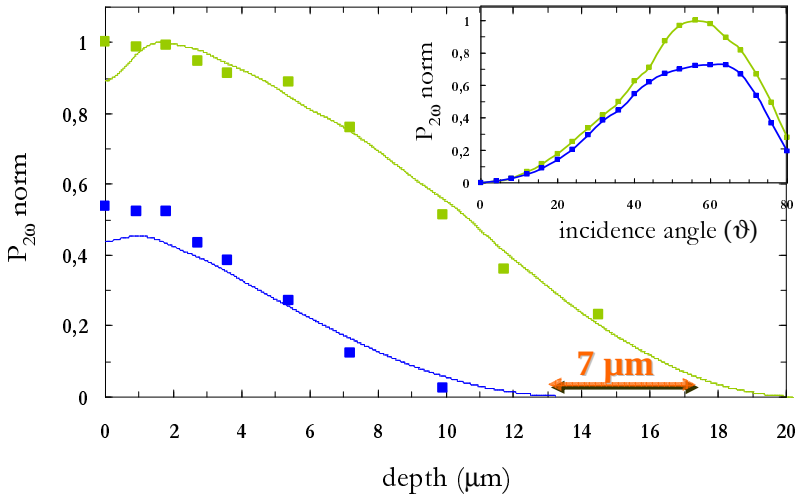


FIGURE 3.6: Evolution of the normalized $SH$ peak power versus etched depth from two couples of Infrasil samples identically poled for $5\,min$ in air at $250°C$, $3\,kV$ (*blue*) and $5\,kV$ (*green*), respectively. Confirmation of good reproducibility between real-time measurements (Lille, as solid line) and discrete data from successive $HF$ etching steps (ORC, dotted). Inset: qualitative comparison of the Maker Fringe curves

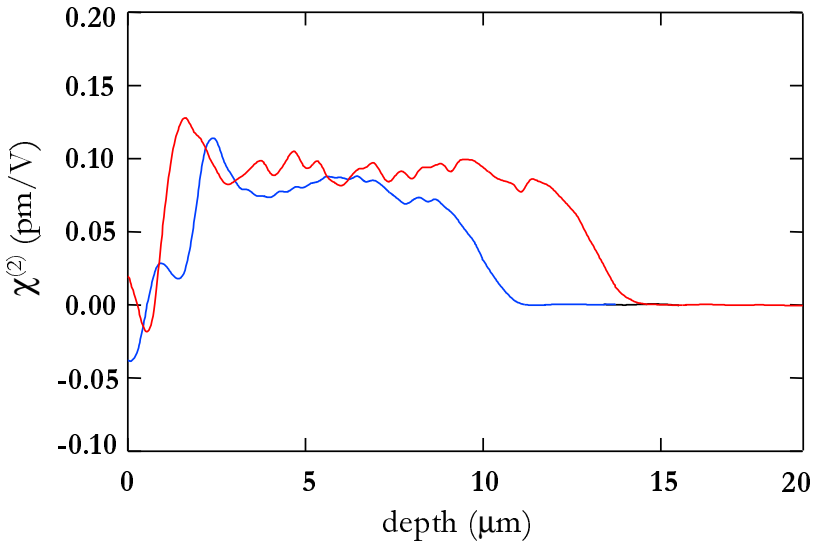


FIGURE 3.7: Reconstructed $\chi^{(2)}$ profile as a function of the depth under the anode of Infrasil samples. Larger nonlinear thickness (about $4\,\mu m$) for higher voltage applied ($3\,kV$ (blue) and $5\,kV$ (red), respectively), as predicted in Equation 2.5

The reconstructed $\chi^{(2)}$ profiles obtained by layer peeling algorithm are plotted in Figure 3.7. In contrast to the Maker Fringe technique, which does not give information about the nonlinear profile, the layer peeling method allows a direct determination of it without any assumption on the microscopic mechanisms at the origin of the nonlinearities and data post-treatment, such as Fourier analysis, genetic algorithm, trials and errors method. Furthermore, although destructive, this method is highly sensitive to sign changes of $\chi^{(2)}$ as well. In fact, its value in Figure 3.7 is found to be initially negative beneath the anode surface and then reverse to finally tail off in the depth. Further investigations are aimed to clarify the reason behind $\chi^{(2)} < 0$, as already reported by Kudlinski et al. (2003b).

Moreover, additional information can be recovered by relating the $HF$ etching rate to the poling induced electric field. In Section 5.2.3 the empirical formula firstly introduced by Lesche et al. (1997) allows the built-in electric field strength to be retrieved, which leads to the determination of the third-order nonlinear susceptibility spatial distribution in Equation 2.9. It would be interesting to confirm in this way the $\chi^{(3)}$ enhancement after poling as already evidenced in Infrasil(Quiquempois et al., 2005b), fibre (Xu et al., 2000a) and recently also in channel waveguides (Garcia et al., 2003).

## 3.4 Spatial mapping of the nonlinearity distribution: scanning optical microscopy

A key role in assessing nonlinear material performance is played by a precise knowledge of the absolute value of the third-rank tensor $\chi^{(2)}_{ijk}$ (Boyd, 1992). In the Maker Fringe

approach (Section 3.2), the estimation of $SON$ coefficients is given by comparative measurements of transmitted $SH$ signal. However, complete characterizations of thin nonlinear films, i.e. measurement of both the nonlinear thickness and coefficient, are not achievable.

Scanning optical microscopy allows an accurate mapping of nonlinear optical parameters through measurements of the reflected $SH$ signal. Reflected second harmonic radiation at the end-face of a noncentrosymmetric material will in general be made up of contributions from both surface and bulk effects. The latter however are predicted to give very small contribution in many cases (Bloembergen and Pershan, 1962). Basically, the $SHG$ signal depends on several parameters, such as the polarization of both the pump beam and the $SH$ detected radiation, the angle of the incident fundamental harmonic and the azimuth angle of anisotropic sample (Shen, 1992). In order to probe the lateral $\chi^{(2)}$ distribution, a normal reflection experimental geometry is adopted as shown in Figure 3.8, where the sample is scanned through the focus of an infrared laser beam in a second harmonic generation setup and the $SH$ intensity is monitored stepwise.

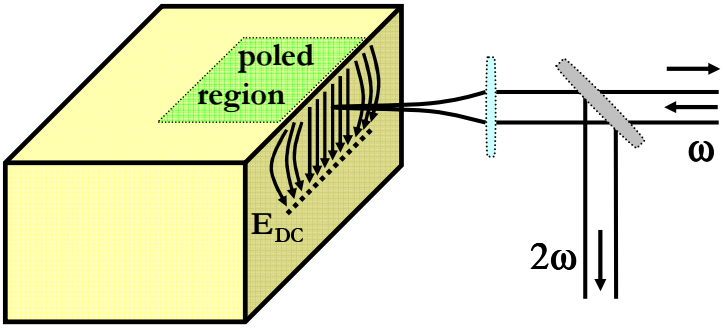


FIGURE 3.8: Geometry adopted for second harmonic scanning optical microscopy (*SHSOM*) in reflection and schematic of the cleaved sample. In the poled region, lying underneath the anodic area (top surface), the field lines of the induced electrostatic field ($E_{DC}$) are sketched

High resolution mapping can be achieved using high $NA$ microscopy objectives for the illumination of the poled region under investigation. This direct investigation provides a $SH$ signal whose square root is proportional to the local optical nonlinearity $\chi^{(2)}$, and allows the evaluation of poling inhomogeneities due to high field poling and field distortions at the edge of poling electrodes. For these reasons, second harmonic scanning optical microscopy ($SHSOM$) is widely used as a nondestructive and noncontact probe (Heinz, 1991). Moreover, spatially resolved detection of second harmonic radiation has several advantages, such as the capability to resolve nonlinear thickness as small as $1\,\mu m$ with sub-micron resolution and to probe the morphology of the surface molecular layers with remarkable sensitivity to interface properties.

Finally, *SHSOM* can return the absolute value of the second order generated signal by calibrating the technique response and comparing it with the reflected signal from a reference sample of known nonlinearity. Since the experiments are carried out by monitoring the modification of *SH* signal itself, extra care is required to minimize contributions from multiple or back reflections. More details are given in the next section.

### 3.4.1 Calculating the surface second order generated signal

In investigations of surfaces and surface phenomena by *SHG*, the intensity and polarization properties of the second harmonic are measured in reflection as a function of parameters such as the polarization, wavelength, and angle of incidence of the fundamental. To determine the effective $d$ coefficient, it is necessary to compare the reflected *SH* intensity from the sample with that generated by a well-characterized reference material; however, to extract the surface nonlinear susceptibility tensor or alternatively to predict the outcome of an experiment, a suitable theoretical framework is needed.

The first approach to the problem was due to Bloembergen and Pershan (1962), who considered the nonlinear optical properties of a material slab that, in the limit of zero thickness, could be taken as a model for a surface. In what follows, a Green-function approach (Sipe, 1987) based on $s$ and $p$ components of the electromagnetic field has been applied to describing *SHG* from planar surfaces.

To model the electromagnetic properties of the surface, it is worth first considering a polarization sheet (oscillating at some frequency $\omega$) of the form

$$\vec{P}^{\omega}(\vec{r},t) = \vec{\Gamma}\delta(z)e^{i(\vec{\alpha}\cdot\vec{R}-\omega t)} + c.c. \tag{3.11}$$

where $\vec{R} = (x, y)$. Assuming that the polarization sheet, whose linear optical properties we neglect in calculating the fundamental field, is embedded in a uniform medium of (complex) refractive index $n$, it has been shown in detail (Sipe, 1987) that the solution of the Maxwell equations with a source term (Equation 3.11) can be written, at point $z \neq 0$, as

$$\vec{E}(\vec{r},t) = \vec{E}(\vec{r})e^{-i\omega t} + c.c. \tag{3.12}$$

and

$$\vec{E}(\vec{r}) = \vec{E}_{+}(\vec{r})\Psi(z) + \vec{E}_{-}(\vec{r})\Psi(-z) \tag{3.13}$$

where $\Psi(z)= 0, 1$, as $z < 0$ or $z > 0$ respectively.

Here

$$\vec{E}_{\pm}(\vec{r}) = [E_{s\pm}\hat{s} + E_{p\pm}\hat{p}_{\pm}]e^{i\vec{k}_{\pm}\cdot\vec{r}} \tag{3.14}$$

corresponds, respectively, to an upward and downward propagating wave of wave vector

$$\vec{k}_{\pm} = \vec{\alpha} \pm \beta\hat{z} \tag{3.15}$$

with

$$k_{\pm} = n\tilde{\omega} = (\alpha^2 + \beta^2)^{1/2}. \tag{3.16}$$

The unit vectors specifying the $s$ and $p$ polarization components in Equation 3.14 are given by

$$\hat{s} = \hat{\alpha} \times \hat{z} \tag{3.17}$$

and

$$\hat{p}_{\pm} = (\alpha\hat{z} \mp \beta\hat{\alpha})/(n\tilde{\omega}) \tag{3.18}$$

even if $n$ or $\beta$ is complex. The $s$ and $p$ components of the wave were shown (Sipe, 1987) to be given by

$$E_{s_{\pm}} = \frac{2\pi i\tilde{\omega}^2}{\beta}\hat{s} \cdot \vec{\Gamma} \tag{3.19}$$

$$E_{p_{\pm}} = \frac{2\pi i\tilde{\omega}^2}{\beta}\hat{p}_{\pm} \cdot \vec{\Gamma} \tag{3.20}$$

From Equation 3.15 - 3.16, $\vec{\alpha}$ is the component of the wave vector in the $\hat{x} - \hat{y}$ plane sketched in Figure 3.9, and $\beta$ is the possibly complex component perpendicular to the plane. For a nonabsorbing medium ($n$ real), if $\alpha < n\tilde{\omega}$, Equation 3.14 describes a plane wave propagating upward through the medium, its wave vector making an angle $\theta = \sin^{-1}(\alpha/\tilde{\omega}n)$ from the $\hat{z}$ axis. The upward wave is illustrated in Figure 3.9, where the $\hat{s}$ and $\hat{p}_+$ directions are also indicated.

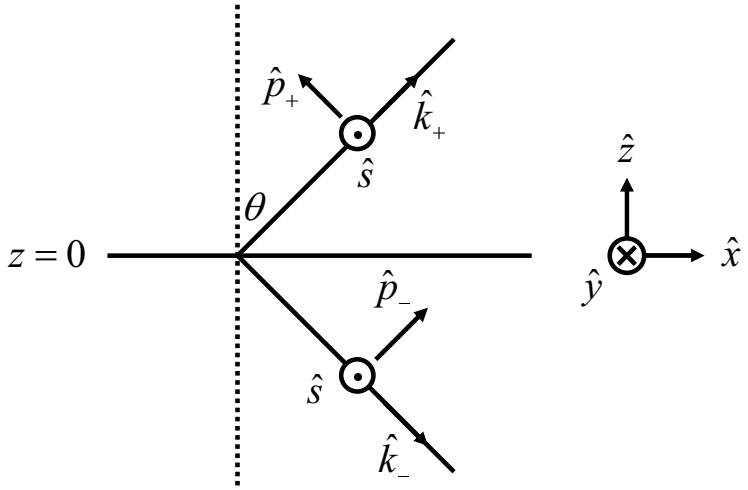


FIGURE 3.9: The coordinate systems used to describe the solutions of the Maxwell equations. The polarization sheet is located at the $z = 0$ plane. The case $\hat{\alpha} = \hat{x}$ is illustrated, although in general $\hat{\alpha}$ lies in the $\hat{x} - \hat{y}$ plane.

To use the resulting equations to describe *SHG*, henceforth $\omega$ will exclusively denote the fundamental frequency and $\vec{\alpha}$ the component of the incident wave vector parallel to the surface (i.e. $\hat{\alpha} = \hat{x}$). Furthermore, we treat the region that contributes to surface *SHG* as an induced nonlinear polarization sheet sitting in the vacuum at $z = 0^+$ (see Equation 3.11), just above a thick slab of linear dielectric medium of dielectric constant $\epsilon$ [where, in general, $\epsilon(\omega) \neq \epsilon(2\omega)$]

$$\vec{P}^{2\omega}(\vec{r}, t) = \vec{P}^{2\omega}(\vec{R})\delta(z - 0^+)e^{(-2i\omega t)} + c.c. \tag{3.21}$$

The slab is presumed to fill the space form $z = 0$ to $z = -S$ in Figure 3.10, and the polarization sheet is induced by a surface nonlinear susceptibility tensor $\vec{\chi}^{(s)}$,

$$\vec{P}^{2\omega}(\vec{R}) = \vec{\chi}^{(s)} : \vec{E}^{\omega}(\vec{R}, z = 0^-)\vec{E}^{\omega}(\vec{R}, z = 0^-) \tag{3.22}$$

where the fundamental electric field is given by

$$\vec{E}^{\omega}(\vec{r}, t) = \vec{E}^{\omega}(\vec{r})e^{-i\omega t} + c.c. \tag{3.23}$$

In keeping with the usual convention, $\vec{\chi}^{(s)}$ is defined with respect to the electric field at $z = 0^-$ just inside the linear substrate. This definition is not essential, and a convention in which $\vec{\chi}^{(s)}$ is defined with respect to the vacuum field would lead to a rescaling of the component of the $\vec{\chi}^{(s)}$. Also, it is assumed that only one surface is active in *SHG*; if necessary, the theory can be extended to consider even more general cases.

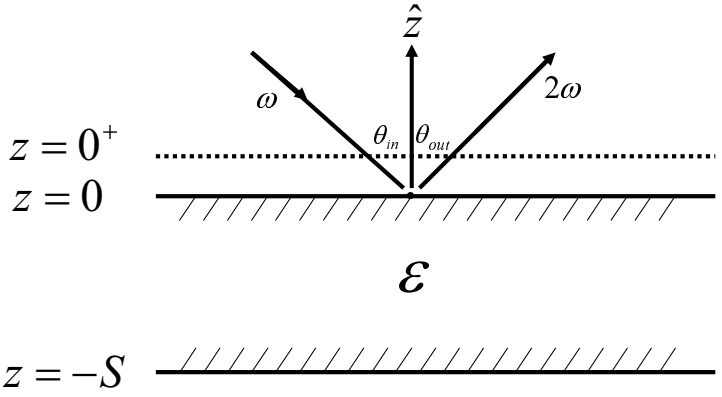


FIGURE 3.10: Standard reflection geometry used in surface *SHG* from a thick slab. Assuming the coordinate system of Figure 3.9, the nonlinear polarization sheet lies in the $z = 0^+$ plane.

We take for the moment the incident beam to be represented by a plane wave, so the fundamental field is of the form

$$\vec{E}^{\omega}(\vec{r}) = \vec{E}^{\omega}(\vec{r})e^{i\vec{\alpha}\cdot\vec{R}} + c.c. \tag{3.24}$$

and the formalism of Equation 3.12 - 3.20 may be used to calculate the field generated simply by replacing the lowercase symbols with the uppercase. Therefore, the nonlinear generated polarization is oscillating at frequency $\Omega \equiv 2\omega$ and will be characterized by a wave vector parallel to the surface $\vec{A} \equiv 2\vec{\alpha}$. Moreover, the polarization sheet is in vacuum ($n = N = 1$), but the optical properties of the nearby substrate must be taken into account: a full set of complex Fresnel transmission and reflection coefficients will be introduced accordingly, as listed in Table 3.1.

In Figure 3.10, the fundamental field incident from the vacuum (subscript $o$) is given by

$$\vec{E}^{\omega}_{in}(\vec{r}) = [E^{s}_{in}\hat{s} + E^{p}_{in}\hat{p}_{o-}]e^{[i(\alpha x - \beta_o z)]} \tag{3.25}$$

with $\tilde{\omega}^2 = \alpha^2 + \beta_o^2$. The linear field in the medium (subscript $m$) is then (from Equation 3.25)

$$\vec{E}^{\,\omega}(\vec{r}) = [E^{s}_{in}t^{s}_{om}\hat{s} + E^{p}_{in}t^{p}_{om}\hat{p}_{-}]e^{[i(\alpha x - \beta z)]} \tag{3.26}$$

where $t^{s(p)}_{ij}$ is the Fresnel transmission coefficient for $s$ ($p$) polarized fundamental crossing from medium $i$ to medium $j$. Also relating the notation, we have allowed for the change in direction of the wave by replacing $\hat{p}_{o-}$ with $\hat{p}_{-}$ and $\beta_o$ with $\beta$, where now $\epsilon(\omega)\tilde{\omega}^2 = \alpha^2 + \beta^2$. The $\hat{x} = \hat{\alpha}$ component of the wave vector does not change in crossing the boundary because of the translational invariance in the plane. In addition, we can reasonably ignore the reflection at the $z = -S$ interface for a thick slab, since we may expect a clear separation from the front and back surface reflections when using a laser (confined beam) light source. However, this assumption would not hold for a thin film substrate, where multiple reflections must be included.

We can identify

$$\vec{E}^{\,\omega}(x, z = 0^{-}) = [E^{s}_{in}t^{s}_{om}\hat{s} + E^{p}_{in}t^{p}_{om}\hat{p}_{-}]e^{i\alpha x} = \vec{e}^{\,\omega}\,|E_{in}|\,e^{i\alpha x} \tag{3.27}$$

where

$$\vec{e}^{\,\omega} = [\hat{s}t^{s}_{om}\hat{s} + \hat{p}_{-}t^{p}_{om}\hat{p}_{o-}] \cdot \hat{e}^{in} \tag{3.28}$$

Putting this expression in the Equation 3.21, we can write

$$\vec{P}^{2\omega}(\vec{r}) = \vec{\chi}^{(s)} : \vec{e}^{\,\omega}\vec{e}^{\,\omega}|E_{in}|^2\delta(z - 0^{+})e^{2i\alpha x} = \vec{\Gamma}\delta(z - 0^{+})e^{iAx} \tag{3.29}$$

where

$$\vec{\Gamma} = \vec{\chi}^{(s)} : \vec{e}^{\,\omega}\vec{e}^{\,\omega}|E_{in}|^2 = \vec{p}|E_{in}|^2 \tag{3.30}$$

Now we can calculate the upward propagating second harmonic field that is generated by the nonlinear polarization sheet. Two contributes need to be considered. First, there is the directly generated upward propagating wave, which is given in terms of the nonlinear polarization (Equation 3.29) by Equation 3.14 with Equation 3.17 - 3.19. Second, part of the downward propagating wave, given by Equation 3.14 with Equation 3.17, 3.18

and 3.20, will be reflected upward by the first vacuum-substrate interface at $z = 0$ (still ignoring reflection at the $z = -S$ interface). Combining these two contributions, we have, from the equations indicated above,

$$\vec{E}^{2\omega}(\vec{r},t) = \vec{E}^{2\omega}(\vec{r})e^{-i\Omega t} + c.c. \tag{3.31}$$

where the the second harmonic field reflected upward at $2\omega$ is given by

$$\vec{E}^{2\omega} = \frac{2\pi i\tilde{\Omega}^2}{B_o}\vec{H}^o \cdot \vec{\Gamma} e^{i(Ax+B_o z)} \tag{3.32}$$

with

$$\vec{H}^o = [\hat{S}(1+R^s_{om})\hat{S} + \hat{P}_{o+}(\hat{P}_{o+} + R^p_{om}\hat{P}_{o-})] \tag{3.33}$$

In keeping with our notational convention, $R^{s(p)}_{om}$ is the Fresnel coefficient for reflection to the medium $m$ of the second-harmonic wave in vacuum, for $s$ ($p$) polarized light, respectively; likewise, $\hat{P}_{o-}$ indicates the unit vector for $p$ polarized wave propagating downward in the vacuum at $\Omega = 2\omega$. The component of the wave vector of the second-harmonic wave in the plane of the surface is the same as for the induced nonlinear polarization wave, and the well-known result that the second-harmonic wave is emitted at the specular reflection angle follows; this conclusion does not hold if the vacuum is replaced by a dispersive medium. If denoting with $\hat{e}^{out}$ the polarization component of the second-harmonic beam which is chosen for detection, thus the amplitude is

$$E^{2\omega} = \frac{2\pi i\tilde{\Omega}^2}{B_o}\hat{e}^{out} \cdot \vec{H}^o \cdot \vec{\Gamma} = \frac{2\pi i\tilde{\Omega}^2}{B_o}\vec{e}^{2\omega} \cdot \vec{\Gamma} \tag{3.34}$$

Then

$$\left|E^{2\omega}\right|^2 = \frac{4\pi^2\tilde{\Omega}^4}{B_o^2}\left|\vec{e}^{2\omega} \cdot \vec{\Gamma}\right|^2 = 4\pi^2\frac{\tilde{\Omega}^4}{B_o^2}\left|\vec{e}^{2\omega} \cdot \vec{p}\right|^2 |E_{in}|^4 \tag{3.35}$$

Since the vacuum is dispersionless,

$$\left(\frac{\tilde{\Omega}}{B_o}\right)^2 = \left(\frac{\tilde{\omega}}{\beta_o}\right)^2 = \left(\frac{1}{\cos\theta_{in}}\right)^2 = \sec^2\theta_{in} \tag{3.36}$$

where $\theta_{in}$ is the angle between the wave vector of the incident fundamental and the surface normal, as indicated in Figure 3.10. Also indicated in Figure 3.10 is $\theta_{out}$, which is the angle between the wave vector of the detected second-harmonic wave and the surface normal. Obviously, in the normal reflection geometry $\theta_{in} = \theta_{out} = 0°$. Now, using $\tilde{\Omega}^2 = 4\omega^2/c^2$ and inserting Equation 3.36 into Equation 3.35, it is found that:

$$\frac{c}{2\pi}\left|E^{2\omega}\right|^2 = \frac{32\pi^3\omega^2}{c^3}\sec^2\theta_{in}\left|\vec{e}^{2\omega} \cdot \vec{p}\right|^2\left(\frac{c}{2\pi}|E_{in}|^2\right)^2 \tag{3.37}$$

Because our analysis starts from a plane wave incident upon the surface, we introduce an area ($\Lambda$) normal to the Poynting vector of the incident beam. Then, by defining $P_\omega$

as the power incident through this area and $P_{2\omega}$ as the corresponding second-harmonic power generated, we obtain

$$P_{2\omega} = \frac{32\pi^3\omega^2}{c^3\Lambda}\sec^2\theta_{in}\left|\vec{e}^{2\omega}\cdot\vec{p}\right|^2 P_\omega^2 = \frac{32\pi^3\omega^2}{c^3\Lambda}\sec^2\theta_{in}\left|\vec{e}^{2\omega}\cdot\vec{\chi}^{(s)}:\vec{e}^{\,\omega}\vec{e}^{\,\omega}\right|^2 P_\omega^2 \quad (3.38)$$

since here $\Lambda$ is also the area normal to the Poynting vector of the second-harmonic beam. The Equation 3.38 gives the second-harmonic power from a surface as a function of such parameters as $\theta_{in}$, the polarization of the fundamental, and the observed polarization of the second harmonic.

For a Gaussian laser beam (Boyd, 1992) of radius $r_o$, a simple geometric argument shows that we may, for small $\theta_{in}$, replace $\Lambda$ with $\pi r_o^2$ if the beam waist intersects the surface. The second harmonic power calculated as a function of the effective nonlinear optical coefficient $d_{eff} = \frac{1}{2}\left|\vec{e}^{2\omega}\cdot\vec{\chi}^{(s)}:\vec{e}^{\,\omega}\vec{e}^{\,\omega}\right|$ is plotted in Figure 3.11 for a specific value of the fundamental harmonic average power $\bar{P}_\omega$.

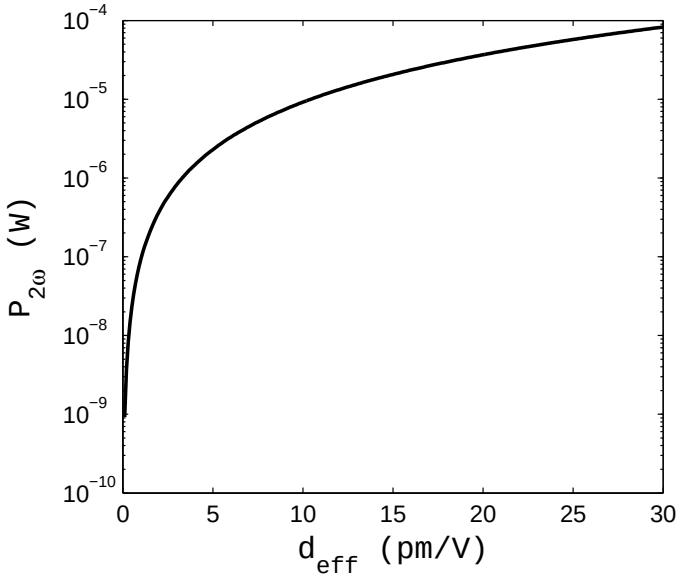


FIGURE 3.11: Reflected $P_{2\omega}$ versus $d_{eff} = 1/2\cdot\chi^{(s)}$, given $\theta_{in} \cong 0°$ for a tightly confined focused beam, $\omega = 2\pi c/\lambda = 17.7\times10^{14}\,Hz$, $r_o = 4\,\mu m$, $\bar{P}_\omega = 0.2\,W$.

To evaluate $P_{2\omega}$ correctly, we need the appropriate Fresnel coefficients that go into the $\vec{e}^{\,\omega}$ and $\vec{e}^{2\omega}$ expressions, and these are compactly presented in Table 3.1. These expressions are valid even if the dielectric constant is complex.

An explicit representation for these Fresnel coefficients can be obtained by substituting

$$\beta_o = \tilde{\omega}\cos\theta_{in} \quad (3.39)$$

$$B_o = \tilde{\Omega}\cos\theta_{in} \quad (3.40)$$

$$\beta = \tilde{\omega}[\epsilon(\omega) - \sin^2\theta_{in}]^{1/2} \quad (3.41)$$

| **At** $\omega$ | **At** $\Omega = 2\omega$ |
|---|---|
| $r_{ij}^{s} = \dfrac{\beta_i - \beta_j}{\beta_i + \beta_j}$ | $R_{ij}^{s} = \dfrac{B_i - B_j}{B_i + B_j}$ |
| $r_{ij}^{p} = \dfrac{\beta_i \epsilon_j(\omega) - \beta_j \epsilon_i(\omega)}{\beta_i \epsilon_j(\omega) + \beta_j \epsilon_i(\omega)}$ | $R_{ij}^{p} = \dfrac{B_i \epsilon_j(2\omega) - B_j \epsilon_i(2\omega)}{B_i \epsilon_j(2\omega) + B_j \epsilon_i(2\omega)}$ |
| $t_{ij}^{s} = \dfrac{2\beta_i}{\beta_i + \beta_j}$ | $T_{ij}^{s} = \dfrac{2B_i}{B_i + B_j}$ |
| $t_{ij}^{p} = \dfrac{2\beta_i [\epsilon_i(\omega)\epsilon_j(\omega)]^{1/2}}{\beta_i \epsilon_j(\omega) + \beta_j \epsilon_i(\omega)}$ | $T_{ij}^{p} = \dfrac{2B_i [\epsilon_i(2\omega)\epsilon_j(2\omega)]^{1/2}}{B_i \epsilon_j(2\omega) + B_j \epsilon_i(2\omega)}$ |

TABLE 3.1: Fresnel coefficients

$$B = \tilde{\Omega}[\epsilon(2\omega) - \sin^2\theta_{in}]^{1/2} \tag{3.42}$$

Experimentally, to obtain an absolute measurement of the effective surface nonlinear susceptibility tensor $\vec{\chi}^{(s)}$, the reflected $SH$ signal from the sample given by the Equation 3.38 is normalized to the reflected $SH$ signal generated by a well characterized reference material, such as quartz or $LiNbO_3$. In the latter case, the reflected $SH$ power from the $LiNbO_3$ to be compared with would accordingly be given by

$$P_{2\omega,ref} = \frac{32\pi^2\omega^2}{c^3 r_{o,ref}^2} \sec^2\theta_{in,ref} \left| \vec{e}^{\,2\omega} \cdot \vec{\chi}^{(s)} : \vec{e}^{\,\omega}\vec{e}^{\,\omega} \right|_{ref}^2 P_{\omega,ref}^2 \tag{3.43}$$

where subscript *ref* stands for reference material.

### 3.4.2 Reflection second harmonic generation scanning: apparatus

A scanning optical microscopy geometry provides a non-destructive tool to bidimensionally map second harmonic generation occurring during normal reflection from the cleaved end-face of the sample, as represented in Figure 3.12. In particular *SHG* microscopy reveals the profile of the induced *SON* along the coordinate parallel to the poling field (y axis in figure).

The *Nd:YAG* laser, Q-switched and actively mode locked at $76\,MHz$, delivers 24 pulses of duration $\tau \cong 300\,psec$ with a repetition rate $f = 1004\,Hz$. The average power $\bar{P}$ is about $3\,W$ and the peak power of each pulse under this condition is $P \cong 400\,kW$, requisite to reveal the non-linear response of the medium. The polarization state of the fundamental beam ($\lambda = 1.064\,\mu m$) may be varied with respect to the plane of incidence

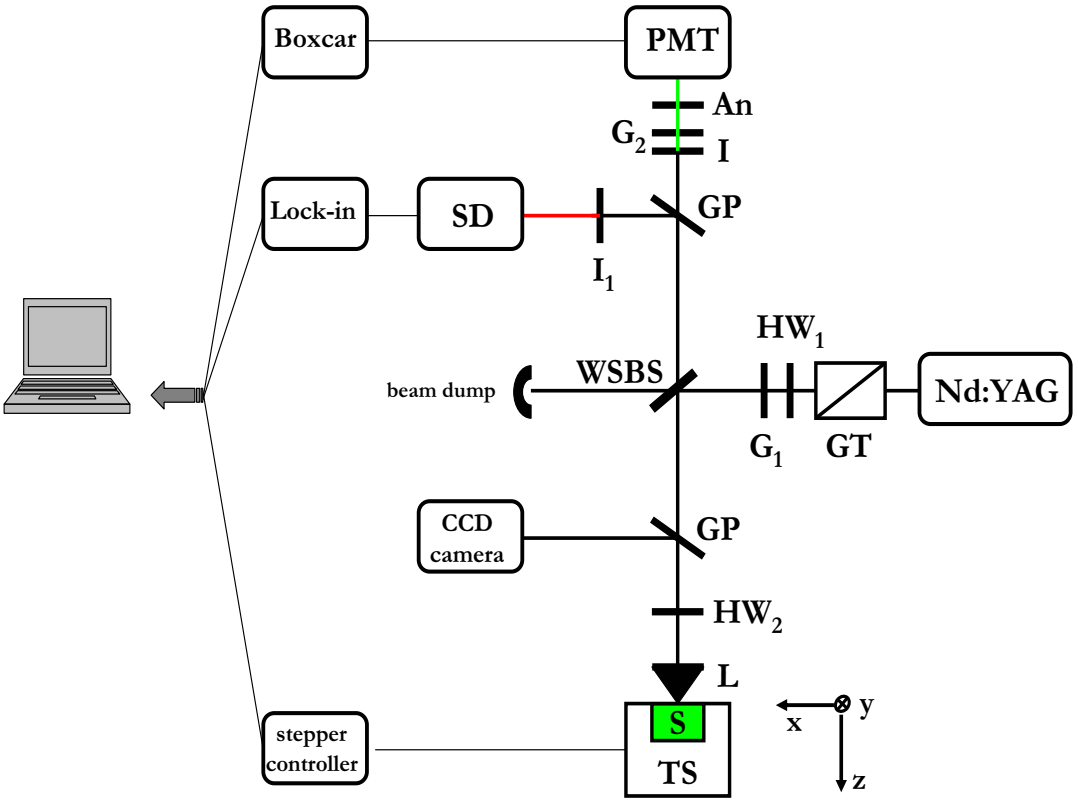


FIGURE 3.12: Experimental layout for the scanning of *SHG* along the direction of the poling field.

by rotating a Glan-Thomson polariser ($GT$) and half-wave plate ($HW_1$) combination. The set-up allows detection of $SHG$ signal for all combinations of $s$ and $p$ polarizations, i.e. perpendicular and parallel to the y axis, respectively. By setting a polariser ($HW_2$) in the optical path of the pump beam, and an analyser ($An$) in the optical path of the reflected $SH$ beam, an accurate map of the effective nonlinear susceptibility tensor $\chi^{(2)}$ can be obtained. For clarity, $p-pol$ electric field only will be considered here. The linearly polarized incident excitation is perpendicularly focused onto the end-face of the sample ($S$) through an achromatic high magnification microscope objective ($L$). After a close scan of the cross section, both the reflected first harmonic ($FH$) and $SH$ generated beams are collected by the same objective lens as they are returned and travel parallel to each other, coupled by the $d_{33}$ nonlinear coefficient of the sample. A residual fraction of the reflected fundamental beam passes through the wavelength selective beam splitter (*WSBS*): then, it is reflected from a glass plate (*GP*) into a silicon detector (*SD*) masked with a $1.064\,\mu m$ bandpass filter ($I_1$). $FH$ signal, i.e. linear reflectivity of the sample, is monitored by the lock-in amplifier and recorded as a function of the scanning coordinate in order to determine the position of the air/sample interface. In the same way, after spectral selection by an appropriate set of interference filter ($G_2$) (minimum peak transmission of 50% at $532 \pm 2\,nm$) and infrared-extinguishing filters ($I$), the $SH$ radiation intensity is detected by means of the photomultiplier tube (*PMT*) and analyzed

with a gate integrator. As shown in Figure 3.11, the actual reflected second harmonic signal requires a very sensitive photon counting system to be used. Depth probing of the nonlinearity is performed using a computer controlled bidimensional translation stage (*TS*): the end-face sample is held perpendicularly in the focal plane of the microscope and subsequently scanned with an independent X-Y stepper motor driven stage of $0.1\,\mu m$ spatial resolution. The lateral resolution is limited by both the cleaved surface state (critical at the sharp edge) and the diameter of the probing beam at the lens working distance. The theoretical diffraction limit set by the Rayleigh criterion for the lateral resolution ($\Delta x$) is given by:

$$\Delta x \cong 1.22 \cdot \frac{\lambda}{2 \times NA} \tag{3.44}$$

For $\lambda = 1.064\,\mu m$ with standard microscope objectives corrected at infinity, the resolutions are $\Delta x \cong 0.81\,\mu m$ $(63\times, NA = 0.80)$; $\Delta x \cong 0.99\,\mu m$ $(40\times, NA = 0.65)$ and $\Delta x \cong 2.59\,\mu m$ $(10\times, NA = 0.25)$, respectively. Having such a small focus would lead to increase the intensity of the incidence light and, in order to avoid thermal damage of the sample end face, it is necessary to find a compromise with the maximum fundamental power in use. However, the experimental spot sizes are usually bigger since the numerical aperture is not completely filled, the incident beam diameter ($\phi \cong 1.48\,mm$ by knife-edge measurement) being smaller than the objective diameter ($\phi \cong 5.64\,mm$). A beam expander can be added.

To optimize the objective surface distance and guarantee experimental reproducibility, the width of the reflected FH beam can be monitored with a *CCD* camera sitting at the distance of $0.3\,m$ from the sample. In this way, the field intensity at the end face, and consequently the *SHG* efficiency, can be maximized and the spatial resolution in both *FH* and *SH* images improved. The influence of the other field components, besides the one fixed by the half wave plate, would be theoretically negligible, although it ought to be borne in mind that even an ideal focusing might create a complicated field distribution with all field components being non-zero (Mansuripur, 1992). In the next section some of the most significant results are briefly outlined.

### 3.4.3 Second order nonlinearity profile measurements: calibration

In order to assess whether the signal to noise ratio of the photon counting system in Figure 3.12 is high enough to detect second harmonic reflected powers $P_{2\omega}$, a preliminary calibration test was carried out.

A $1\,mm$ thick z-cut quartz crystal (crystallographic class 32) of well known nonlinearity is used to validate the sensitivity of the scanning optical microscopy apparatus. The position of the air/sample interface is determined in Figure 3.13 by the fundamental signal (*red squares*) reflected back from the z-cut quartz facade. A spatial resolution of less than $1.5\,\mu m$ can be inferred from this response versus depth. Subsequently, reflection

second-harmonic generation as a function of the vertical translation is also measured and plotted for three different values of the orthogonally polarized pump power: their average intensities scale with the square of the fundamental power, as emerged from Equation 3.38. Fluctuations around the intensity average value are due to the quality of the sample surface, which was carefully polished before the measurement.

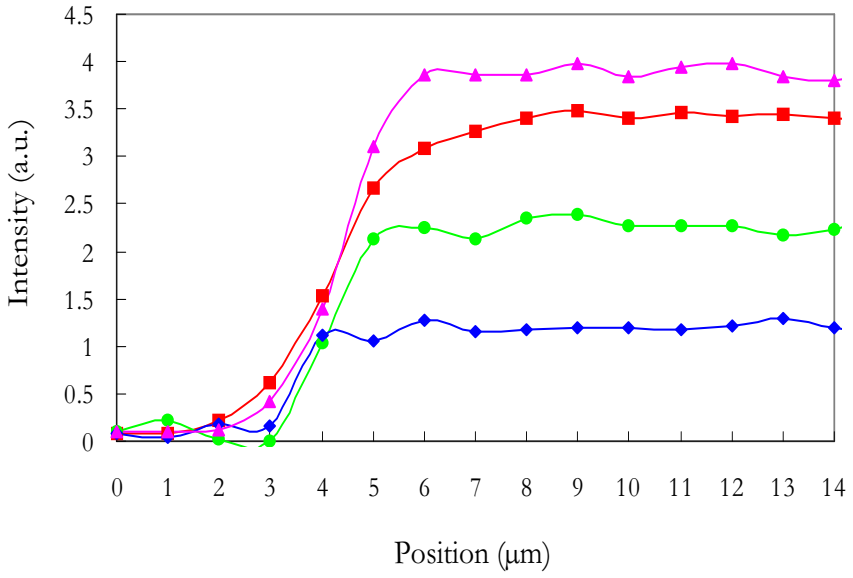


FIGURE 3.13: *IR* reflected pump (*red squares*) from a z-cut quartz crystal and *SH* intensity profile versus position for *FH* intensity of 150 $mW$ (*blue diamonds*), 200 $mW$ (*green circles*), and 250 $mW$ (*pink triangles*), respectively. *SHG* squares with the fundamental pump power.

Considering the value of the tensorial coefficient $d_{11} = 0.30 \pm 0.01\, pm/V$ at $\lambda = 1.064\, \mu m$ for the z-cut quartz nonlinearity (Hagimoto and Mito, 1995), the results show that the apparatus in Figure 3.12 is indeed suitable to measure spatial modifications of $\chi^{(2)}$ at least comparable to $0.1\, pm/V$, in good agreement with the order of magnitude of the most reported values of second order nonlinearity generated in thermally poled silica bulk (see Section 1.1). Furthermore, higher power levels improve the signal to noise ratio, although a trade-off will exist between undesirable damage caused by the high intensity irradiation and enhancement of the signal detection.

In order to establish the *SHSOM* technique for waveguides, more calibration tests are carried out to measure *SON* in guided-wave nonlinear optical devices. In particular, this detection tool is employed to inspect the second order nonlinear optical properties of as-exchanged and annealed proton-exchanged (*APE*) waveguides in $LiNbO_3$. The study, carried out using waveguides fabricated by Dr. Gallo from the ORC, aimed to gain further insight towards optimizing the design and fabrication process. The nonlinear properties of *APE* $LiNbO_3$ waveguides, strongly reduced after the initial proton-exchange, were found to be restored and even increased after annealing (Korkishko et al., 2000). However, the authors claimed that this apparent increase of the nonlinearity was

accompanied by a strong degradation of the quality of the second-harmonic generation reflected beam in the region of initial waveguides due to beam scattering.

The measurement of harmonic power $P_{2\omega}$ in both the exchanged and unexchanged region by edge scanning is thus well-suited to compare the waveguide nonlinearity with its substrate value. The polished cross section is here exposed to an average $FH$ power of only $10\,mW$, low enough to guarantee second order signal generation in reflection and at the same time to avoid thermal damage at the surface, whose optical damage threshold is $100MW/cm^2$, about three order of magnitude lower than silica-based materials. A detailed $30x30\mu m^2$ map of both $IR$ (*left hand side*) and $SH$ reflected signal (*right hand side*) from a channel ion-exchange waveguide in z-cut $LiNbO_3$ is shown in Figure 3.14.

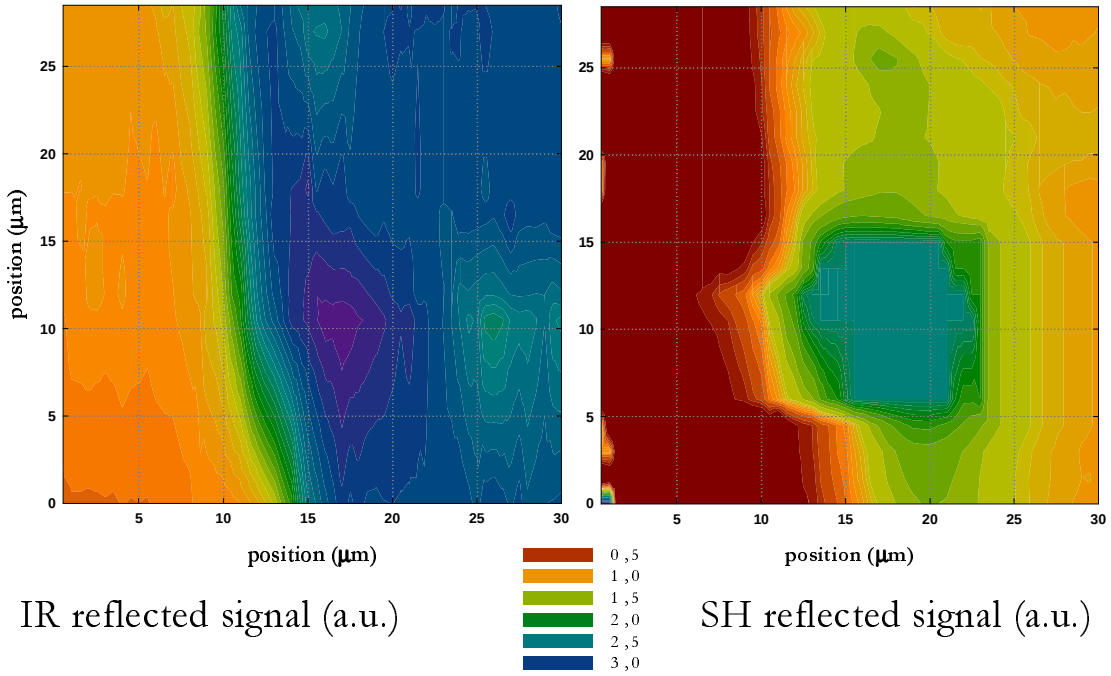


FIGURE 3.14: $2D$ distribution of both $IR$ (left hand side) and $SH$ reflected signal (right hand side) from the polished end-face of a channel waveguide in $LiNbO_3$. The measurement of reflection second harmonic generation from the $PE$ and unexchanged region by scanning optical microscopy can be used to compare the waveguide nonlinearity with the substrate value.

The second harmonic signal generated in reflection from the bulk of the crystal (green in Figure 3.14) shows a good signal to noise ratio. However, saturation of the detection system is experienced when the guiding zone is scanned, which prevents quantitative estimation of the $SH$ signal generated there. Unexpectedly, a reflected nonlinear optical coefficient ten times higher than the bulk of the same sample is measured on the ion-exchanged area, which cannot be due to nonlinearity effectively recovered by the reverse proton-exchange technique. Some other effects, such as scattering and/or back reflection, may disturb the contribution from the genuine $SON$ in the guiding region.

In confirmation, the $IR$ reflected pump on the left in Figure 3.14 shows higher signal in correspondence to the guiding channel than in the whole bulk.

In conclusion, the scanning optical microscopy allows very accurate direct detection of surface second order nonlinearity although it may be sensitive to spurious signal coupled in guiding region as well, which turns out to be a drawback to take in account of when investigating waveguiding devices (Arentoft et al., 2000b). More experimental investigations are given in the next section, where the scanning optical microscopy is used to detect the second harmonic signal generated in thermally poled twin-hole fibres, and further clarification of the effects of a waveguide upon measurements is achieved.

### 3.4.4 Twin-hole poled fibre

Scanning microscopy analysis of second order nonlinearity distribution is employed in this section to optimize the spatial overlap between the nonlinear coefficient and light guided in the core region of poled twin-hole fibres.

The twin-hole fibre geometry is specifically designed for poling. The electrodes can be inserted in the two holes running both sides of the core. High voltage is safely applied to the electrodes during poling thanks to silica insulation. Moreover, the fibre can be conveniently cleaved after poling, to reveal the local distribution of the poling induced nonlinearity at the cross section. Specifically, the ability to tailor the poling conditions through direct investigation of $SH$ optical efficiency is very advantageous when it comes to optimizing $\chi^{(2)}$ in the core of the fibre. To date, modest linear $EO$ coefficients are reported ($r \cong 0.3pm/V$), nonetheless competitive conversion efficiencies are achieved by taking advantage of long interaction length in quasi-phase-matched poled fibres (Corbari et al., 2005) and by pumping with peak power as high as few $kW$ (Pruneri et al., 1999a), given the damage threshold of $10GW/cm^2$ in silica-based materials. The twin-hole fibre used for this work was fabricated by the Silica Group at the ORC (Figure 3.15).

The core is asymmetrically positioned $\approx 2\,\mu m$ away from one of the holes to maximize the interaction between the poling induced $DC$ field and the guided optical field. The core is $4\,\mu m$ in diameter and the edge to edge separation between the holes is $12\,\mu m$. The fibre $NA = 0.26$ is chosen to improve the confinement of the $1550\,nm$ single mode to the heavily Ge-doped core. This would lead to higher power density of the fundamental mode, and improved overlap between fundamental and $SH$ modes. The device diameter of $125\,\mu m$ allows easy splicing with standard telecom fibre $SMF28$, and the hole diameter allows for gold plated tungsten electrodes ($\phi = 25\,\mu m$) to be inserted and voltage to be uniformly applied during poling.

To asses whether the $SHSOM$ technique is capable to resolve the nonlinearity profile, thermal poling in air is carried out at $280°C$ for $1\,min$ with $3.2\,kV$ applied to the electrode closest to the core, as schematically shown at the top right in Figure 3.16.

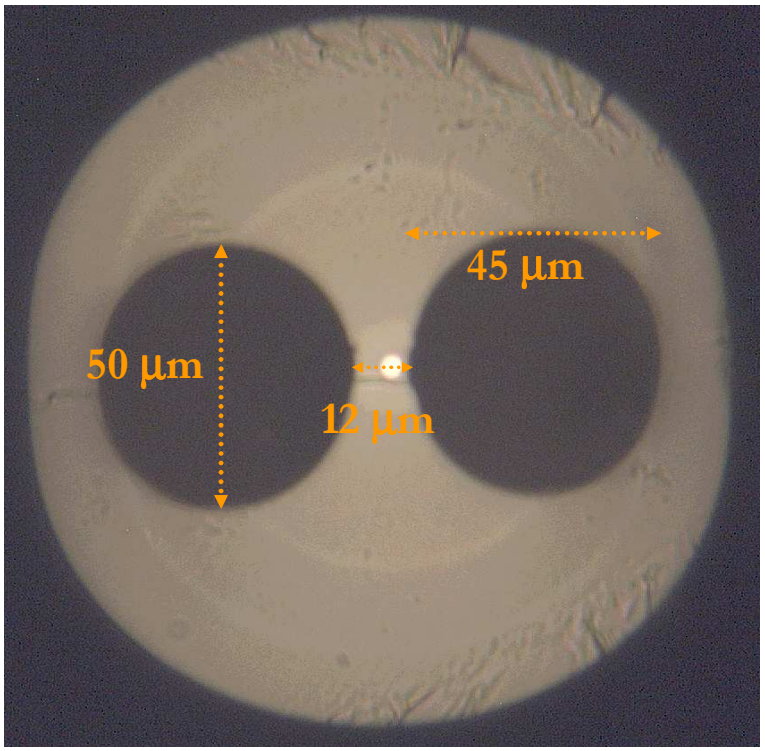


FIGURE 3.15: Cleaved cross-section of the twin-hole fibre.

The $SH$ bidimensional map in Figure 3.16 reveals an off-center wedge-shaped depletion region which points towards the cathode, extending even further up between the electrode. Similar features were reported by Myren et al. (2004) in their attempt to reveal the recorded electric field in a twin-hole fibre thermally poled with Au-Sn alloy electrodes. The microscope inspection of the cleaved end-face is displayed at the bottom right in Figure 3.16 for a comparable geometry device after $HF$ etching it.

The second harmonic signal distribution detected in reflection presents a clear evidence of a peak locally overlapping the core area. However, the greatest intensity in the $2D$ map of Figure 3.16 is equivalent to a two order of magnitude higher value than the signal in the faint gray area, which is unpredicted. In order to investigate the origin of this unexpected result, further experiments are carried out. As the nonlinear profile is typically expected below the anodic surface, poling with the anodic electrode inserted in the hole further from the core is performed to clarify whether the enhanced signal can be associated with the core. The same experimental condition as above are thus set up, but with a reversed voltage (Mezzapesa et al., 2004). This time, a much fainter peak close to the anodic surface is revealed after poling, as expected. In Figure 3.17 the left hand side signal of $\approx 0.3\,pm/V$ corresponds to genuine $SH$ generated at the anode.

The profile shown by *yellow down − triangles* discloses an even stronger signal centered on the core, so to saturate the detection. It is proposed that such an abnormal $SH$ reflection might be generated along the fibre core and reinforced after back-reflecting at the remote fibre-air interface. The reflection at the air-glass interface is estimated

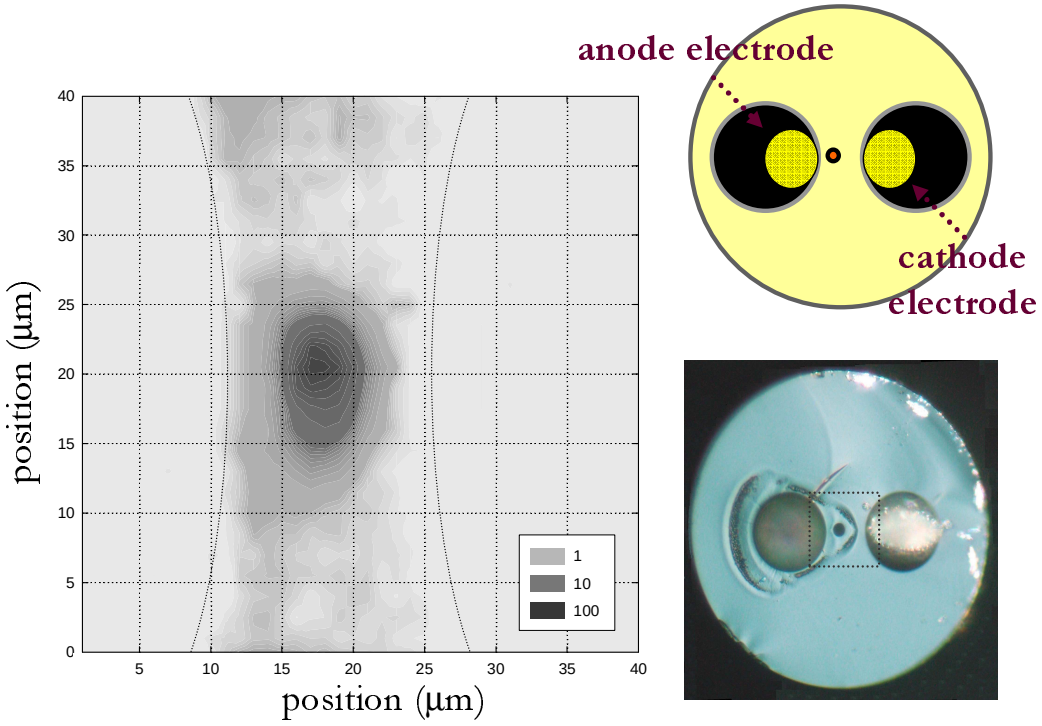


FIGURE 3.16: Spatial bi-dimensional map of the $SHG$ signal from the cleaved end-face of a thermally poled twin-fibre. The reflected $SH$ is obviously zero when the beam is scanned across the holes. At the bottom right, the microscope image of the cleaved end-face is displayed as reported by Myren et al. (2004) on poled twin-hole fibre after $HF$ etching.

as $\cong 4\%$, thus typically neglected in bulk. In fibres and waveguides, however, the $SH$ signal might significantly grow owing to modal-phase matching during the optical field propagation. To prove this, index matching gels have been investigated to reduce the back scattered signal. The far end of the fibre is immersed in the gel in order to minimize the index discontinuity at the interface. The best index matching gel which generates the lowest back reflected light is $n(@1064\,nm) = 1.46750$. The large signal around the core is now greatly reduced, as profiled in *green squares*, whereas the small peak next to the anode results unaffected by it, thus confirming that the latter is genuinely due to poling-induced nonlinearity. Its maximum value, as determined by referring it to the calibration z-cut quartz of known nonlinear coefficient (Section 3.4.3), is comparable with thermally poled bulk silica. Also shown in Figure 3.17 are both the nonlinearity profile with inverted pump polarization (*blue up − triangles*) and the *brown circles* reflected $IR$, whose intensity is obviously null when the beam is scanned across the holes. Finally, extra care is taken to verify that same features would not actually be revealed nor when a virgin devices is likewise scanned before being poled, neither when the scan is performed out of the poled core region.

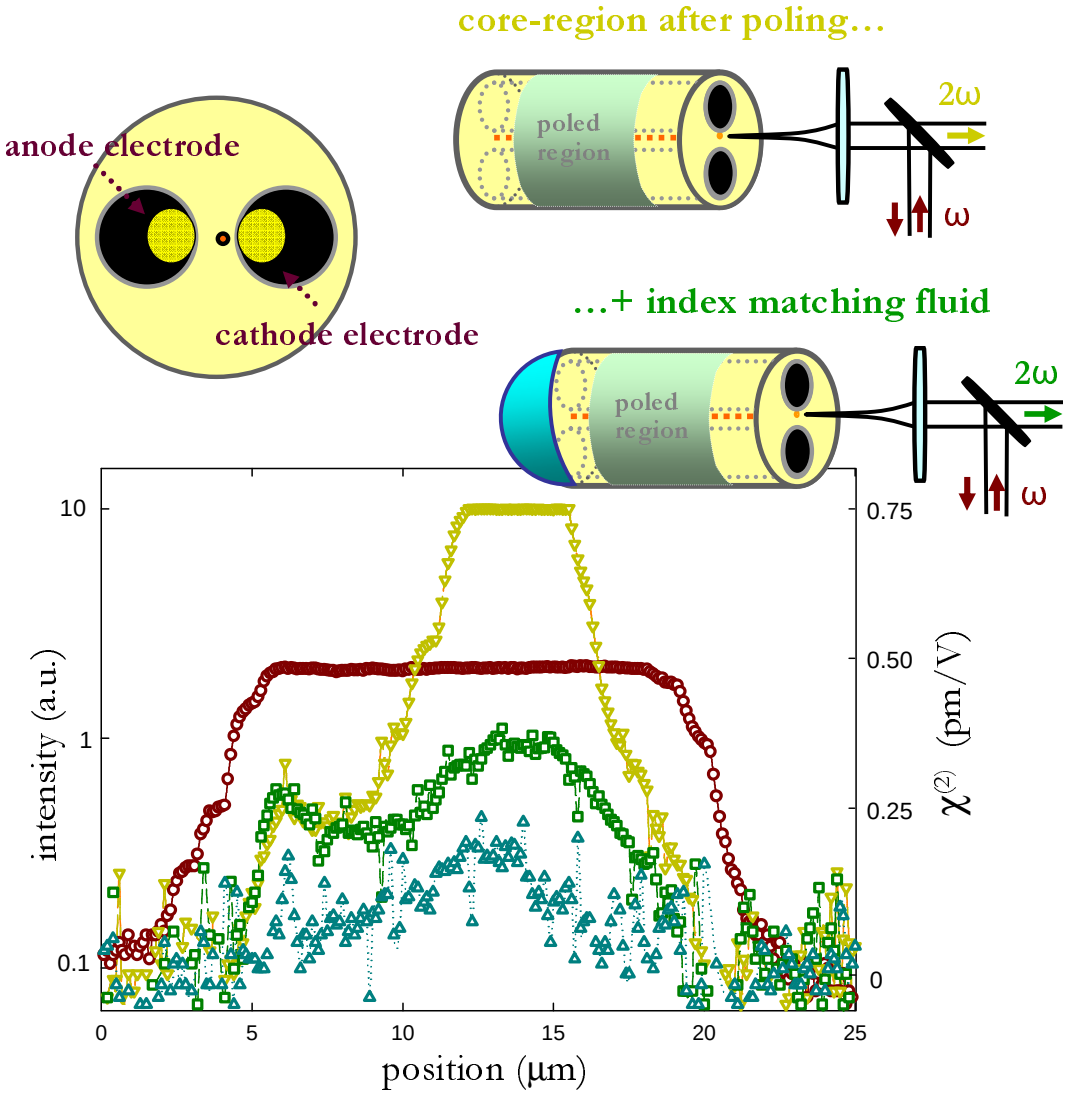


FIGURE 3.17: *IR* reflected pump (*brown circles*) and *SH* intensity profile versus vertical translation in a twin-hole fibre poled at $280°C$, $3.2\,kV$ for $1\,min$ before (*yellow down − triangles*) and after (*green squares*) the index matching gel. *SHG* intensity profile changes with inverted pump polarization (*blue up − triangles*).

For the sake of comprehensiveness, the spatial $2D$ map of the poling-induced $\chi^{(2)}$ distribution is plotted in Figure 3.18. On the left hand side, the fundamental reflected signal features the position of the holes and allows a better location of the core, highlighted by a dotted circle.

The reflected signal generation in second harmonic is shown on the right hand side of Figure 3.18, and clearly reveals the distribution of the depletion region by the anode side, whose wedge-tailed shape features some similarities with Figure 3.16. However, the contribution coming from back-reflected signal around the core is not totally erased, although the remote tip of the fibre is constantly immersed in index matching gel.

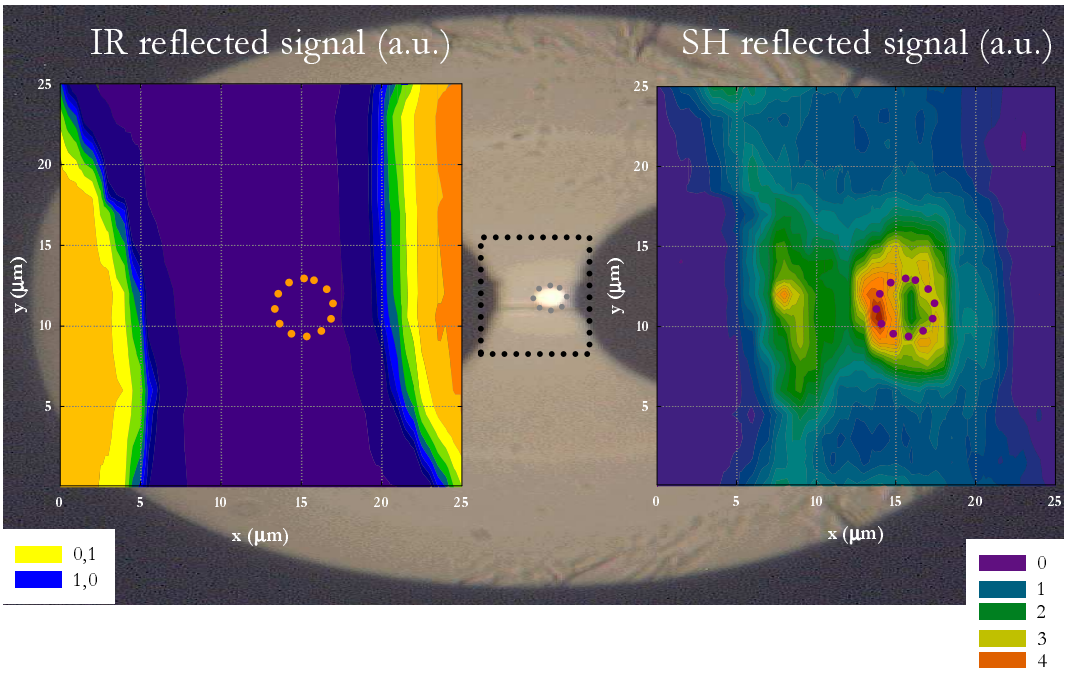


FIGURE 3.18: $2D$ distribution of both $IR$ at the $left\,hand\,side$ and $SH$ reflected signal ($right\,hand\,side$) from the cleaved end-face of a twin-hole fibre poled for $1\,min$ at $280^oC$ with $3.2\,kV$ applied away from the core

In conclusion, modifications of poling induced $SH$ signal are revealed on poled devices by scanning optical microscopy. Non-invasive investigation of both nonlinear thickness and coefficient leads to spatially mapping the nonlinearity distribution in thermally poled twin-hole fibres with a spatial resolution $\approx 1\,\mu m$. The direct inspection of waveguiding region results yet altered by spurious $SH$ signal detection in reflection. Any source of signal contamination must be filtered out before the measurement, most of all in experiments where the confinement of the spatial modulation of $\chi^{(2)}$ along the waveguide and the two (fundamental and second order) modes is to be optimized.

## 3.5 Conclusion

This chapter describes the methods employed to profile $\chi^{(2)}$.

The Maker Fringe Technique was the first method used for measurements of $\chi^{(2)}$, but its main drawback for the characterization of poled glasses is the determination of the nonlinear depth. It is not suitable when the depth of the nonlinear region is smaller than one coherence length, unless the thickness of the nonlinear region is measured independently by etching.

Section 3.3 describes the layer peeling method. The power of the second harmonic wave generated within the poled sample is recorded in a very reproducible way as the nonlinear layer is simultaneously etched in hydrofluoric acid. The layer peeling method

is integrated with interferometric measurement of the etching rate, the nonlinear depth is measured in real time and the built-in electric field distribution can be deduced. Hence, the nonlinear profile can be reconstructed by layer peeling algorithm, with a spatial resolution of below $1\,\mu m$. In contrast to the Maker Fringe technique, which gives only general features of the nonlinear profile, the layer peeling method allows a direct determination of it without any assumption on the microscopic mechanisms at the origin of the nonlinearities and data post-treatment. Furthermore, although destructive, this method is highly sensitive to sign changes of $\chi^{(2)}$ as well.

Finally, the *SHSOM* has proved to be well suitable to detect modifications of the $SH$ signal in a non-invasive way within $\approx 1\,\mu m$ spatial resolution. Direct investigation of both nonlinear thickness and coefficient in thermally poled twin-hole fibre have been reported. However, precautions have to be taken when accurate location of the $\chi^{(2)}$ distribution in thin nonlinear guiding films is under characterization.

In the light of these conclusions, the layer peeling technique is considered at this stage as the best-suited characterization approach among those available. During this project, this detection system has greatly contributed to identifying the critical parameters affecting the poling process in $Bi_2O_3$-based glasses and enhancing their induced $\chi^{(2)}$, as detailed in Section 5.3.1.1.

# Chapter 4

# Poling of high-index glasses

## 4.1 Why bismuthate glass?

The growing commercial interest toward engineering all-optical communication devices has recently converged on 'low-melting point' host media, whose refined matrix combines large nonlinear coefficient along with good optical quality and low optical losses. The current fabrication technologies for their glass synthesis relies on heavy metal ions, mainly lead. In particular, because the chemical bond between lead and oxygen is weak and easily dissociates at a low temperature, the lead largely decreases the melting temperature, without decreasing the chemical durability of glass. Heavy metal ions are conveniently added to the compounds also to control the absorption window and increase the refractive index, in turn largely dependent on the material density.

Chalcogenide glasses are potentially good candidates for optical component achievements, such as waveguiding devices. Their spectral range of transparency extends in the infrared region ($10-20\,\mu m$) and they display high linear and nonlinear indices (Smektala et al., 1998). Moreover, nonlinear optical phenomena such as second-harmonic generation or electro-optic modulation are also allowed owing to the creation of a permanent electrical polarization inside the glass by thermal poling (Guignard et al., 2005). Guignard et al. (2006) claimed a record value of $\chi^{(2)} \cong 8\,pm/V$ in a sulfide glass system. However, reversible erasure of poling-induced second-order optical nonlinearities was observed when these glasses were light-exposed in the visible range. $As_2S_3$ thin films were also shown photosensitive at wavelengths in the telecommunication window (Ho et al., 2003) due to photoinduced change in polarizability of Van der Waals type hyperpolarizable bonds, which may in turn affect the glass stability/fragility. Finally, health and environmental issues have to be carefully considered when working with poisonous elements, such as $As$, $Pb$, $Se$, $Te$.

In 2005, Dussauze et al. (2005) indicated the high-index sodium borophosphate niobium oxide glasses as a well-suited alternative for electro-optical applications. A reproducible

second-order susceptibility value of $\cong 5\,pm/V$ was reported, although the nonlinear layer showed a rather complex space-charge migration process.

Recently, bismuthate glasses have also experienced intense research interest among highly nonlinear optical-guiding media owing to nonlinear refractive index up to two order of magnitude higher than silica-based glasses. Their good mechanical, chemical and thermal stability allowed preform fabrication for low-loss fiber drawing (Ebendorff-Heidepriem et al., 2005). $Bi_2O_3$-based erbium doped fibres have already been demonstrated (Ohara et al., 2003).

In this chapter, an experimental study of poling induced nonlinearity in high-index bismuth-based samples is described. In particular, an efficient poling treatment is demonstrated on bismuth-borate glass systems ($Bi_2O_3$-$ZnO$-$B_2O_3$), whose nonlinear $\chi^{(3)}$ susceptibility is found to increase with the $Bi_2O_3$ content (Section 4.1.2). The $Bi_2O_3$-$B_2O_3$-$SiO_2$ glass family with high concentration of $Bi_2O_3$ ($92\,wt\%$) exhibited $\chi^{(3)}$ values as large as $6\times10^{-14}cm^2/W$, which is two orders of magnitude higher than silica (Sugimoto et al., 1999). Since the second-order optical nonlinearity in thermally poled glasses is predicted to be enhanced in proportion to the intrinsic third-order optical nonlinearity, for a given frozen-in electric field strength (Equation 2.9), bismuth-borate $Bi_2O_3$-$ZnO$-$B_2O_3$ glasses are hence chosen to be investigated.

### 4.1.1 Chemical composition

Bismuth-borate samples ($BZH\diamond$) were fabricated at the Nippon Glass Sheet ($NSG$) facilities by melting and quenching in the ternary system $Bi_2O_3 - ZnO - B_2O_3$ and in the binary system $ZnO - B_2O_3$, respectively. The nominal compositions and glass transition temperatures ($T_g$) of the $BZH\diamond$ glasses used for poling are listed in Table 4.1.

| *sample* | $Bi_2O_3$ $(mol\%)$ | $ZnO(mol\%)$ | $B_2O_3(mol\%)$ | $T_g(^oC)$ |
|---|---|---|---|---|
| $BZH6$ | – | 55.0 | 45.0 | 550 |
| $BZH4$ | 6.25 | 46.88 | 46.88 | 495 |
| $BZH7$ | 12.5 | 43.75 | 43.75 | 470 |
| $BZH2$ | 25.0 | 37.5 | 37.5 | 419 |

TABLE 4.1: Nominal compositions and glass transition temperatures ($T_g$) of various $BZH\diamond$ glasses with different bismuth oxide content.

Boron and zinc ions act as network formers and modifiers, respectively. The bismuth oxide is varied from 6.25 $mol\%$ to 25.0 $mol\%$ while keeping constant the ratio

$$\xi = \frac{[ZnO]mol\%}{[ZnO]mol\% + [B_2O_3]mol\%} \tag{4.1}$$

In the bismuth-free borate glass, the ratio $\xi$ is equal to 0.55, whereas its value is set equal to 0.5 in all the other cases. There, bismuth ions can act both as network modifiers and network formers according to $Bi_2O_3$ content, although only as network modifiers at very low concentration of bismuth oxide (Chowdari and Rong, 1996).

The glass transition temperature ($T_g$) decreases with the $Bi_2O_3$ content, as reported by the manufacturers. Hence, $BZH\diamond$ glasses are expected to be much softer than silica ($T_g \approx 1700^oC$) at typical poling temperatures ranging between $250-350^oC$ and, consequently, their response to the thermal treatment may considerably differ.

In addition to the nominal composition, water is present in the glass matrix in the form of hydroxyl $OH$ bonds. In Table 4.2, the weight percentage of $OH$ impurity ($\omega_{OH}$) is calculated from measurements of the absorption peak around 2.9 $\mu m$, as highlighted in the inset of Figure 4.1. The $OH$ content ranges from 463 $ppm$ in 1.0 $mm$ thick $BZH2$ samples to 808 $ppm$ in 1.0 $mm$ thick $BZH4$ samples (Table 4.2) and, interestingly, varies with the sample thickness (not shown in Figure 4.1). It is found to be 1.5 times lower in 0.9 $mm$ than in 1.0 $mm$ thick $BZH6$ samples and two times lower in 0.2 $mm$ than in 1.0 $mm$ thick $BZH2$ samples.

| *sample* | $Bi_2O_3$ $(wt\%)$ | $\rho(g/cm^3)$ | $\omega_{OH}(wt\%)$ | $n$ | $\Phi$ |
|---|---|---|---|---|---|
| $BZH6$ | – | $\approx 3.0$ | 0.0624 | 1.62 | 4.7 |
| $BZH4$ | 29.15 | $\approx 4.0$ | 0.0808 | 1.71 | 9.3 |
| $BZH7$ | 46.85 | $\approx 5.0$ | 0.0531 | 1.79 | 16 |
| $BZH2$ | 67.29 | 6.1 | 0.0463 | 1.91 | 33.3 |

TABLE 4.2: Weight percentage of hydroxyl ($OH$) ions and refractive index ($n$) of $BZH\diamond$ samples. $\rho$: glass density. $OH$ weight percentage ($\omega_{OH}$) is calculated by: $\omega_{OH}(\%) = 0.1 \times \alpha_{OH}/\epsilon_{OH} \times M_{OH}/\rho$, where $\alpha_{OH}$ is the $OH$ absorbance peak (measured around 2.9 $\mu m$), $\epsilon_{OH}$ is the $OH$ extinction coefficient (50 $l/mol/cm$) and $M_{OH}$ is the $OH$ molar weight. Values of $\omega_{OH}$ are given for batches of 1.0 $mm$ thick samples. The refractive index is estimated from Fresnel reflection loss measurements. The enhancement factor $\Phi$ is calculated from Equation 1.5: $\Phi = [(n^2-1)/(n_s^2-1)]^4$ where $n_s = 1.45$ is the refractive index of silica.

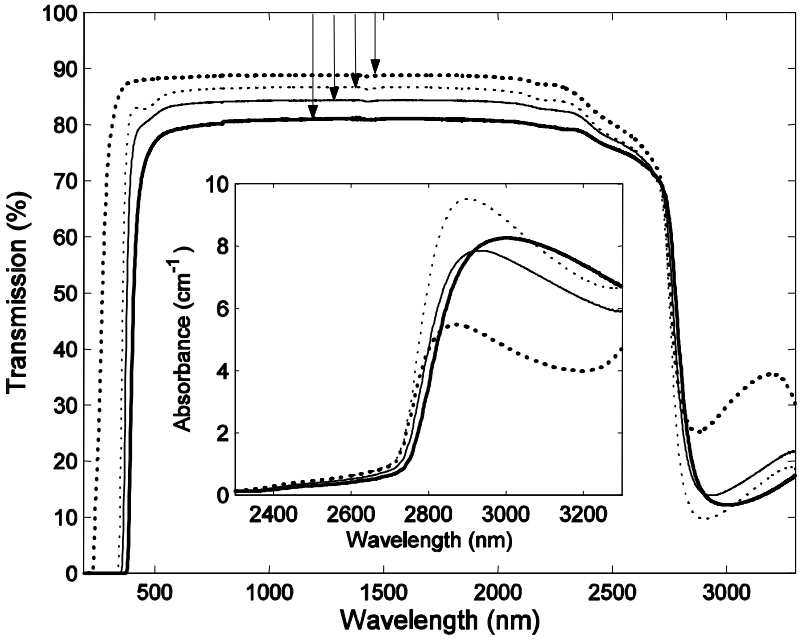


FIGURE 4.1: Optical transmission spectra measured in $1.0\,mm$ thick $BZH6$ (thick dotted line), $BZH4$ (thin dotted line), $BZH7$ (thin line) and $BZH2$ (thick line) samples. Vertical arrows indicate the transmission loss associated with Fresnel reflections at air/sample interfaces ($T_0$). Inset: absorbance spectra - the absorbance is calculated by $\alpha = [log(1/T) - log(1/T_0)]/L$, where $T$ is the measured transmission loss. Samples have thickness, $L$, of $1.0\,mm$, $0.5\,mm$ or $0.2\,mm$ and size of $20 \times 30\,mm^2$.

The optical transmission spectra in Figure 4.1 exhibit a flat maximum between $\approx 600\,nm$ and $\approx 2000\,nm$ and an $UV$ absorption edge which shifts toward the red with increasing $Bi_2O_3$ content. Assuming that the transmission loss in the flat region of the spectrum, $T_0$, is only due to Fresnel reflections at air-sample interfaces, i.e. $T_0 = (1-R)^2$, the refractive index listed in Table 4.2 for all different compositions were estimated by

$$n = \frac{\sqrt{R}+1}{1-\sqrt{R}} \tag{4.2}$$

with $R$ being the power reflection coefficient.

Also listed in Table 4.2 is the predicted enhancement factor, $\Phi$, introduced in Section 1.1.3, which clearly scales with the bismuth content. Only few $mol\%$ of $Bi_2O_3$ imply an intrinsic third-order susceptibility several times higher than silica, clarifying scientific and technological interest in $Bi_2O_3ZnOB_2O_3$ glass compounds.

### 4.1.2 $\chi^{(3)}$ measurement on bismuth-based glass

In the last section, the third order susceptibility, $\chi^{(3)}$, was predicted to scale with the bismuth oxide concentration in bismuth-borate glass family. Likewise, the refractive index dispersion ($\partial n/\partial\lambda$) is expected to increase with increasing $Bi_2O_3$ content, as

Becker (2003) reported in binary $Bi_2O_3 - B_2O_3$ glasses using the Sellmeier equation. By adapting Becker (2003) glass dispersion data for $Bi_2O_3ZnOB_2O_3$ samples, the refractive index values at $\lambda = 1064\,nm$ and $\lambda/2 = 532\,nm$ are calculated as a function of $Bi_2O_3$ content, and collected in Table 4.3. The coherence length of the second-order nonlinear optical interaction is shown to be even shorter than in silica, depending upon the $Bi_2O_3$ content. However, the refractive index values as calculated from Sellmeier coefficients are slightly undervalued compared to those determined by Fresnel reflection measurements on $BZH\diamond$ glasses (see Table 4.2), most likely owing to the zinc oxide contents in $BZH\diamond$ glass compounds.

| *sample* | $Bi_2O_3$ $(mol\%)$ | $n_\omega$ | $n_{2\omega}$ | $l_c(\mu m)$ |
|---|---|---|---|---|
| $BZH6$ | – | 1.5500 | 1.5600 | 26.6 |
| $BZH4$ | 6.25 | 1.5600 | 1.5800 | 13.3 |
| $BZH7$ | 12.5 | 1.6580 | 1.6860 | 9.5 |
| $BZH2$ | 25.0 | 1.8106 | 1.8536 | 6.2 |

TABLE 4.3: Extrapolated value of refractive indexes and coherence length ($l_c$) of $BZH\diamond$ samples. $n_\omega$, $n_{2\omega}$: refractive index values at $\lambda = 1064nm$ and $\lambda/2 = 532nm$. The *SHG* coherence length is given by $l_c = \lambda/(4(n_{2\omega} - n_\omega))$. Values of $n_\omega$ and $n_{2\omega}$ are quoted for comparison and calculated using Sellmeier coefficients available for $Bi_2O_3 - B_2O_3$ glasses (*Becker* (2003)).

Direct investigations on the third order nonlinearity of $Bi_2O_3ZnOB_2O_3$ glasses are carried out thanks to the collaboration with the research group of Prof. Gomes at the Universidade Federal de Pernambuco, Brazil. In particular, they have fully characterized the optical properties of the most promising $BHZ2$ and $BZH7$ glass compounds (Gomes et al., 2007). A summary of results is provided in the next section, along with a schematic description of the two complementary techniques employed for this purpose: the one color Z-scan method and the Kerr shutter technique, respectively. In detail, the sign and magnitude of the real (nonlinear refractive index $n_2$) and imaginary part (nonlinear absorption $\alpha_2$) of the third order nonlinearity are evaluated with the Z-scan method, whereas with the Kerr gate the magnitude of the nonlinearity as well as the electronic time response are measured. A standard carbon disulfide $CS_2$ is used as reference to calibrate the measurements in both Z-scan and Kerr-shutter experiments, since its $n_2$ coefficient is well reported in literature (Stegeman, 1997) for the visible-$NIR$ range: $n_2(@532\,nm) = 3.1 \times 10^{-14} cm^2/W$ and $n_2(@1064\,nm) = 3.3 \times 10^{-14} cm^2/W$.

#### 4.1.2.1 Z-scan method

The well-established Z-scan technique is employed for direct measurements of the nonlinear properties of $Bi_2O_3ZnOB_2O_3$ compounds. In this method the change in phase of a laser beam induced by propagation through a nonlinear material, gives rise to a wave front distortion of the beam. The Z-scan experiment gives both the sign and magnitude of this phase change, which is in turn related to the change in index of refraction (Sheik-Bahae et al., 1990). Moreover, it can separately determine changes in the nonlinear absorption coefficient by inspecting optical transmission spectra.

The measurements are performed using both fundamental and second harmonic ($532\,nm$) light beam generated by doubling a Q-switched and mode locked $Nd$:$YAG$ laser, delivering pulses of $100\,ps$ and $80\,ps$ full width at half maximum, respectively. To avoid cumulative thermal effects, a single pulse at a repetition rate of $10\,Hz$ is selected using a pulse picker. A lens of $10\,cm$ focal distance focuses the laser beam of measured beam waist of $20\,\mu m$, on the surface of the sample, which is in turn mounted on a computer-controlled translation stage.

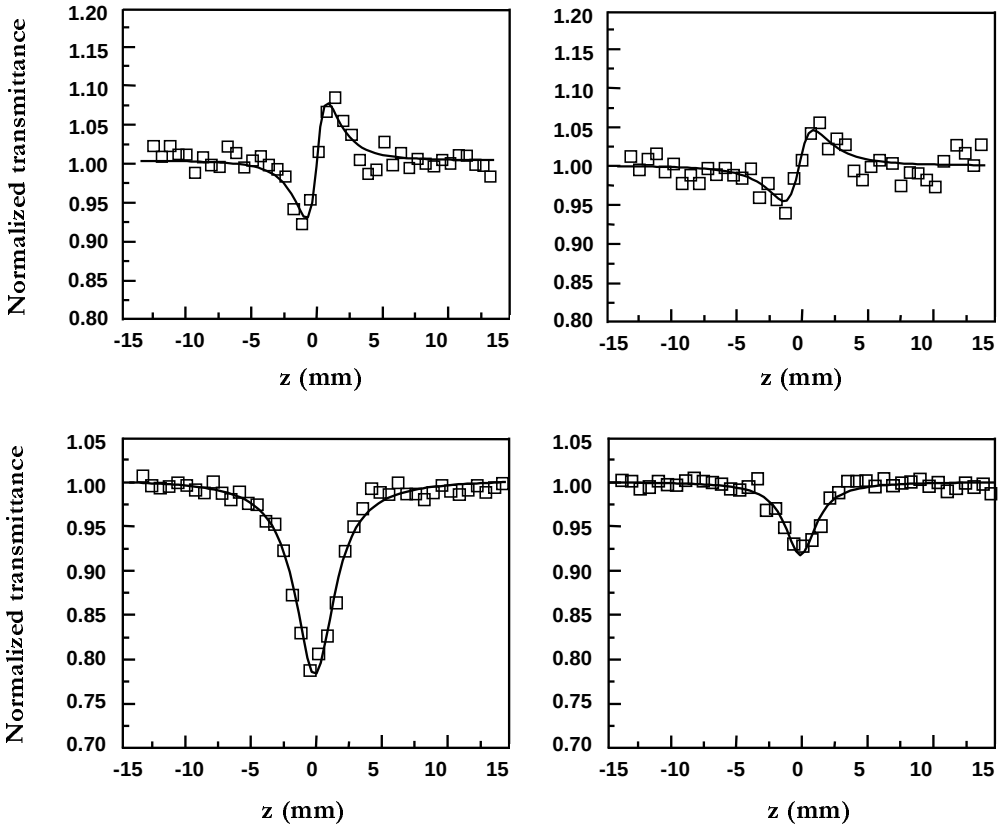


FIGURE 4.2: Normalized Z-scan profile at $532\,nm$ for $BZH2$ (left) and $BZH7$ (right) samples. The measured nonlinear refraction (top) and the measured nonlinear absorption (bottom), respectively, are taken at the same beam intensity $I = 1.3\,GW/cm^2$.

A photodetector equipped with an adjustable aperture is placed in the far-field region. The detector output is monitored as the position of the sample, $z$, is translated along the optical axis relative to the focal plane of the input lens ($z = 0$ in Figure 4.2). A small aperture Z-scan experiment is employed for $n_2$ measurements, and a wide or absent aperture is necessary for the determination of $\alpha_2$.

Figure 4.2 shows the results obtained by testing $1\,mm$ thick $BZH2$ and $BZH7$ samples for identical beam intensity at $\lambda = 532\,nm$. The $z$ ordinate is measured along the beam propagation direction and $z < 0$ corresponds to locations of the sample between the focusing lens and its focal plane. Using the equations given by Sheik-Bahae et al. (1990), the magnitude of the nonlinearity is found to be $n_2(BHZ2) = 3.0 \times 10^{-14} cm^2/W$ and $n_2(BHZ7) = 1.8 \times 10^{-14} cm^2/W$, respectively. The sign of the nonlinearity is positive in both cases as measured on $CS_2$, not shown in Figure 4.2.

The measured $n_2$ coefficients at $\lambda = 1064\,nm$ are compared with silica values available in literature for identical spectral and temporal excitation conditions (DeSalvo et al., 1996). In particular, an enhancement factor of the real part of the third-order optical nonlinearity as large as $n_2(BZH2) \cong 31 \times n_2(SiO_2)$ is inferred, which corroborates the assertions made in Table 4.2, where the third-order nonlinear optical susceptibility in $BZH2$ is estimated to be 33.3 times higher than $SiO_2$, according to Miller's rule.

The measured values of the absorptive nonlinearities at $\lambda = 532\,nm$ are $\alpha_2(BHZ2) = 5.5\,cm/GW$ and $\alpha_2(BHZ7) = 1.5\,cm/GW$, respectively. No nonlinear absorption coefficient can be measured when using $1064\,nm$ excitation wavelength, which is in good agreement with the fact that the glass linear absorption spectra in Figure 4.1 display a strong absorption below $400\,nm$, thus being susceptible to nonlinear (two photon) absorption below an excitation wavelength of $800\,nm$. Nonlinear absorption is typically exploited for optical limiting application, as well-reported by Oliveira et al. (2006) on the same $Bi_2O_3ZnOB_2O_3$ glass compounds.

#### 4.1.2.2 Kerr shutter technique

In order to determine the time response of the nonlinearity, Kerr-shutter measurements in the femtosecond regime are performed by the research group of Prof. Gomes at the Universidade Federal de Pernambuco, Brazil. In detail, a beam delivering pulses with $150 fs$ duration at $76 MHz$ repetition rate from a Ti-sapphire laser is split into two beams with different intensities. The electric field of the strong (*pump*) beam is set at $45^o$ with respect to the electric field of the weak (*probe*) input beam. When the pulses of the two beams overlap spatially and temporally at the sample position, the probe beam polarization rotates due to the birefringence induced in the sample by the pump beam. Then, a fraction of the probe beam passes through a polarizer which is orthogonal to

the input probe beam polarization. A detector is used to record the probe signal as a function of the time delay between the pump and the probe beams.

Using the value of $n_2^{Kerr}(CS_2) = 2.3 \times 10^{-14} cm^2/W$ reported by Alfano (1984) at $\lambda = 800\,nm$, the magnitude of the nonlinearity in $BZH\diamond$ samples was estimated to be $n_2^{Kerr}(BZH2) = 2.73 \times 10^{-14} cm^2/W$ and $n_2^{Kerr}(BZH7) = 0.52 \times 10^{-14} cm^2/W$, in excellent agreement with the results obtained with the Z-scan technique in Section 4.1.2.1.

Furthermore, Figure 4.3 shows the temporal measurements obtained with the Kerr shutter for $BZH2$ (*triangles*) and $BZH7$ (*square*), respectively. It results that the glass response time is symmetrical for both $BZH2$ and $BZH7$ samples and only limited by the pump pulse duration. This implies that the rise-time of the nonlinearity at this wavelength is faster than $200 fs$.

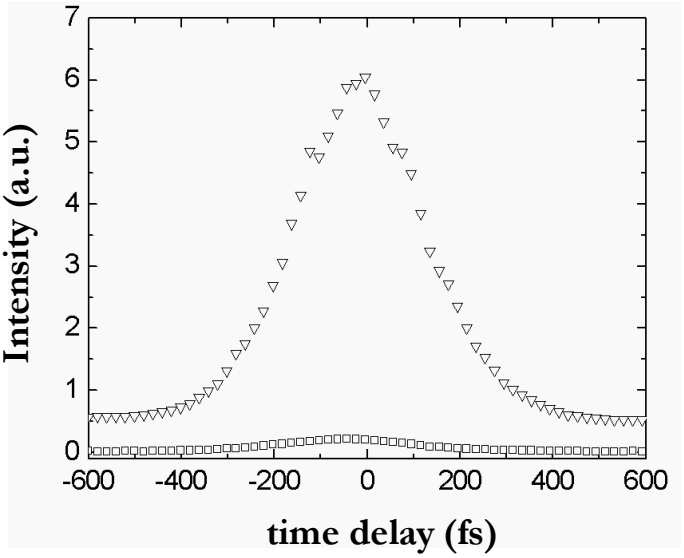


FIGURE 4.3: Optical Kerr shutter measurements in glasses $BZH2$ (*triangles*) and $BZH7$ (*square*). For identical pump intensity the relative signal intensities are compared.

In summary, the nonlinear optical coefficients of the newly devised $BZH2$ and $BZH7$ compounds have been fully characterized. Their patented composition has been intentionally engineered to increase the glass linear refractive index, hence the third order optical nonlinearity. The results obtained using the Z-scan and Kerr-shutter techniques show that these glasses are up to 31 times better than silica in terms of third-order susceptibility, which leads to the expectation of a similar enhancement in $\chi^{(2)}$ after poling, according to the strategy introduced in Section 1.1.3.

## 4.2 Thermal poling experiments

In Section 2.3.1, second-order optical nonlinearities induced by thermal poling technique are shown to be originated from the rectification of the intrinsic third-order nonlinear optical susceptibility by the frozen-in electrostatic field. The rectification model predicts an enhancement of $\chi^{(2)}$ in proportion to $\chi^{(3)}$ in thermally poled glasses with higher third-order optical nonlinearity than silica, provided that a frozen-in field strength as high as in silica can be achieved. In Section 4.1.2, $Bi_2O_3$-based glasses are shown to be promising for this purpose since they exhibit intrinsically higher $n_2$ coefficients than silica.

In what follows, the first experimental evidence of second-order optical susceptibility are reported on thermally poled $Bi_2O_3ZnOB_2O_3$ glasses with various $Bi_2O_3$ content. The induced nonlinearity is created in a near-surface layer at the anode side, with $\chi^{(2)}$ values increasing from about $0.2\,pm/V$ to $0.6\,pm/V$ as the $Bi_2O_3$ content scales from $6.25\,mol\%$ to $25.0\,mol\%$.

### 4.2.1 Sample poling procedure

Thermal poling of the $BZH\diamond$ glass family is carried out with the electrodes press-contacted on the sample, which is in turn heated in a temperature controlled oven ($\pm 0.1°C$). A standard procedure is initially adopted, consisting in heating the sample slowly up to a prescribed temperature $T_p$, applying the voltage, $V_p$, for a certain time $t_p$, cooling the sample slowly down to $50^oC$ with the voltage still applied, and finally removing the voltage. This avoids breaking the sample due to thermal stresses. A schematic diagram of the apparatus for the poling in air is shown in Figure 4.4, with a detailed photograph of the poling configuration.

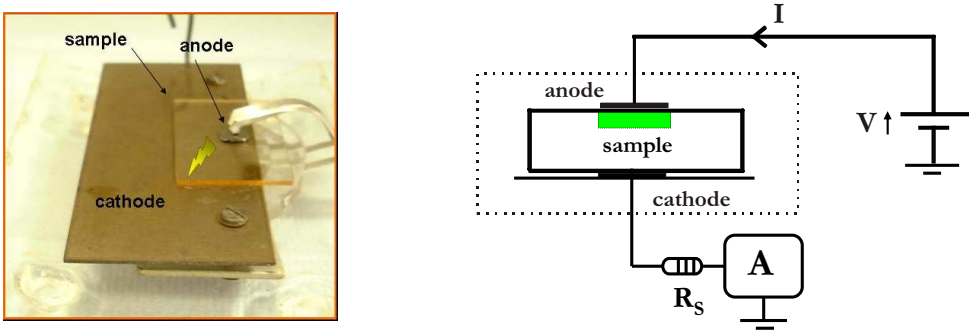


FIGURE 4.4: Experimental set-up for thermal poling in air.

An ammeter ($A$), in series with a protection resistance ($R_S = 100\,k\Omega$), is used to measure the current $I$ which flows through the sample during poling. The high-voltage ($HV$) source delivers a constant voltage, provided that the current is lower than a pre-set limit ($I_{LIM}$). Sample and electrode dimensions have to be designed to prevent electrical breakdown in air, which is estimated as $\approx 1\,kV/mm$ at $300^oC$ and would be caused

by the existence of a high potential on the sample surface. For a set poling voltage of $V_p = 4kV$, as typical in silica, an electrical current as high as tens of microamperes is measured during poling (see Section 4.2.4). However, current paths in air may cause the current flowing through the sample to be effectively lower than the current detected by the external circuit in Figure 4.4. Dielectric breakdown of the glass may occur during the treatment, if both poling temperature and time are not carefully chosen.

### 4.2.2 Investigating the formation of nonlinearity: glass-electrode contact

A preliminary study is conducted to assess the role played by glass-electrode contact on the generation of second-order nonlinearity in bismuth-based high index glasses. Systematic experiments are carried out at $400^oC$ and $4kV$ on $1\,mm$ thick $BZH7$ samples using different types of electrodes. The roughness ($r$) of the surface, which determines the quality of the contact, is listed in Table 4.4 for a few commonly used electrode materials: $r$-values are measured using an alpha-step profilemeter.

| **electrode material** | $r$ $(nm)$ |
|---|---|
| silicon | $\leq 10$ |
| gold-on-silicon | $\leq 50$ |
| stainless steel | $\leq 100$ |
| platinum | 1000 |

TABLE 4.4: Surface roughness $r$ of candidate electrodes for poling.

In order to probe the poled samples as a function of the electrode roughness, the nonlinear characterization is carried out by employing the Maker Fringe technique. The $SH$ power is measured at an incident angle of $60^o$ and the uniformity of the $SHG$ signal is measured by scanning the fundamental $IR$ beam across the poled area (Section 3.2).

Nonlinearity can be induced in 12.5% $Bi_2O_3$ glass by poling it for 30 minutes at $70^oC$ below the glass transition temperature. Moreover, the lower the roughness of the electrode surface, the higher and the more uniformly distributed the $SH$ signal generated from the poled region. In contrast to silica, chemical reactions at the sample-electrode interface are shown to affect the poling process. Oxidation reactions take place at the interface between the sample and the anode when a stainless steel anode is employed. With platinum foil electrodes, the $SHG$ power is measured to be two order of magnitude weaker

and much less uniform across the poled area than with $Si$ electrodes. Although platinum is difficult to oxidize, the attraction of cations $H^+$ from surrounding atmosphere is more likely to occur, due to its surface roughness. Such $H^+$ ions may penetrate into the sample and substitute $H^+$ ions which just left the anode, slowing down the formation of the depletion region and influencing the space charge dynamics (see Section 4.2.5). After poling, $Si$ electrodes adhere to the anodic surface by electrostatic forces and chemical bonding: occasionally they can be removed by dropping isopropanol on the sample. Field-assisted metal-to-glass sealing or anodic bonding (Wallis and Pomerantz, 1969) is related to the depletion of ions near the glass surface, which would make it highly reactive with the silicon surface, so to chemically bind it to the glass surface (B.Kusz, 2003). Anodic bonding during poling is avoided when gold-on-silicon pressed-on electrodes are used. Evaporating gold electrodes directly onto the material may also give advantages, as described in Section 4.2.4.1, although the sample surface is irreversibly damaged by the chemical etchant used to remove the electrode after poling.

It is concluded that the formation of second-order optical nonlinearity across the poled area of $Bi_2O_3$-based glasses requires intimate contact between the electrode and the glass surface, along with optimization of all poling parameters. In order to obtain uniform and efficient $SHG$ power, gold-on-silicon pressed-on electrodes have to be used.

#### 4.2.2.1 The effect of poling parameters upon the $SHG$ power

Second-order nonlinearity as high as in poled silica is measured in high-index $BZH\diamond$ glasses by poling at temperature close to their glass transition value, $T_g$ (Deparis et al., 2005b). Figure 4.5 shows $SHG$ power observed as a function of the poling temperature, $T_p$. The $SH$ generated signal is normalized to the reference Herasil1 plate, poled at $280^oC$ and $4\,kV$ for $30min$.

Second-order nonlinearities are observed only if poling is carried out at temperature a few tens of degrees below the glass transition point. With the poling voltage $V_p = 4\,kV$, the efficiency of the $SH$ generation is measured to improve with the poling temperature. The optimal poling temperature shown in Figure 4.5 scales inversely with the $Bi_2O_3$ content, as $T_g$ does accordingly with the glass composition (Table 4.1).

The highest values of $SHG$ are obtained by poling in the temperature range from $0.8\times T_g$ to $0.9\times T_g$. In particular, the highest values of $SHG$ in bismuth-free $ZnOB_2O_3$ glass are obtained at $500^oC$. For $BZH4$ glass, the highest values of $SHG$ are obtained in $1.0\,mm$ thick samples poled at $420^oC$ $(0.90 \times T_g)$, whereas the highest $SHG$ values for $25.0\,mol\%\,Bi_2O_3$-glass are obtained only in $0.2\,mm$ thick samples poled around $280^oC$ $(0.80 \times T_g)$. For $BZH7$ glass $(12.5\,mol\%\,Bi_2O_3)$, $SHG$ values as high as in silica are obtained both in $1.0\,mm$ and $0.2\,mm$ thick samples poled at $400^oC$ $(0.91\times T_g)$ and $350^oC$ $(0.84 \times T_g)$, respectively. Moreover, the $SHG$ signal measured from $BZH7$ compounds

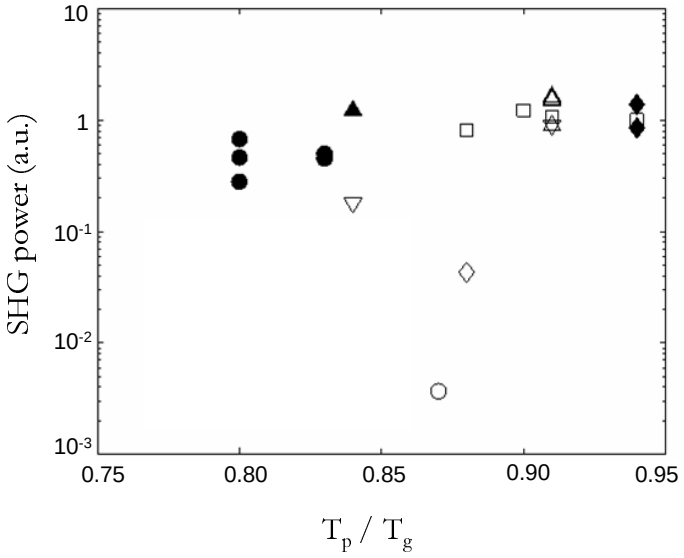


FIGURE 4.5: Normalized *SHG* power as a function of the ratio between poling and glass transition absolute temperatures ($T_p/T_g$) for $BZH6$ (*diamond*), $BZH4$ (*square*), $BZH7$ (*triangle*) and $BZH2$ (*circle*), respectively. The reference sample is a $0.5\,mm$ thick Herasil1 plate, poled at $280^oC$ and $4\,kV$ for $30\,min$. At a given poling temperature, samples are poled at $4\,kV$ for different poling times and thickness: $1.0\,mm$ ($\diamond, \square, o, \Delta$), $0.9\,mm$ ($\blacklozenge$), $0.5\,mm$ ($\nabla$), $0.2\,mm$ ($\blacktriangle, \bullet$).

displays a clear dependence on the poling time and on the sample thickness, as shown at the top and bottom in Figure 4.6, respectively.

In $1.0\,mm$ thick $BZH7$ sample (top in Figure 4.6), the *SHG* power as a function of the poling duration tails off with a flat decrease for longer time. A poling time of $\approx 5\,min$ is sufficient to induce a maximum in the nonlinearity, depending on parameters such as ion concentrations and their mobilities.

The registered $\chi^{(2)}$ value in bismuth-borate glasses results dramatically improved by decreasing the sample thickness, i.e. increasing the applied electric field. Specifically, in $BZH7$ samples poled at $4kV$, $350^oC$ for $5min$, the *SHG* signal increases by two orders of magnitude in $0.2\,mm$ thin samples compared to $1.0\,mm$ thick samples, as shown in Figure 4.6 (bottom). The existence of a poling time which maximizes $d_{33}$ was already observed in silica-glass slides by studying the temporal evolution of the second-order nonlinear coefficient (Faccio et al., 2001b), likely because the nonlinear depth is expected to increase with the poling time (see Equation 2.3). However, the sample thickness in silica would affect the time constant associated with the decay of the poling current (Equation 2.4) rather than the formation dynamics and the amount of $\chi^{(2)}$.

In summary, second-harmonic powers as high as in silica are generated in $BZH\diamond$ compounds at a few Celsius degrees below the glass transition temperature. The glass compounds are affected by large thermal stress during poling and slow heating and cooling phase are required in order to avoid breaking of the samples. Finally, the efficiency

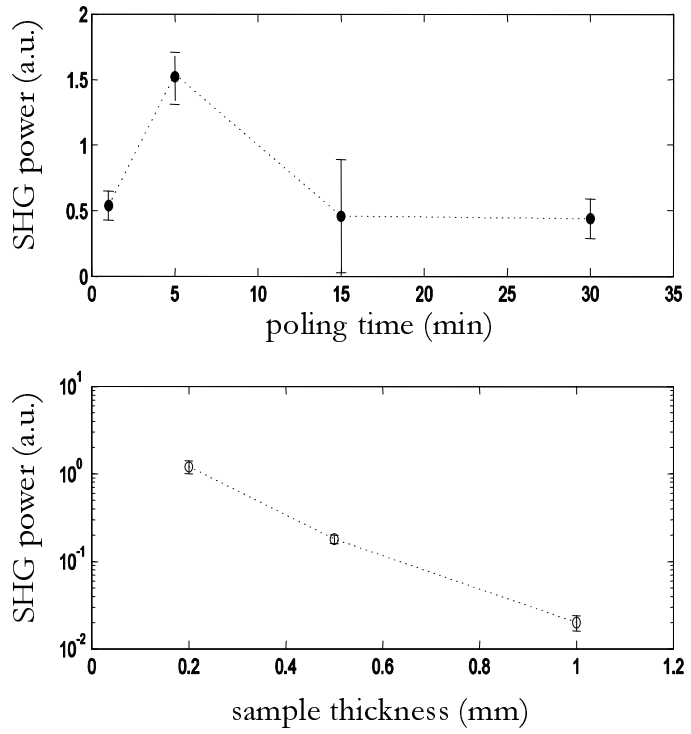


FIGURE 4.6: Normalized *SHG* power as a function of poling time and sample thickness. The reference sample is a $0.5\,mm$ thick Herasil1 plate, poled at $280^oC$ and $4\,kV$ for $30\,min$. Top: $BZH7$, $400^oC$, $4kV$, $1.0\,mm$. Bottom: $BZH7$, $350^oC$, $4kV$, $5\,min$. Error bars indicate the standard deviation of $SH$ signal across the poled area.

of $SH$ generation is measured to depend on the ratio between poling and glass transition absolute temperatures, the poling time and the sample thickness.

### 4.2.3 Second order nonlinearities in $BZH\diamond$ glass

In order to probe the poled samples as a function of $Bi_2O_3$ content, nonlinear characterization is carried out by employing the Maker Fringe technique (Section 3.2).

In Figure 4.7, Maker Fringe curves from all $BZH\diamond$ samples exhibit the characteristic shape of thin nonlinear layer, where $\omega \leq l_c$; to be more precise, the $SH$ signal peaks around $60^o$ and decreased at larger incident angles due to Fresnel losses. Etching the poled sample and measuring the *SHG* power as a function of the etched depth has revealed that the nonlinearity is located in a near-surface layer at the anode side. A nonlinear thickness of $6 \pm 0.5\,\mu m$ ($\approx$ 2/3 $l_c$) is measured from the inset in Figure 4.7 after successive etching and *SHG* measurements on a poled $BZH7$ sample. The highest second-order nonlinear coefficient $\chi^{(2)}_{33}$ measured in the $Bi_2O_3$-based samples are listed in Table 4.5 as a function of the bismuth-oxide content (Deparis et al., 2005b).

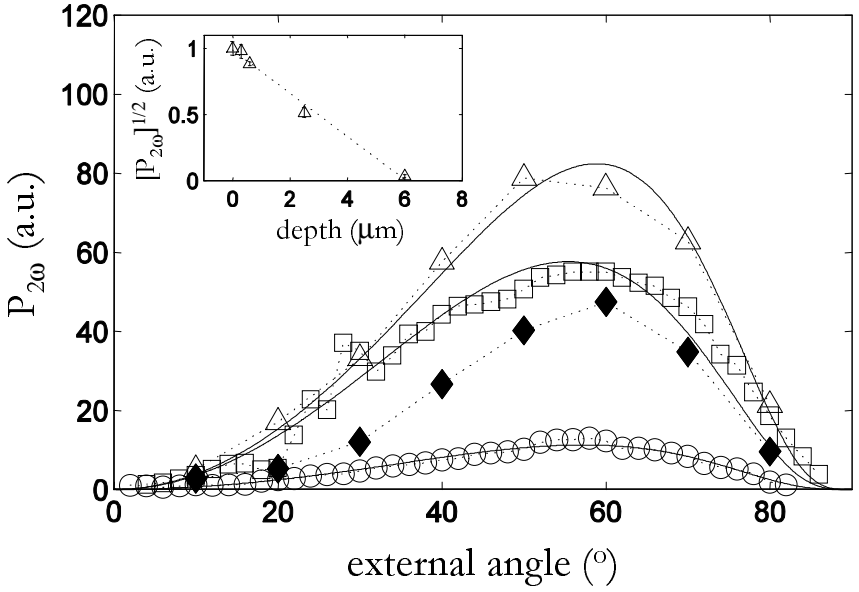


FIGURE 4.7: Maker fringe curves of poled $BZH\diamond$ samples: dotted lines connect data points, whilst lines are best fits. Samples and poling conditions as listed in Table 4.5: $BZH6$ full diamonds, $BZH4$ squares, $BZH7$ triangles, $BZH2$ circles. Inset: square root of $SH$ power as a function of etched depth in $BZH7$; the etching rate is estimated as $0.8\,\mu m/min$ in 0.1% diluted $HNO_3$. Dotted line is a best linear fit.

| *sample* | $Bi_2O_3$ $(mol\%)$ | $d(mm)$ | $T_p(^oC)$ | $t_p(min)$ | $w$ $(\mu m)$ | $\chi^{(2)}_{33}(pm/V)$ |
|---|---|---|---|---|---|---|
| $BZH6$ | – | 0.9 | 500 | 15 | 11.0 | 0.15 |
| $BZH4$ | 6.25 | 1.0 | 450 | 5 | 13.3 $(\wedge)$ | 0.23 |
| $BZH7$ | 12.5 | 1.0 | 400 | 5 | 6.0 | 0.38 |
| $BZH2$ | 25.0 | 0.2 | 300 | 3 | 6.2 $(\wedge)$ | 0.59 |

TABLE 4.5: Second-order nonlinear coefficient ($\chi^{(2)}_{33}$) in poled $BZH\diamond$ samples. $d$: sample thickness; $T_p$: poling temperature; $t_p$: poling time; $w$: thickness of the nonlinear layer. The poling voltage is kept at $4kV$.

Nonlinear thickness and nonlinear coefficient are similar to those obtained in poled silica. The optimal poling temperature is related to the $T_g$, as already reported in thermally poled $PbO/B_2O_3$ glass (Xi et al., 2002). The $\chi^{(2)}$ values increase from $0.23\,pm/V$ to $0.59\,pm/V$ as $Bi_2O_3$ content increases from $6.25\,mol\%$ to $25.0\,mol\%$, and as does $\chi^{(3)}$. A $\chi^{(2)} \cong 0.15\,pm/V$ is also obtained in zinc borate host glass $BZH6$ poled for $15\,min$. For clarity, values of $w$ are determined by etching or assumed to be equal to $l_c$ ($\wedge$ in Table 4.5), in which case only a lower limit of $\chi^{(2)}$ is given. It is worth noting that

$\chi^{(2)}$ peak values may be slightly underestimated, having set $n_\omega$ and $n_{2\omega}$ as calculated in Table 4.3.

The $\chi^{(2)}$ value is verified to increase accordingly with $\chi^{(3)}$, which in turn increases with increasing the bismuth oxide content. However, $BZH\diamond$ compounds do not yield higher values than thermally poled silica yet, as predicted by the rectification model. The advantage of high refractive index is counterbalanced by low glass dielectric breakdown strength, which is believed to decrease with increasing $Bi_2O_3$ and measured to be up to 10-fold lower than silica, owing to electrons in bismuth orbitals being less tightly bonded (Deparis et al., 2005b). This latter result demonstrates the importance to select glass compositions on the basis of both $\chi^{(3)}$ and dielectric breakdown strength to succeed in enhancing second order nonlinearity.

In conclusion, results on the spatial distribution of the second-order nonlinearity in thermally poled bismuthate glasses have been reported. Although the $SH$ signal is still located in a near-surface layer at the anode side, poling conditions and dynamics are very different from those in silica and change dramatically with $Bi_2O_3$ content. Efficient poling treatments have to be carried out at a temperature close to the glass transition point and requires a very intimate glass-electrode contact. The efficiency of $SHG$ power is measured to depend on the poling time and the sample thickness. In Section 4.2.5, the issue of enhancing $\chi^{(2)}$ will be tackled with further investigations on the suitable composition to accomplish high $\chi^{(3)}$ in less conductive glasses.

### 4.2.4 Atmospheric effects upon measured poling current

In this section, some peculiarities of the poling current dynamics in $Bi_2O_3ZnOB_2O_3$ samples are described in comparison with standard poling of silica samples. A systematic inspection of the role played by the atmosphere during poling is provided, with a particular attention to the type of electrode used, the glass composition, the poling temperature and the sample thickness. Finally, a dielectric constant more than 65% higher than Herasil is measured in $BZH7$ samples.

In Figure 4.8 is plotted the current evolution measured for $1\,mm$ thick $BZH7$ samples poled for $5\,min$ at $400^oC$ (curve 2).

The poling current dynamics exhibit an increase of the current throughout the poling time required to obtain the $\chi^{(2)}$ values reported in Table 4.5. Deparis et al. (2005b) showed that this feature appeared to be common to both $Bi_2O_3$-free and $Bi_2O_3$-containing samples poled with gold-on-silicon electrodes, all other parameters being identical.

A tendency to current saturation is displayed instead by thinner samples ($d = 0.5\,mm$), as shown in curve 1 for identical poling conditions. In this case, the 'spikes effect' exhibited during the poling time becomes much more significant, probably as a result of

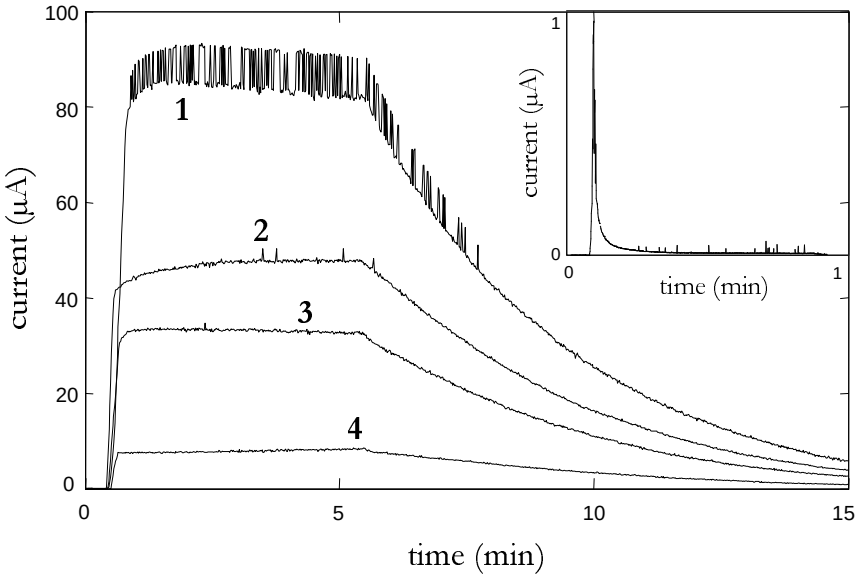


FIGURE 4.8: Poling current dynamics in $BZH7$ samples with different thickness: $1.0\,mm$(2, 4); $0.5\,mm$(1); $0.2\,mm$(3). Electrode material: gold on silicon ($7 \times 10mm$). Poling time: $5\,min$, $V = 4\,kV$, $T_p = 400^oC$ $(1, 2)$ and $T_p = 350^oC$ $(3, 4)$, respectively. Inset: Evidence of depletion region formation in type II silica glass. Poling conditions: $280°C$, $4\,kV$, $15\,min$, air atmosphere, anode: n-type silicon, cathode: stainless steel

local micro-sparks at the electrode-sample interface. The contact between the electrode and the sample seems to have an influence on the evolution of the poling current; the poling current dynamics in $BZH\diamond$ compounds changed dramatically with the material and the surface flatness of the electrodes (Deparis et al., 2005b).

The current measured in graph 3 of Figure 4.8 is relative to a $d = 0.2\,mm$ thick $BZH7$ sample. In this case, the poling temperature has to be lowered to $350^oC$ in order to avoid current avalanching ($> 1\,mA$) which leads to dielectric breakdown in the matrix. Curve 4 shows the current evolution of $1.0\,mm$ thick $BZH7$ samples at the same temperature. The initial current is proportional to the voltage and inversely proportional to the thickness, $d$, as predicted by

$$I = \frac{V \times S}{d \times \sigma(T_p)} \tag{4.3}$$

with $\sigma$ the glass conductivity at a given poling temperature and $S$ the electrode surface.

The inset in Figure 4.8 displays by contrast how the current typically evolves at $280°C$ across the specimen of a $0.2\,mm$ thick Herasil sample during the first minute of poling with $4\,kV$ applied to pressed-contacted Si-electrodes. Its rapid decrease with time is due to the formation of a cation-depleted layer under the anodic surface which acquires a much higher resistivity than the bulk, as described in Section 1.1.1.

The absence of the current decay in $BZH\diamond$ glasses, always displayed during poling of silica, along with the different evolution exhibited in current $vs$ time measurements are here attributed to the high electronic contribution to current, masking ionic migration during poling. In bismuth-based glasses, proton conduction is still believed to take place (Carlson, 1974), as the poling temperature is only few degrees lower than $T_g$ (see Figure 4.5). In the following section, the experimental evidence of proton conduction is given, as previously reported in hydrous $BaSi_2O_5$5 glass (Behrens et al., 2002). Proton conduction is here associated with the presence of hydroxyl ($OH$) in all $BZH\diamond$ samples.

#### 4.2.4.1 Guard ring to prevent surface current measurement

To gain better understanding on the conduction mechanism during poling of bismuthate glasses, current dynamics versus temperature in the presence of high voltage applied to $BZH7$ samples are analyzed. In order to isolate any contribution coming from surface current, comparisons are carried out when using a guard ring electrode configuration rather than pressed gold on silicon electrodes.

The guard ring is formed by a thin film of Au ($100\,nm$) on top of Ti ($30\,nm$) evaporated all around the cathode electrode of the sample to prevent the surface current detection from the ammeter in Figure 4.4. The guard ring shape is given by photolithographically exposing the metal coating through a mask, followed by a reactive-ion etching process. The mask is designed to allow two symmetrical disks of $5\,mm$ in diameter deposited on both side of the $BZH7$ sample: they play as anode and cathode electrodes, respectively. Three Au wires are press-bonded to the guard ring and grounded in order to isolate it from the anode. Only a wire is actually needed. A detail of the microscope image of the guard ring geometry is given in Figure 4.9

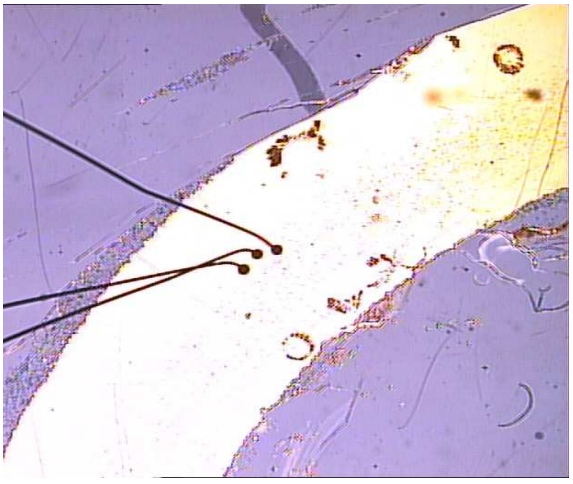

FIGURE 4.9: Optical microscope view of Au wires ($\phi = 25\,\mu m$) connected to the guard ring deposited on a $0.3\,mm$ thick $BZH7$ sample to prevent the surface current.

In such a guard ring configuration, the study of the current evolution with the temperature during poling of bismuthate glass is carried out. In particular, the current is recorded as a function of temperature when 0.3 $mm$ thick $BZH7$ samples are heated from room temperature ($T_{room}$) up to 400$^oC$, at the controlled rate of 1$^oC/min$. While the temperature increases, the samples are submitted to 4 $kV$ at regular intervals of 5 $min$. The voltage is applied for a time long enough (30 $sec$) for the second-order nonlinearity to appear (Quiquempois et al., 2000a).

In Figure 4.10, the comparative study of current variation with temperature is shown when the high voltage is applied in air atmosphere to pressed-on Au on Si electrode (*blue*) and guard ring around evaporated electrode (*yellow*), respectively. Also shown is the current trend measured in vacuum atmosphere when circular electrodes are evaporated on both sides but no guard ring is employed (*green* in Figure 4.10).

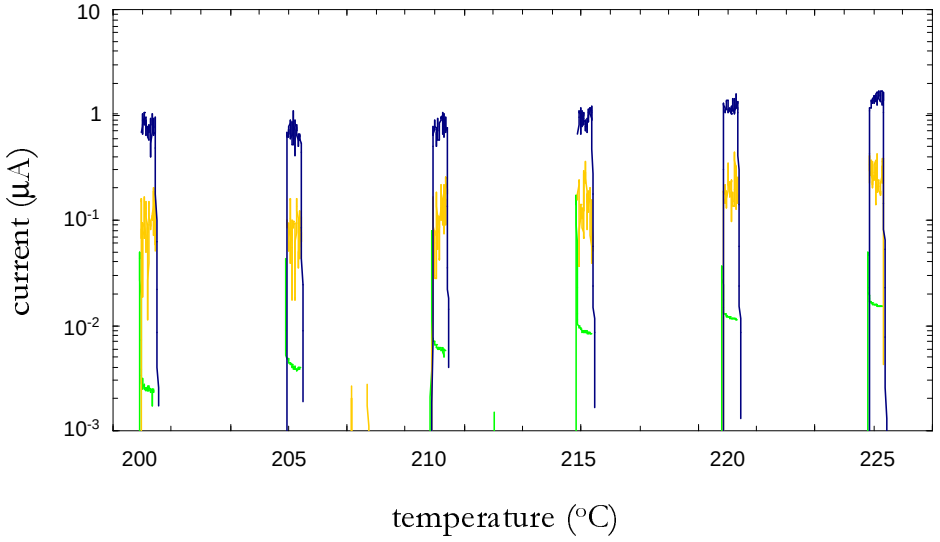


FIGURE 4.10: Current variation with temperature while 4$kV$ are applied for 30$sec$ at 5$min$ interval. Pressed-on Au on Si electrode in air (*blue*), evaporated electrode and guard ring in air (*yellow*), evaporated electrode in vacuum (*green*).

All other parameters being identical, the average value of current measured in air when using a guard ring electrode configuration is almost 10 *times* smaller than without the guard ring. Therefore, the current detected by the external circuit in Figure 4.4 is effectively higher than the current flowing through the sample when poling is carried out with pressed gold on silicon electrodes. As humidity can affect the surface resistivity, surface current contributions are expected to be strongly reduced if the experiment is carried out in vacuum instead. Under vacuum, atmospheric injection of cationic species ($H^+, H_3O^+$) into the glass can not occur; therefore, the poling current dynamics is believed to reflect only the conduction mechanisms that are intrinsic to the glass (Pruneri et al., 1999b). To reduce atmospheric effects upon measured poling current, experiments are performed by placing the sample in a vacuum chamber.

The vacuum chamber ($p < 5 \times 10^{-6}\, torr$) is heated up by a resistive ceramic heater ($500\, W, 230\, V$), whose non-uniform radiation is continuously monitored and corrected by a closed-loop control system. Using identical experimental procedures to those above, clear evidence of current decay can be observed in vacuum for temperatures ranging from $200^oC$ to $300^oC$, as partially shown in Figure 4.10 (green curve). This decay may be indicative for initial building-up of the space charge field underneath the anodic surface. No current decay is observed in the range $300^oC/400^oC$ (not shown in Figure 4.10), likely because more complex charge transport mechanism could contribute to the dominant conduction process in $Bi_2O_3$-based samples throughout poling at high temperature. The average current values result to be more than two order of magnitude lower in vacuum than in air atmosphere, comparing the *green* and *blue* curves in Figure 4.10, respectively. The same experiment is performed in vacuum using both evaporated electrode and pressed gold on silicon electrode, showing no significant difference. For completeness, the $SHG$ signal induced in vacuum on a $0.3\, mm$ thick $BZH7$ sample is very dis-homogeneous across the anode area and its magnitude is two order lower than identical poling in an air atmosphere ($T_p = 300^oC$, $t_p = 5\, min$, $V_p = 5.1\, kV$).

More experiments are therefore required to establish how the current measured in vacuum may be still influenced by surface current paths. For this purpose, it may be worth investigating the current variation with temperature in the presence of high voltage when the guard ring configuration is adopted in vacuum as well.

In conclusion, from the study of the current evolution with the temperature during poling of bismuthate glass, the real value of the poling current has been shown to be mostly masked by surface contributions, which can be attributed to the presence of different atmospheric species playing a role in the $\chi^{(2)}$ formation by thermal poling. Finally, it is not possible to obtain conclusive information on the physical process from the current measurement, unless a guard ring is introduced into the poling set up.

#### 4.2.4.2 Activation energy

In this section, the activation energy value of $12.5\, mol\%$ bismuth-oxide glass is estimated using the results obtained from the study of the current evolution with the temperature in Section 4.2.4.1. In particular, the experimental data are relative to the average current values of the $BZH7$ sample poled in air with evaporated electrode and guard ring (*yellow* curve in Figure 4.10).

A graph of the electrical $DC$ conductivity as a function of reciprocal absolute temperature is plotted in Figure 4.11. From the best linear fit to Arrhenius law, the value of the activation energy is calculated to be $E_\sigma = 1.32 \pm 0.26\ eV$ in $BZH7$ poled in air with evaporated electrode in the guard ring configuration, slightly lower than the value $E_\sigma$=1.5 estimated by Deparis et al. (2005b) when pressed gold on silicon electrode

only are used. However, this activation energy $E_\sigma$ is more than 65% higher than that reported for thermal dissociation of a single charge carrier such as $Na^+$ in silica (Bansal and Doremus, 1986), thus supporting a charge transport mechanisms in $BZH\diamond$ glasses which involves both electronic and ionic conductivity. More details on such a poling mechanism are presented in the following section.

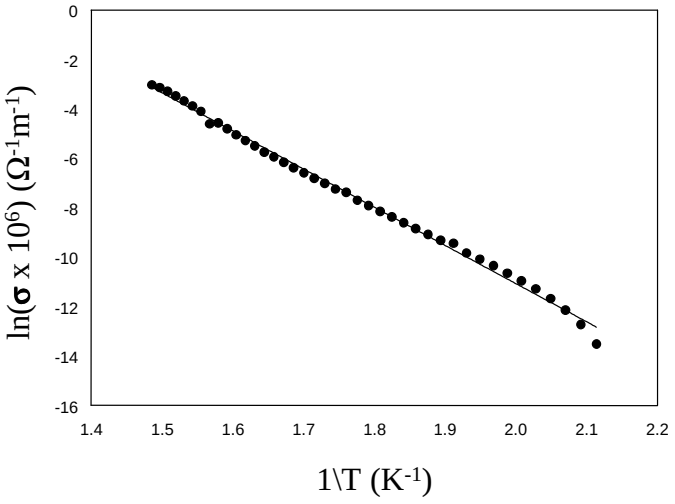


FIGURE 4.11: Electrical $DC$ conductivity ($\sigma$) as a function of the reciprocal absolute temperature ($T$) in $BZH7$ sample. Line is best linear fit to Arrhenius law: $\sigma = \sigma_o \times exp[-E_\sigma/K_B T]$ where $\sigma_o$ is the pre-exponential factor, $E_\sigma$ is the activation energy, $K_B$ is the Boltzmann constant. Temperature range: $200^oC$-$400^oC$. The experiment is carried out in air with evaporated electrode and guard ring.

### 4.2.5 The effect of high conductivity upon the poling efficiency

The nature of conductivity in $Bi_2O_3ZnOB_2O_3$ glasses has not so far been clearly established. Some of the most plausible charge transport processes are discussed to interpret experimental data on conduction in these new glass matrices during thermal poling.

Ionic conduction has been suggested in the case of bismuth silicate and bismuth germanate, where it is asserted that oxygen ions are the charge carriers and percolation in $BiO_{5-6}$ sub-network is the charge transport mechanism (B.Kusz, 2003). Migration of $O^{2-}$ during poling would create an anion-depleted region at the cathode, assuming that the electrodes are blocking for $O^{2-}$. If there was any ionic conduction in $BZH\diamond$ samples, it should involve cations and not anions since the nonlinearity is found to be at the anode side rather than at the cathode side.

Electronic conduction has been reported in bismuth borate glasses (Yawale and Pakade, 1993), involving electron hopping between bismuth ions of different valence states ($Bi^{3+}$ and $Bi^{5+}$). Electron hopping can not create electrically charged layers since at all time electrons enter at the cathode (no charge depletion) and exit at the anode (no charge

accumulation). Nonetheless, although electron hopping conduction could be the dominant contribution to conduction mechanism at high $Bi_2O_3$ content, in $BZH\diamond$ samples there are evidences that a cation-depleted near-surface layer is created at the anode side, supported by observations of anodic bonding and decay of the poling current in $0.3mm$ thick $BZH7$ samples in vacuum (see Section 4.2.4.1).

The presence of hydroxyl ions in all $BZH\diamond$ samples in the form of $\equiv Si-OH$ dangling bonds (see Table 4.2) could support conduction through protons ($H^+$) moving in the glass matrix at temperatures close to $T_g$. The effect of the poling treatment on the weight percentage of hydroxyl $OH$ bonds is revealed from measurements of the absorption peak around $2.9\,\mu m$. In Figure 4.12, the absorbance spectra measured on $20\times30\times0.3\,mm^3$ pristine (*pink*) $BZH7$ sample is compared with that measured after poling it in air for $5\,min$ at $300^oC$ at two different voltages: $V_p = 6.4\,kV$ (*yellow*) and $V_p = 7\,kV$ (*blue*), respectively. The absorbance is calculated by $\alpha = [log(1/T) - log(1/T_0)]/L$, where $T$ is the measured transmission loss. The absorbance spectra measurements display more than 15% decrease in the $OH$ content in the poled area of a $BZH7$ sample when compared to an unpoled region (*blue* and *pink*, respectively). All the other parameters being identical, the residual $OH$ content depends inversely on the poling voltage, as deducted by comparing the *blue* ($V_p = 7\,kV$) and *yellow* ($V_p = 6.4\,kV$) curves in Figure 4.12.

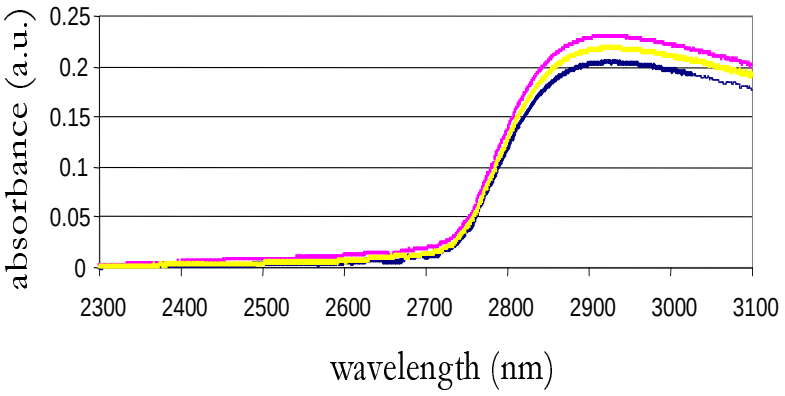


FIGURE 4.12: Absorbance spectra measured on $20\times30\times0.3\,mm^3$ $BZH7$ poled in air for $5\,min$ at $300^oC$: $V_p = 7\,kV$ (*blue*), $V_p = 6.4\,kV$ (*yellow*), pristine (*pink*), respectively.

After poling the sample at such a high voltage, the experimental evidence of the dissociation of $OH$ bonds and the release of protons in $BZH7$ glasses is obtained. Assuming that protons and electrons are the mobile charge carriers, a multi-carrier migration model is now proposed for describing the poling mechanism in bismuth-borate glasses and accounting for most of the experimental results.

The mobility of $H^+$ carriers is highly enhanced with temperature, which does satisfy the requirement of poling temperature a few degrees below $T_g$. Under the action of the applied electric field, protons migrate toward the cathode, leaving negatively charged dangling bonds $B-O\bullet^-$ behind them. As a result, a space charge field builds up under

the anode, which peaks at the surface, decreases linearly with depth in the proton-depleted layer and is constant across the rest of the bulk. This simple model supports the location of the nonlinearity in a near-surface layer at the anode side. On the other hand, near $T_g$ a partial orientation of the electrical dipoles associated with these dangling bonds may occur in the direction opposite to the applied electric field. Freezing of the space charge field and/or dipole orientation results in the creation of $\chi^{(2)}$ through the rectification of $\chi^{(3)}$ by the internal d.c. field and/or through individual contributions of dipole hyperpolarizability.

The observed anodic bonding (Section 4.2.2) can be interpreted as macroscopic electric-field assisted interaction between $\equiv Si^+$ (wafer) and $B-O\bullet^-$ (sample) at the glass electrode interface. A more accurate description of the poling mechanism would still take into account the possibility of ionization and ion injection driven by high electric fields. Once the space charge field strength in the glass exceeds its dielectric breakdown, injection of ionized species from the atmosphere ($H^+$, $H_3O^+$) and ejection of negative charges, such as electrons or oxygen ions (Matos et al., 2000), can take place at the anode, modifying current dynamics and the depth distribution of the space charge. If the glass-electrode contact is not perfect, those ionized species penetrate into the sample diffusing in the depth and may recombine with fixed negative charges left by the migration of internal ions; more concisely, the internal ions are substituted by injected ions in analogy with an ion-exchange process. Such a process is reported to happen during thermal poling of silica (Alley and Brueck, 1998) but it does not have a significant impact on the nonlinearity because the substituting ions ($H^+$, $H_3O^+$) have a much lower mobility than sodium. In the case of $BZH\diamond$ glasses, on the other hand, substitution ions and internal ions are either the same ($H^+$) or similar ($H_3O^+$) and therefore the ion-exchange process is believed to be much more efficient. The competition between the formation of $B-O\bullet^-$ and the injection of ($H^+$, $H_3O^+$) has a net effect upon the poling efficiency which depends in turn on injection and poling conditions.

The above considerations explain why $BZH\diamond$ glass nonlinearity is so critically dependent on the glass-electrode contact and the poling atmosphere. It is concluded that the poling mechanism relies on the migration of protons. The importance of the glass electrode contact is explained by the injection of $H^+$ and $H_3O^+$ from the atmosphere which tends to neutralize the depletion layer resulting from the migration of internally released $H^+$. Ionization of the glass occurs and plays a role in the formation of $\chi^{(2)}$.

Electron hopping between multi-valence $Bi$ ions, on the other hand, does not contribute to the formation of $\chi^{(2)}$, although it does to the conduction process, as verified by comparing it to current measurement on $Bi$-free samples (Deparis et al., 2005b). Moreover, the electronic current is expected to increase dramatically with increasing $Bi_2O_3$ content, so to hide the contribution from proton migration. Unlike ions, electrons can not be blocked at the electrodes and therefore can not create a near-surface depletion (or

accumulation) space charge layer; however, they may be involved in reduction-oxidation chemical reactions at the glass-electrode interfaces.

Based on the proposed poling mechanism, a simple model relating the second-order nonlinear susceptibility induced in poled bismuthate glasses to their electronic and ionic conductivity is proposed in the next section. In particular, it is predicted why bulk electronic conductivity higher than ionic conductivity may prevent the achievement of a frozen-in electric field large enough to generate efficient second order nonlinearities in $Bi_2O_3$-based glasses.

#### 4.2.5.1 Conductivity model for efficient poling of bismuthate glass

In what follows, the equivalent electrical $DC$ circuit of $BZH7$ glass samples after poling sets the starting point towards quantitative understanding of their $\chi^{(2)}$ formation and dynamics.

Assuming all the charge transport processes in Section 4.2.5 as independent from each other, the current, $i$, in the external circuit is considered in first approximation as the sum of contributions associated with ionic migration ($i_{ion}$) and electronic conduction ($i_e$):

$$i \cong i_{ion} + i_e \tag{4.4}$$

After poling, the cross-section of the glass may be schematically represented by a two layer structure, as sketched in the left hand side of Figure 4.13. The voltage applied to the sample would then be distributed across the sample according to the equivalent $DC$ circuit drawn at the right hand side in Figure 4.13.

In the hypothesis of the electric field in both the depletion layer and bulk being constant:

$$V_{app} = V_d + V_b = E_{DC} \cdot \omega + E_b(L - \omega) \tag{4.5}$$

and the built-in electric field $E_{DC}$ may be estimated by:

$$E_{DC} = \frac{E_{dep}}{1 + \left(\frac{\frac{1}{\beta}+\alpha}{\delta+1}\right)\left(\frac{L}{\omega} - 1\right)} \tag{4.6}$$

where the electric field in the depletion layer is given by $E_{dep} = \frac{V_{app}}{\omega}$, and the bulk/depletion layer conductivities are related by:

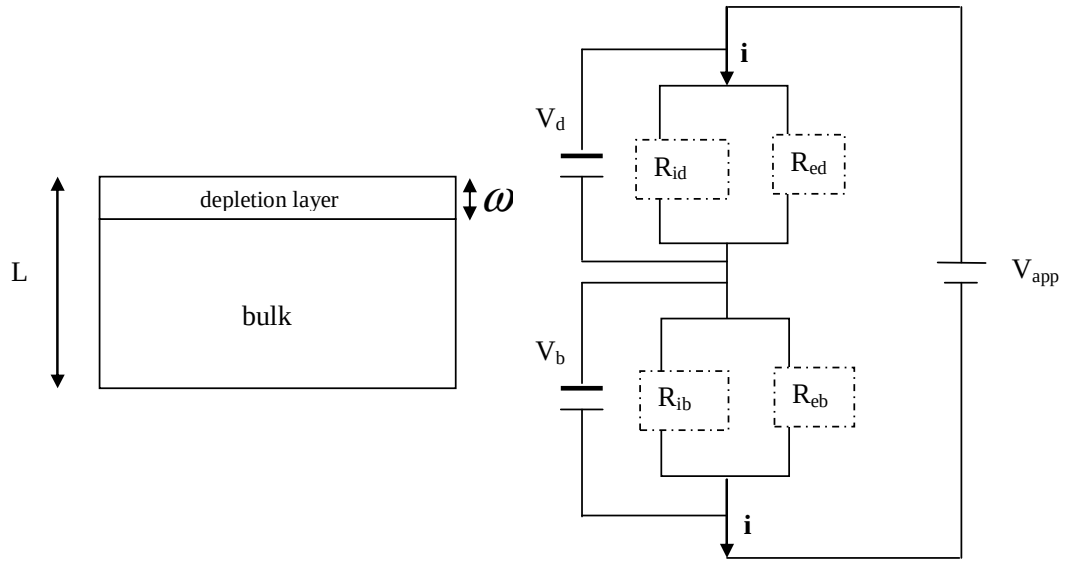


FIGURE 4.13: Scheme of the structure of the glass after poling. $L$ is the sample thickness and $\omega$ is the depletion layer thickness. The equivalent $DC$ electrical circuit is represented in the scheme on the right hand side, where $R_d$: equivalent resistance (ionic and electronic) on the depletion layer; $R_b$: equivalent resistance (ionic and electronic) on the bulk; $V_{app}$: applied voltage; $V_d$: voltage across depletion layer; $V_b$: voltage across bulk.

$$\alpha = \frac{\sigma_{id}}{\sigma_{ib}} \tag{4.7}$$

$$\beta = \frac{\sigma_{ib}}{\sigma_{ed}} \tag{4.8}$$

$$\delta = \frac{\sigma_{eb}}{\sigma_{ib}} = \frac{\sigma_{eb}}{\beta \cdot \sigma_{ed}} \tag{4.9}$$

with $\sigma_{ed}$ and $\sigma_{id}$, the electronic and ionic conductivity at the depletion layer; $\sigma_{eb}$ and $\sigma_{ib}$, the bulk electronic and ionic conductivity, respectively. Now, if the intrinsic non-linear third-order $\chi^{(3)}$ susceptibility is rectified by the electric field $E_{DC}$, according to Equation 1.2, the nonlinear second-order $\chi^{(2)}$ susceptibility in thermally poled $BZH7$ glass may be evaluated using Equation 4.6.

The trend of $\chi^{(2)}$ as a function of $\beta$ is shown in Figure 4.14, in the hypothesis of ionic conductivity in the bulk being much larger than in the depletion layer ($\alpha \cong 10^{-7}$) and with the enhancement factor given in Table 4.2, $\omega = 4\,\mu m$ and $L = 0.3\,mm$.

For small $\beta$, the electronic conductivity of the glass would prevent significant voltage drop over the depletion layer, therefore a high electric field could not be recorded in the depletion layer and consequently large $\chi^{(2)}$ values would be prohibited. Moreover,

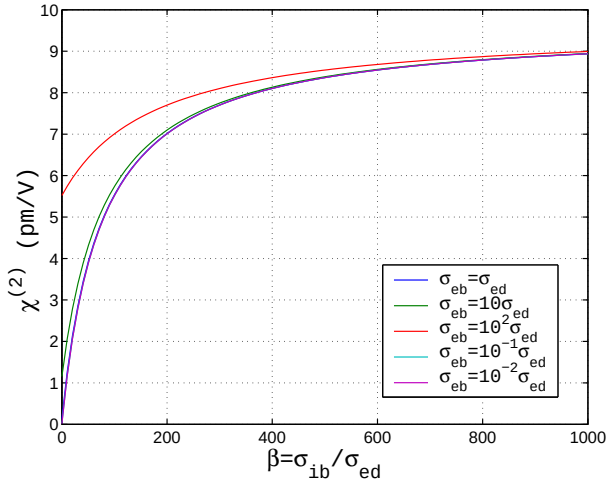


FIGURE 4.14: $\chi^{(2)}$ as a function of $\beta = \frac{\sigma_{ib}}{\sigma_{ed}}$ for various ratio between $\sigma_{eb}$ and $\sigma_{ed}$.

to succeed in enhancing the second order susceptibility, glass compounds with bulk electronic conductivity higher than $\sigma_{ed}$ ought to be tested.

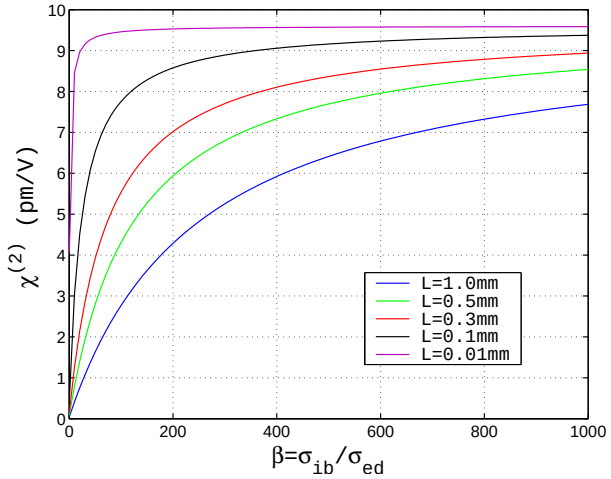


FIGURE 4.15: $\chi^{(2)}$ as a function of $\beta = \frac{\sigma_{ib}}{\sigma_{ed}}$ for various sample thicknesses if $\sigma_{eb} = \sigma_{ed}$.

Finally, the simulated trends for different sample thicknesses are plotted in Figure 4.15, in the hypothesis of constant electronic conductivity throughout the sample (i.e. $\delta = \frac{1}{\beta}$). Interestingly, the poling induced $\chi^{(2)}$ value seems to benefit from smaller sample thickness, as already verified in Section 4.2.2. It is worth noting that even a small increase in $\sigma_{ib}$, such as $\sigma_{ib} = 10 \cdot \sigma_{ed}$, would cause the $\chi^{(2)}$ value to double.

The model proposed shows that high conductivity may critically influence efficient generation of $SH$ signal in poled $BZH7$ glasses and this must be investigated, to be confirmed. Compounds with equivalent $Bi_2O_3$ content are expected to display different electronic behavior if their melting point is adjusted during the fabrication process. In Chapter 5, thermal poling treatments on $BZH7$ batches with different electronic conductivity are

performed for comparison, showing results in accordance with this conductivity model. Experiments on $BZH7$ glass samples with different thickness are also performed.

## 4.3 Conclusion

Second-order optical nonlinearity is induced in high index bismuth borate ($Bi_2O_3 - ZnO - B_2O_3$) and borate ($ZnO - B_2O_3$) glasses by thermal poling. Values of $\chi^{(2)}$ as high as $0.7\,pm/V$ are reported on $25.0\,mol\%$ $Bi_2O_3$ glass, rendering thermally poled bismuth borate a competitor to silica-based technology. Assuming that the rectification model is valid, further improvements are theoretically achievable. The incorporation of bismuth in the matrix increases the $\chi^{(3)}$ of the glass while reducing the $T_g$. The dielectric breakdown strength is believed to decrease likewise, because electrons in bismuth orbitals are less tightly bound.

Poling conditions are significantly different from those for silica: poling temperatures have to be relatively close to the glass transition temperature; an intimate glass-electrode contact is required to achieve *SHG* uniformity in the poled area; dramatic changes in the $\chi^{(2)}$ formation dynamics are experienced by varying the sample thickness results; the conductivity is much higher than in silica and very different current dynamics are exhibited depending on the $Bi_2O_3$ content. In spite of these differences, the nonlinearity is located in a near-surface layer at the anode side, as in thermally poled silica, and the nonlinear layer thickness is measured to be less than coherence length. A poling mechanism relying on proton migration and glass ionization has been proposed to account for all the experimental evidence leading to $\chi^{(2)}$ formation. However, if the frozen-in field had already reached the limit set by dielectric breakdown ($E_{DC} \approx E_{breakdown}$), these results would imply that the dielectric breakdown strength is lower in $BZH\diamond$ glasses than in silica and decreases with increasing $Bi_2O_3$ content. In the next chapter, the innovative time-varying voltage technique (Mezzapesa et al., 2005) is extended at bismuthate $BZH7$ glasses to enhance their poling induced in-built electric field, and consequently their second order susceptibility.

# Chapter 5

# Poling using time-varying voltage

## 5.1 Introduction

Second-order susceptibility related to the formation of a space-charge region is widely accepted as the macroscopic effect of thermal poling. The standard process induces ionic migration by a high static electric field applied across a pre-heated amorphous material and subsequently freezing it with the same voltage still applied (Section 2.2). While several studies have investigated how the *SHG* dynamic behaves in respect to different poling parameters, such as time (Alley et al., 1999), voltage (Triques et al., 2000), (Martinelli et al., 2002), atmosphere (Pruneri et al., 1999b), none to date has been performed when the voltage is increased during the cooling phase. By employing this new voltage-assisted treatment, the frozen-in electric field is significantly improved in comparison with the standard poling procedure, for identical conditions at the start of it. Moreover, the second order susceptibility $\chi^{(2)}$ doubly benefits when the initially constant voltage is raised during cooling, owing to the combined result of both reduced nonlinear depth and dramatic enhancement of the second harmonic signal (Equation 3.1). Experimental evidence of in-built electric field strengthening is provided throughout this chapter; moreover, control of the nonlinear region evolution is also gained by modifying the standard constant-voltage poling procedure, which will lead towards optimizing the integration of nonlinearity in waveguiding regions.

## 5.2 A new route to enhance $\chi^{(2)}$ in silica

The following three sections report on a comparative study between variable-voltage and standard thermal poling carried out in air atmosphere on two sets of Herasil1 samples, with thickness of $S = 0.2\,mm$ and $1.0\,mm$, respectively. Section 5.3 details how to extend this new route to bismthate $BZH7$ glasses towards achieving further enhancement in their second order nonlinearities.

In order to determine how time-varying voltage affects the $SON$, the poling time and temperature are set at $t_p = 10\,min$ and $T = 280^oC$, respectively. Two pressed-contact n-type silicon plates are used to apply an initial constant voltage across the samples in the range between 2 and $5\,kV$. After $t_p$, either the same or a higher voltage is applied across the electrodes during the first minutes of the cooling phase.

The current evolution is compared in Figure 5.1 for Herasil1 samples poled in the standard way at $V = 3\,kV$ (*black*) and $5\,kV$ (blue), respectively. In orange, the current measured when the voltage $V_{initial} = 3\,kV$ is raised to $V_{cooling} = 5\,kV$ during cooling is shown. Once the final voltage is applied, the sample conductivity varies, regardless of the initial poling voltage.

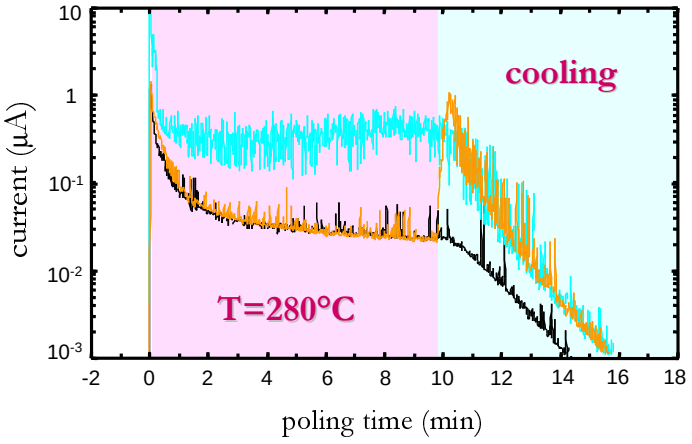


FIGURE 5.1: Current evolution in $0.2\,mm$ thick Herasil1 during standard poling ($3\,kV$ (black) and $5\,kV$ (blue), respectively) and increasing voltage during cooling $3 \Rightarrow 5\,kV$ (orange).

Investigation of the spatially resolved evolution of the depletion region when both standard constant-voltage and variable-voltage cooling is discussed in Section 5.2.1. Direct $\chi^{(2)}$ detection proves the efficiency enhancement when the innovative poling procedure is adopted and electric field measurements are performed in Section 5.2.3 to confirm the mechanism.

### 5.2.1 Nonlinear thickness evolution: transverse etching and layer peeling reconstruction

The width of the depletion region in thermally poled Herasil1 samples is characterized here after both standard and modified poling procedures. Two experimental techniques are employed to confirm these findings, namely optical microscope inspection of the cleaved sample after transversally etching it and real-time interferometric measurement of the etching rate in the layer peeling method, as described in Section 3.3.

Figure 5.2 describes the trend of the nonlinear boundary depth below the anode surface as measured by microscope inspection after cross sectional etching in 48% hydrofluoric ($HF$) acid for $1\,min$. The microscope image of the sample cross-section after etching is shown in the inset. A ridge at about $10\,\mu m$ from the sample surface is observed, which reflects the edge of the depletion region, where the etching rate is reduced by a change in the local field distribution (Alley and Brueck, 1998).

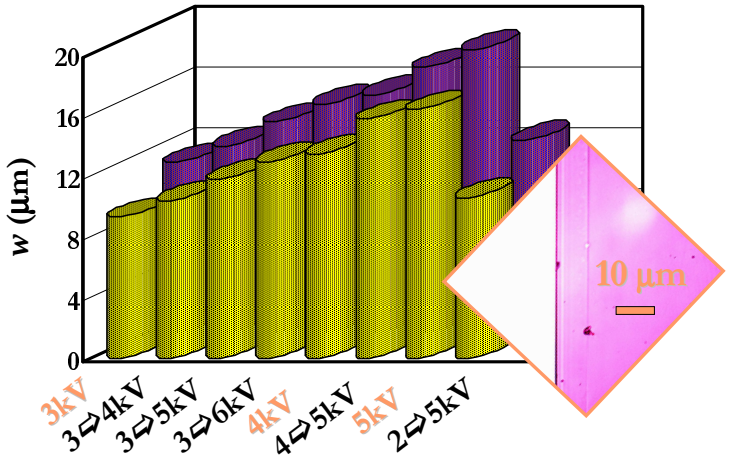


FIGURE 5.2: Spatially resolved evolution of the depletion region when both standard constant-voltage and variable-voltage cooling are performed (orange and black on the $x$-axis, respectively). The Herasil1 sample thickness is either $0.2\,mm$ (*violet*) or $1.0\,mm$ (*yellow*). The microscope image of the depletion layer as in the inset.

When standard poling is performed (e.g. $3\,kV$ continuously applied), increases in the voltage induce a monotonic increase in the nonlinear region width (40% bigger for $5\,kV$), as predicted in the single-carrier model (Equation 2.5). The trend is even confirmed in $0.2\,mm$ thick samples (*violet* in Figure 5.2), whose deeper nonlinear thicknesses are consistent with the increase of the volume electric field applied across them (Faccio et al., 2001b). Equivalent experiments carried out on Infrasil samples lead to identical results as in Herasil1. Comparable nonlinear depth ratios are measured on Infrasil glasses (as reported in Figure 3.6) when studying the evolution of their normalized $SH$ peak power versus etching time, if it is assumed that the nonlinear signal is zero only where the in-built electric field is zero.

If the voltage is raised after the first $t_p = 10\,min$ (e.g. $V_{initial} = 3\,kV$ increased to $V_{cooling} = 5\,kV$), the nonlinear depth in Herasil1 samples evolves slowly with the voltage. More, Figure 5.2 depicts how the nonlinear width increases much less compared to the constant-voltage case, for identical final voltage (e.g. $5\,kV$).

The accumulation model (Qiu et al., 1999a) is invoked to explain the poling process and the formation of the second-order nonlinear layer. It is assumed that the depletion layer is formed by both positive and negative ionic flux. The negative charges gather in the anodic region due to the potential barrier between glass and air, high enough to

obstruct them from completely flowing out to the anode; whereas the positive ions drift to the cathode, and the distance of drift is proportional to ions mobility, poling time and mainly final poling voltage. As a result, the separation of positive and negative ions spatially define the second-order nonlinear layer, whose thickness modulates the strength of the frozen-in electric field, and consequently $\chi^{(2)}$ in that region.

In conclusion, a revisited version of the standard poling procedure has been investigated. Control on the nonlinear region depth can be achieved by controlling voltage during poling, which will be exploited to integrate nonlinearity in waveguiding regions.

### 5.2.2 Nonlinear susceptibility evolution

The normalized $\chi^2$ profiles retrieved by layer peeling algorithm are compared in Figure 5.3 for three $0.2\,mm$ thick Herasil1 silica glasses poled as detailed in Figure 5.1.

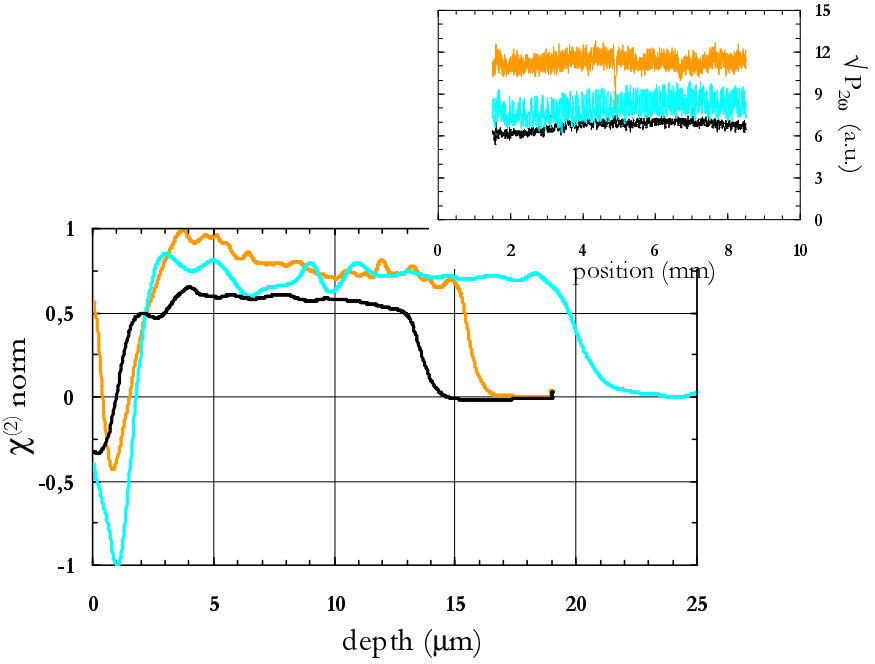


FIGURE 5.3: Normalized $\chi^{(2)}$ profiles retrieved by the layer peeling algorithm for three $0.2\,mm$ thick Herasil1 samples identically poled for $10\,min$ in air at $280°C$, with constant voltage $3\,kV$ (black), $5\,kV$ (blue), and with voltage increased during cooling from 3 to $5\,kV$ (orange), respectively. The square root of the $SH$ signal across the poled area is plotted in the inset.

The normalized nonlinear optical efficiency decreases with etching time. When it reaches the detection threshold, the difference in depth is quantitatively predicted by Equation 2.5 and the ratio between the relative total removed silica thickness is in accordance with Figure 5.2. Strong similarities can be found with the recovered profile shown in Figure 3.7 for $0.5\,mm$ thick Infrasil disks, similarly poled in an air atmosphere, although under different conditions. In all cases, the $\chi^2$ value is initially negative beneath the

anode surface and then reverses its sign to finally tail off in the depth. Here, the retrieved profiles exhibit unexpected fluctuations which are likely ascribed to the detection system, and are not considered statistically significant.

The inset shows the spatial distribution of the square root of the $SH$ signal which is generated by scanning the pump beam across the sample. During this measurement, the samples is mounted on the standard Maker Fringe apparatus at the incident angle which maximizes the $SH$ generation. The $SH$ signal ($\sqrt{P_{2\omega}}$) is uniform under the anode, and its average value increases of 30% when the voltage is heightened during cooling, for identical final voltage (*orange* and *blue*, respectively).

In the hypothesis of $w$ shorter than the coherence length, the *sinc* factor on the right hand side of Equation 3.1 changes very slowly with $w$, thus $\chi^{(2)}$ may scale with the $SHG$ signal approximatively as:

$$\chi^{(2)}_{eff} \propto \left( \frac{\sqrt{P_{2\omega}}}{\omega} \right) \tag{5.1}$$

which implies that increasing the applied voltage during cooling increases the absolute value of $\chi^{(2)}$ owing to second harmonic signal enhancement combined with a reduced nonlinear depth. Figure 5.4 shows the nonlinear susceptibility evolution as a function of standard and variable voltage procedure on a batch of $0.2\,mm$ Herasil1 samples. The poling time and temperature are $t_p = 10\,min$ and $T = 280^oC$, respectively. The time-variable voltage is applied across two pressed-contact n-type silicon electrodes during poling. The second order susceptibility is evaluated by measuring $MF$ curves, as describe in Section 3.2.

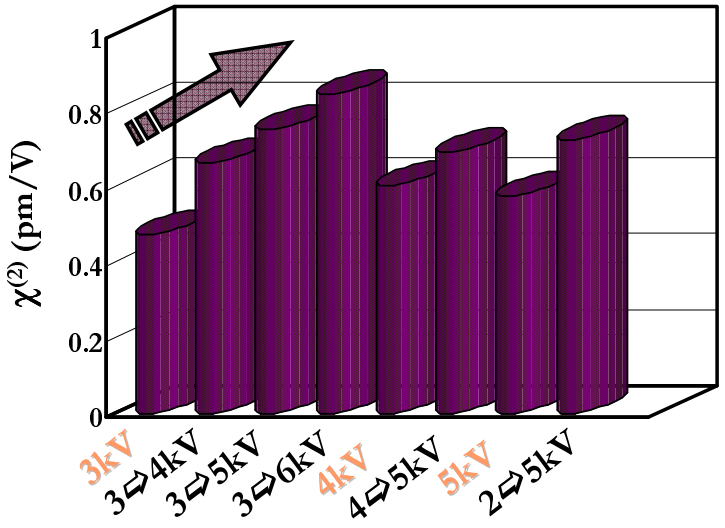


FIGURE 5.4: Voltage effect on $\chi^{(2)}$ peak value on $0.2\,mm$ thick Herasil1 samples

The peak $\chi^{(2)}$ values in depth are inferred by assuming a nonlinearity profile as retrieved with an inverse Fourier transform Maker Fringe technique (Ozcan et al., 2004a) and assuming a maximum nonlinear coefficient at about $1\,\mu m$ below the anode surface, then negligible in the bulk of the sample. If a constant-voltage is applied, the $\chi^{(2)}$ distribution versus voltage is consistent with results already published in the literature (Liu et al., 2000). However, when the cooling phase is 'assisted' with increased voltage, a linear trend of $SON$ with final voltage applied is shown. Furthermore, for identical $\Delta V = V_{cooling} - V_{initial}$, the nonlinear coefficient is influenced by which voltage value ($V_{initial}$) is kept applied during the first $t_p = 10\,min$ of poling. It is speculated that, under higher voltages, the interaction among much less mobile internal carries along with injected charge at the anode surface into the high field depleted region (see Section 2.3.2) may modify the charge distribution and lead to enhancement of the in-built electric field strength. As the dielectric breakdown point of the sample tends to increase inversely with temperature, the assisted-voltage treatment contributes to enhance the recorded electric field inside the nonlinear region during the cooling phase. To confirm it, experimental evidence of increased electric-field magnitude on variable-voltage poled samples is given in the next section. It is concluded that increasing voltage when the ion mobility decreases during cooling allows control of the space charge region evolution and thickness, which would eventually contribute to optimize the spatial overlap of second-order nonlinearity in waveguiding devices.

### 5.2.3 Electric field measurement: PEA and etching rate by interferometry

In Section 3.3 it is described how the power of the second harmonic wave generated within the poled sample is recorded as the nonlinear layer is simultaneously etched in hydrofluoric acid. The layer peeling method is integrated with interferometric measurement of the $HF$ etching rate, from which the built-in electric field distribution can be deduced (Margulis and Laurell, 1996). The authors demonstrated that the etching rate is related to the electric field through the following equation:

$$\rho(E_{DC}) = 2x\frac{exp(x)}{exp(x) - exp(-x)} \tag{5.2}$$

where $x = \alpha \cdot E_{DC}$ and $\alpha$ was estimated to be equal to $(1.26 \pm 0.05) \times 10^{-9} m/V$ in silica glass (Lesche et al., 1997).

The in-built electric field magnitude inside poled $0.2\,mm$ thick Herasil1 glasses is measured using the layer peeling apparatus in Figure 3.5. In particular, standard poling ($3\,kV$ and $5\,kV$ in *red* and *blue* squares, respectively) and time-varying voltage poling (depicted in *black* ($3 \Rightarrow 5\,kV$) and *green* triangles for $3 \Rightarrow 7\,kV$) are carried out, as described in Section 5.2.

Figure 5.5 presents a comparison between the resulting electric field distributions. The built-in electric field exhibits in all cases a slow and monotonic increase from the surface, tending to a plateau until the edge of the poled region is reached, where $E_{DC}$ then drops abruptly to zero. Its peak value, although close to the dielectric breakdown strength reported on silica glass (see Section 2.2), is increased by adjusting the $V_{cooling}$, for identical conditions at the start of the poling.

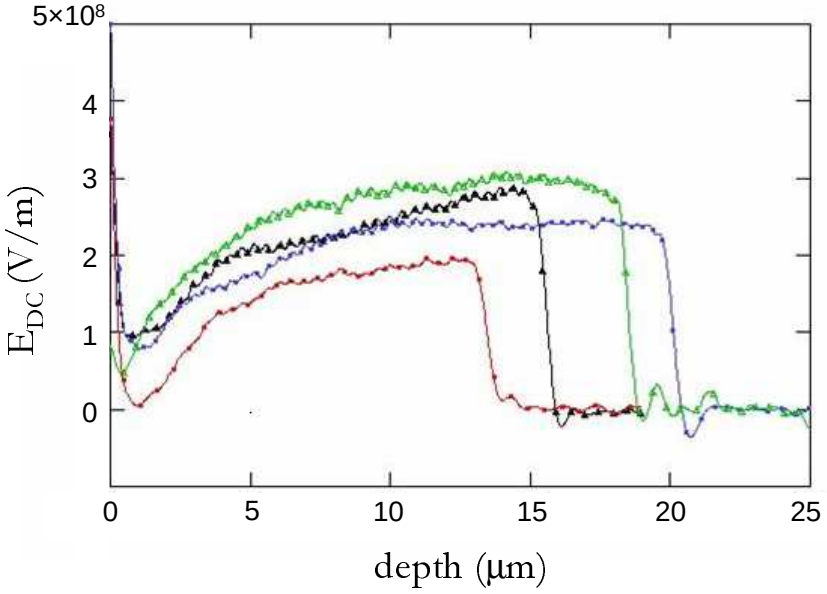


FIGURE 5.5: Anodic built-in electric field $E_{DC}$ distribution versus depth.

An $E_{DC}$ enhancement factor of more than 30% is estimated as a result of a $\Delta V = 2kV$ applied during cooling. The peak value of the electric field is almost doubled for $\Delta V = 4kV$, as revealed by the *red* and *green* curves in Figure 5.5. However, the detection system introduces irreversible damage at the surface due to chemical $HF$ etching and the poled region of the glass is peeled off along with the induced nonlinearity. The measurement can not be repeated on the same sample and a comparative study of the built-in electric field distribution is rather complex to obtain in this way.

The space-charge field strength can be deduced non destructively from measurement of the space-charge distribution using the Pulsed Electro Acoustic ($PEA$) technique. This methodology is typically used to study microstructural modifications in polymeric materials (Chen et al., 2004). Here, preliminary space-charge density measurements are successfully carried out for the first time on thermally poled $0.2\,mm$ Herasil1 samples.

A schematic of the experimental apparatus is illustrated in Figure 5.6. As a result of applying a high voltage electric pulse of ultrashort duration ($2\,ns$) to the poled sample, the space charge inside it is stimulated and experiences a pulse force that travels as an acoustic wave through the sample. By detecting the resultant pressure pulse arriving at a piezoelectric transducer in close contact with one of the electrodes, the space charge

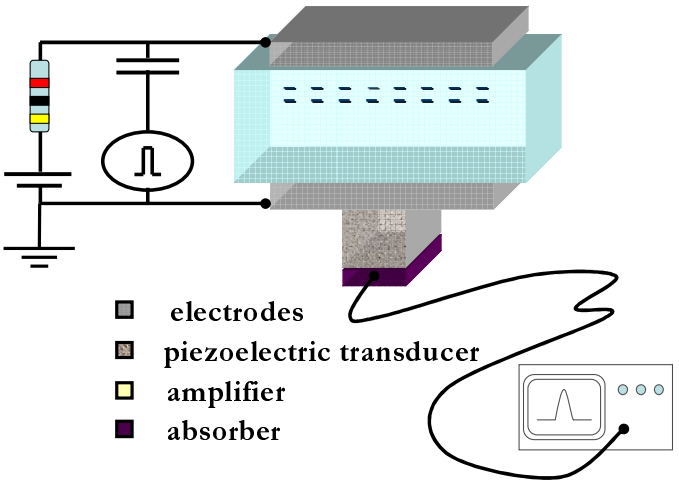


FIGURE 5.6: Pulsed Electro Acoustic ($PEA$) apparatus

distribution in the poled samples can be obtained from the evolution of the output voltage of the transducer itself. The sign of the $PEA$ signal is the same as the charge sign at the interface.

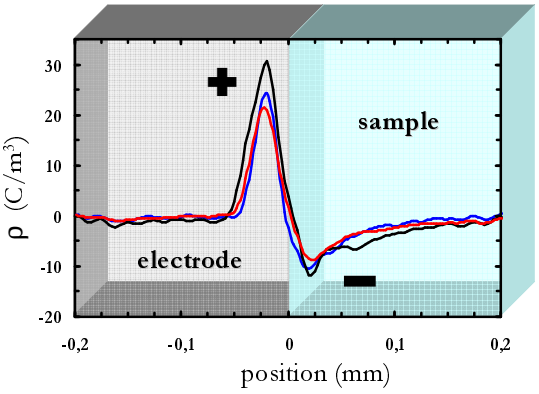


FIGURE 5.7: $PEA$ characteristic obtained recording space charge magnitude after poling under modified ($3 \Rightarrow 5\,kV$ in black) and standard procedure ($3\,kV$ and $5\,kV$ in red and blue, respectively)

Figure 5.7 presents the space-charge density as spatially monitored by the $PEA$ setup. The accumulation of the space-charge at the metal-oxide interface reflects the electric field strength $E_{DC}$ induced in three Herasil1 samples identically poled as in Figure 5.3. Based on comparative measurements, the enhancement of the $E_{DC}$ magnitude can thus be extracted. Overall, the space charge density in the variable-voltage poled sample displays an improved electric field strength of about 28% as a result of a $\Delta V = 2kV$ applied during cooling, which is in remarkable agreement with the results deduced above from interferometric measurement. Therefore, the Pulsed Electro Acoustic method reveals high potential of exploitation in the study of poling-induce space charge evolution,

although the spatial resolution of the present $PEA$ system is limited to about $10\,\mu m$ due to the speed of the acoustic wave in silica being equal to $5.95 \times 10^3 m/sec$. A faster detection system would improve its performance in poling-related applications, where the space-charge region requires resolution better than $1\,\mu m$.

In conclusion, the spatial distribution of the space-charge electric field induced within variable-voltage poled samples was investigated as a function of the final $\Delta V$. An $E_{DC}$ enhancement factor of about 30% is measured as a result of poling using time-varying voltage. The enhancement detected in the built-in electric field contributes to record more efficiently second order nonlinear coefficients. Finally, the ability to tailor the local distribution of $\chi^{(2)}$ creates a new viewpoint towards achieving efficient optical interactions in glass-based active structures such as planar waveguides and optical fibres.

### 5.2.4 Electro-optic coefficient measurement in fibre

In Section 5.2.1, it was shown that the application of a ramp voltage during the cooling stages of the thermal poling led to enhancement in the second harmonic power generated from bulk Herasil1 samples. Control of the depth evolution of the depletion region is also gained using such a variable-voltage poling technique and the frozen-in electric field has been measured to double in strength. These combined factors have allowed the generation of effective $SONs$ as high as $1\,pm/V$ (Figure 5.4). However, recent publications indicate that the average value of $SON$ is one order of magnitude lower for poled silicate twin-hole fibre (Michie et al., 2006). There, high values of $SON$ can not be consistently achieved as the electro-optic effect induced is affected by many factors, such as fibre geometry and core composition. In what follows, the first direct measurement of $SON$ enhancement as high as 75% over the standard procedure is shown by increasing the final voltage during thermal poling of twin-hole fibres (Canagasabey et al., 2006). This provides further evidence that this technique can be applied to a wide range of glasses and devices.

A preliminary study is carried out to experimentally determine the poling temperature required to induce optimal second order nonlinearity in the same devices that are described in Section 3.4.4. For this objective, a set of $13\,cm$ long twin-hole fibre devices are fabricated by A. Canagasabey from the ORC. The gold-coated tungsten electrodes ($\phi = 25\,\mu m$) are inserted as shown in the inset of Figure 5.8 and sealed into the side-polished entry holes using superglue, to prevent breakages from occurring. Subsequently, the devices are fusion spliced into one arm of an all-fibre Mach-Zehnder interferometer for the $in-situ$ measurement of the linear electro-optic ($LEO$) coefficient during thermal poling. The other arm of the interferometer is modulated using a piezo-electric stage operating at $20\,Hz$, as illustrated in Figure 5.8. Light from a diode laser of $3.8\,cm$ coherence length is split and recombined using two 2x2 couplers. A high frequency ($8.5\,kHz$) $AC$ test signal is applied through the electrodes along with the constant $DC$ voltage

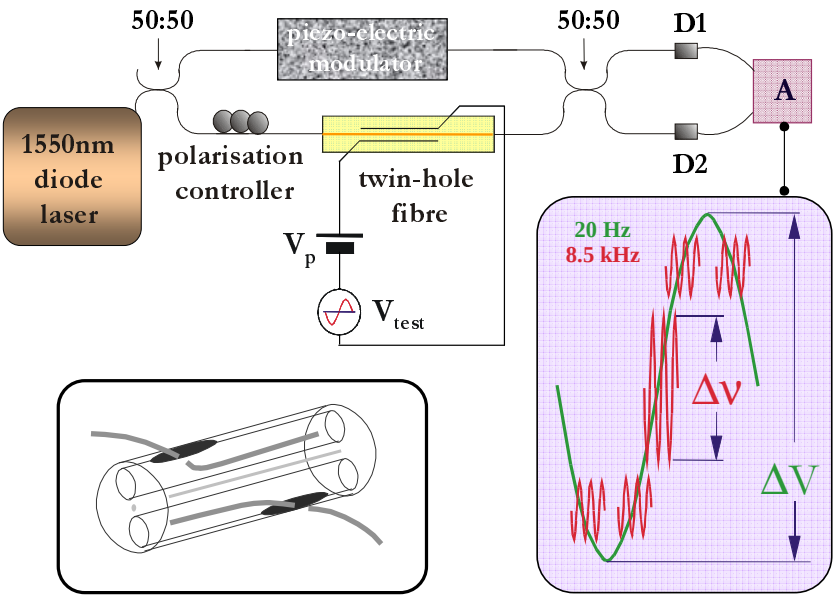


FIGURE 5.8: Online measurement of induced $\chi^{(2)}$ in fibres: apparatus. $V_p$: *DC* poling voltage. $V_{test}$: *AC* test voltage. *A*: differential amplifier. Also shown a typical output from the detectors (*D*). Inset: $125\,\mu m$ diameter twin-hole fibre with two $25\,\mu m$ electrodes inserted through side-polished slots.

($V_p = 3\,kV$) required for poling. Through a polarizer the desired polarization states into the twin-hole fibre is controlled to the direction parallel ($p$ - component input) or perpendicular ($s$ - component input) to that of the applied testing field. The interference fringes with highest contrast are achieved by balancing the intensity and matching the polarization states in both arms. *AC*-coupled detector can be used to measure the changes to fringe contrast. Before the application of the *DC* voltage and before any second order nonlinearity is induced in the fibre, only the fringes produced by the $20\,Hz$ modulation are detected. With the application of a *DC* field across the core of the fibre, the $8.5\,kHz$ amplitude ($\Delta\nu$), determined by the strength of the applied *DC* field across the core, grows with the poling time. The ratio between $\Delta\nu$ and the amplitude of the test signal ($\Delta V$) gives a measurement of the induced second order nonlinearity, according to:

$$\chi^{(2)} = \frac{n_c^4}{2} \cdot r = \frac{n_c \lambda d_{core}}{2\pi L V_{test}} \Delta\phi \tag{5.3}$$

where $n_c$ is the refractive index of the core; $L$ is the length of the wire overlap; $d_{core}$ the distance between the holes and $\Delta\phi = 2sin^{-1}(\Delta\nu/\Delta V)$ is the phase deviation in poled fibre.

The evolution of the electro-optic coefficient for devices poled at temperatures in the range 250-310$^oC$ while the applied voltage is constantly maintained at $3\,kV$, is shown in Figure 5.9.

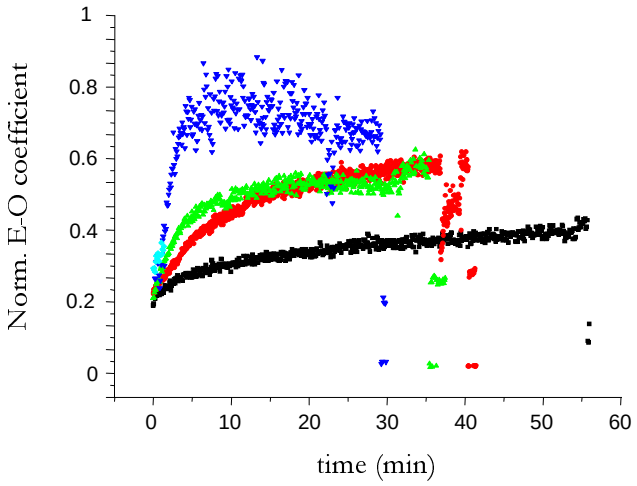


FIGURE 5.9: Electro-optic coefficient dynamics measured as a function of poling time at temperatures: $250^oC$ (black), $280^oC$ (red), $300^oC$ (green) and $310^oC$ (blue).

The characteristic growth profile is exhibited, which includes a rise of the electro-optic coefficient, a momentary drop, followed by an increase which usually levels off at some point. The evolution of the electro-optic effect indicates that the rate of growth is highly dependent on the poling temperature. However, at temperatures above $300^oC$, a steady drop in the electro-optic coefficient is evidenced, eventually leading to a $DC$ voltage breakdown through the core of the fibre. The drop in the electro-optic coefficient may indicate that the thickness of the nonlinear region does not increase with higher poling temperatures. At the optimized temperature of $290^oC$, the residual value of the electro-optic coefficient measured immediately after poling is $0.08 pm/V$, as shown in Figure 5.10 (black dots).

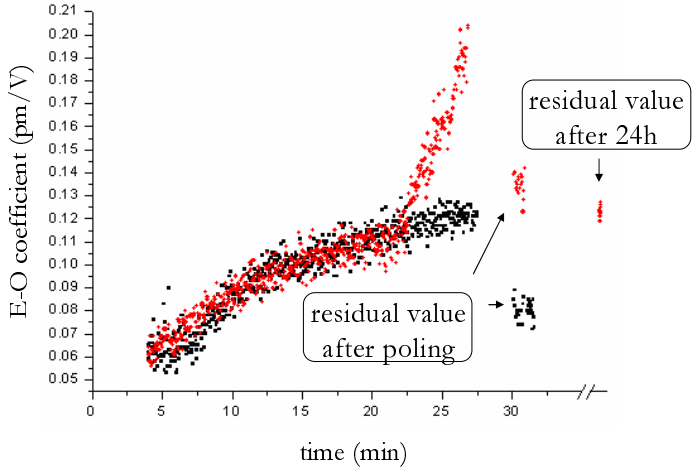


FIGURE 5.10: $EO$ coefficient evolution in thermally poled twin-hole fibres under standard (constant $3kV$ at $290^oC$, black dots) and modified procedure ($3 \Rightarrow 4.5\,kV$, in red). For the sake of clarity, the initial parts of the curves showing the first few minutes of poling have been omitted.

An increase of 75% in the induced electro-optic effect is experienced over the standard poling technique when an identical device is poled by variable-voltage cooling technique (see red curve in Figure 5.10). Initially set at $3\,kV$ for $t_p = 20\,mins$, the voltage is then raised to $3.5\,kV$ once the temperature is lowered at $265^oC$. The voltage is again increased to $4\,kV$ and finally to $4.5\,kV$ at $240^oC$ and $220^oC$, respectively. The average residual value of the $LEO$ coefficient measured immediately after poling is $0.14\,pm/V$. The residual value measured after 24 hours is slightly reduced ($r \approx 0.12\,pm/V$), as expected to occur in all poled devices.

The reported improvement in the second order susceptibility achieved by modifying the poling methodology during cooling is believed to be a result of the frozen-in field distribution after the treatment. Optimizing it would lead to the maximization of the interaction between the optical field of the light coupled in the core and the $DC$ electric field recorded through poling. Moreover, in the presence of higher voltage during cooling, an increased concentration of less mobile carriers might also widen the nonlinear layer, as detailed in bulk Herasil1 samples (Section 5.2.1). This could result in a more uniform distribution of charges in the region between the holes, and consequently a more uniform $SON$ in the core of the fibre.

In conclusion, variable-voltage cooling during poling of twin-hole fibres significantly enhances the second order nonlinearity compared to the standard poling procedure. Furthermore, this technique can lead to adjust the width of the nonlinear layer, which means that the positioning of the core of the fibre near the anode hole may no longer be critical. If the core is positioned equidistant from the two holes, the fibre fabrication process is simplified and the losses in the twin-hole fibre can be significantly improved.

## 5.3 Enhancing the induced $\chi^{(2)}$ in $Bi_2O_3$-based glasses

In the light of the experimental results reported in Section 5.2 on silicate glass, the methodology of increasing voltage during cooling is applied to pole $Bi_2O_3$-$ZnO$-$B_2O_3$ glasses.

To summarize the results on bismuth glasses so far, second-harmonic signals as high as in silica (reference being Herasil1 plate, poled at $280^oC$ and $4\,kV$ for $30\,min$) are generated in bismuth-borate samples within a near-surface layer at the anode side, as fully-detailed in Chapter 4. During poling, the measured current is even two orders of magnitude higher than silica and in most cases the nonlinearity is induced without current decay (Section 4.2.4). Nonetheless, the nonlinearity in $BZH\diamond$ glasses is alike revealed by etching to be within few microns underneath the anode surface. Efficient second-order nonlinearities are achieved only if poling at temperature a few degrees below the glass transition point. Slow heating and cooling phase are required to avoid breakage of the samples, which are affected by large thermal stress. For a given poling temperature and

voltage ($V_p = 4\,kV$), the *SHG* signal depends on $Bi_2O_3$ content, poling time and sample thickness. Furthermore, intimate contact is required at the glass-electrode interface in order to measure uniform *SHG* signal.

In this section, more investigations are carried out to achieve further improvement in poled bismuth-borate glasses. In particular, poling using time-varying voltage is employed for $BZH7$ glasses ($12.5\,mol\%\,Bi_2O_3$). An overview of the main achievements is given, along with some indications on how enhancing the induced $\chi^{(2)}$ in bismuthate glasses.

### 5.3.1 Results on $BZH7$ compounds

A preliminary study is conducted to establish the best conditions to generate second-order nonlinearity in poled $BZH7$ glasses. Systematic experiments are performed using pressed-on gold-on-silicon electrodes, since their contact with the glass polished face is crucially important during poling (Section 4.2.2). The poling time is set at $t_p = 5\,min$, which gives the highest *SHG* in Figure 4.6 for glass with 12.5% bismuth content. Samples with a thickness of $0.3\,mm$ are chosen for investigations (see Figure 4.15), still not too fragile to handle. The oven temperature is kept at $T_p = 290^oC$ during the poling time $t_p$, to perform the poling procedure in experimental conditions as close as possible to silica-based glasses. Within an ionic conducting glass, the major contribution to the increase of the electrical conduction is the increased mobility of each ion species when the temperature increases. As a result, the concentration of dissociated ions should not depend significantly on the temperature, which in turn may effect only the time constants of the phenomenon (Section 2.2).

During this initial investigation the key point to acquire insight in poling bismuth-borate glass materials is optimizing the process to guarantee a good degree of reproducibility. Therefore, the poling set up is customized to automatically monitor both the heating and the cooling rate. Samples are preserved from cracking at $T_p = 290^oC$, more likely to happen at heating conditions close to the $BZH7$ transition point ($T_g$=$470^oC$). Furthermore, accurate control of both voltage and current to the sample is provided throughout the poling process, thus avoiding current runaway and dielectric breakdown. The rate of increase at which the *DC* electric field is applied guarantees control on the field strength at which breakdown occurs. Setting the current limit of the *HV* source to a maximum value of $I_{LIM} = 100\,\mu A$ yields the poling current dynamics in Figure 5.11, whilst the voltage is varied in order to deliver a constant current during poling. Poling at constant current, instead of constant voltage, should not change the conduction behavior of the glass and the *DC* conductivity, $\sigma$, would be still given by Equation 4.3. Nonetheless, as a combined result of the formation of a more resistive depletion region and the temperature dependence of the resistivity in the sample during the first mins of cooling, the voltage tends to increase more and more, up to a final value which is set to

$V_{LIM} = 6.5\,kV$ on these glass compounds. A typical curve of the current and voltage evolution during a poling experiment is presented in Figure 5.11.

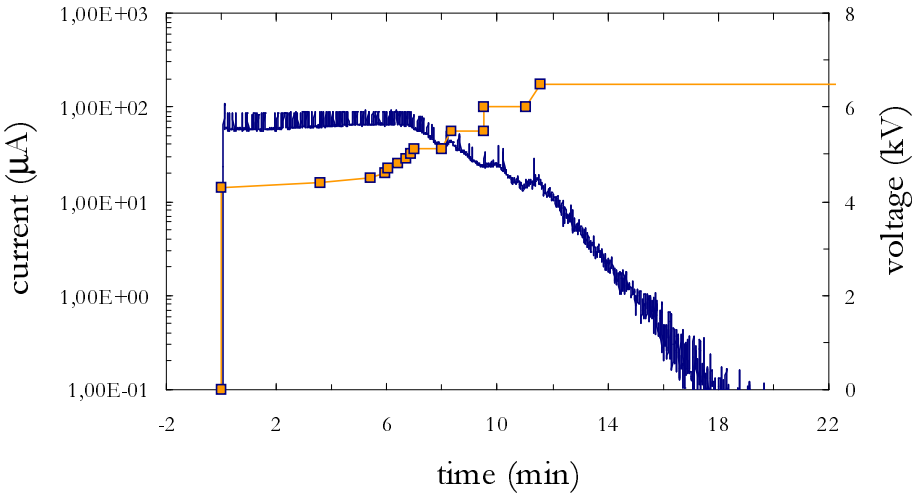


FIGURE 5.11: Evolution with time of current and voltage during poling $0.3\,mm$ thick $BZH7$ glass. Lines with square marks refer to the voltage axis.

In the next section, the best results achieved towards enhancing second order nonlinearities in $0.3\,mm$ thick $BZH7$ samples are overviewed. The variable-voltage procedure during cooling yields reproducibility along with signal uniformity across the poled area. However, more combinations of poling parameters are potentially suitable to optimize the entire process.

#### 5.3.1.1 The effect of sample thickness and melting point

In the light of the experience gained in Chapter 3, the layer peeling technique is considered at this stage as the best-suited characterization approach among those available to profile $\chi^{(2)}$. In Section 3.2 it is concluded that the Maker Fringe technique, although routinely used for the characterization of the induced nonlinearity on poled samples, does not carry any information on the $\chi^{(2)}$ profile of the poled samples. Reconstructing the second-order nonlinearity profile adds an extremely important piece of information towards engineering efficient glass-based active devices.

The layer peeling algorithm uses the second-harmonic signal generated within the first few microns from the anodic surface to determine the nonlinear distribution in poled samples. Therefore, to retrieve the $\chi^{(2)}$ profile on $BZH7$ glasses (melting point at $1000^oC$), the value of the $SHG$ signal is measured after successive etching in dilute nitric acid ($HNO_3$). To guarantee the reliability of the experiment, a customized set-up is implemented to etch the same region of the anode side of the sample each time. The $SHG$ signal is measured by mounting the sample on the Maker Fringe jig at a fixed angle.

The sample is then dismounted, etched in 0.2% $HNO_3$ solution for set time intervals, and finally inspected by $\alpha$-step profilometer to reveal the effective nonlinear depth.

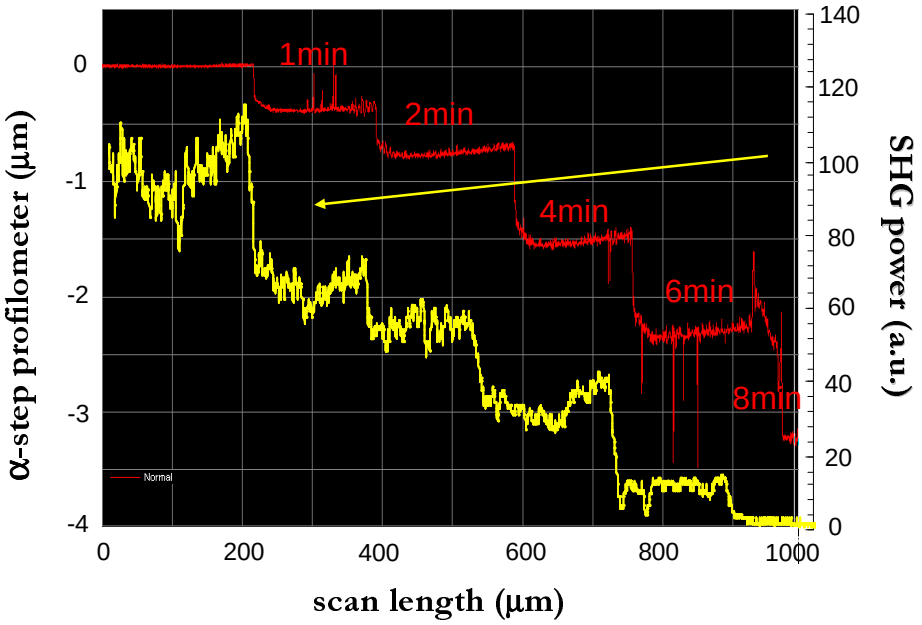


FIGURE 5.12: *SHG* decay as a function of different etching time: for the sake of clarity, red solid line on the graph shows the etching rate when scanning the profilometer across the poled region

Figure 5.12 displays the *SHG* signal decay for consecutive etching times; also shown is the removed nonlinear thickness at each step. The residual *SH* signal is then plotted as a function of depth. The experimental data (red circles in Figure 5.13) are best-fitted to the following theoretical function:

$$y = a \cdot (1 + e^{\frac{x-b}{c}})^{-4} \tag{5.4}$$

where $x$ is the depth across the sample; $a$, $b$ and $c$ are constants (Guignard et al., 2005).

By applying the layer peeling algorithm (Kudlinski et al., 2003a), the reconstructed nonlinear $\chi^{(2)}$ susceptibilities plotted as a function of depth are collected in Figure 5.13 for a full set of poled samples $BZH7$ with different thickness: $L = 0.2\,mm$ (1), $L = 0.3\,mm$ (2), $L = 0.5\,mm$ (3) and $L = 1.0\,mm$ (4), respectively. As can be observed, the profile of the second-order nonlinearity changes in accordance with the thickness, which reflects the specific dielectric response of the sample when identical poling condition are applied. Moreover, the peak $\chi^{(2)}$ increases from $(0.71 \pm 0.07)\,pm/V$ in $1.0\,mm$ case to $\chi^{(2)} = (0.85 \pm 0.09)\,pm/V$ in the thinnest sample, as predicted by the conductivity model described in Section 4.2.5.1.

The characterization of the $\chi^{(2)}$ profile versus the sample thickness adds crucial information towards understanding how to engineer efficient device designs and gives clear

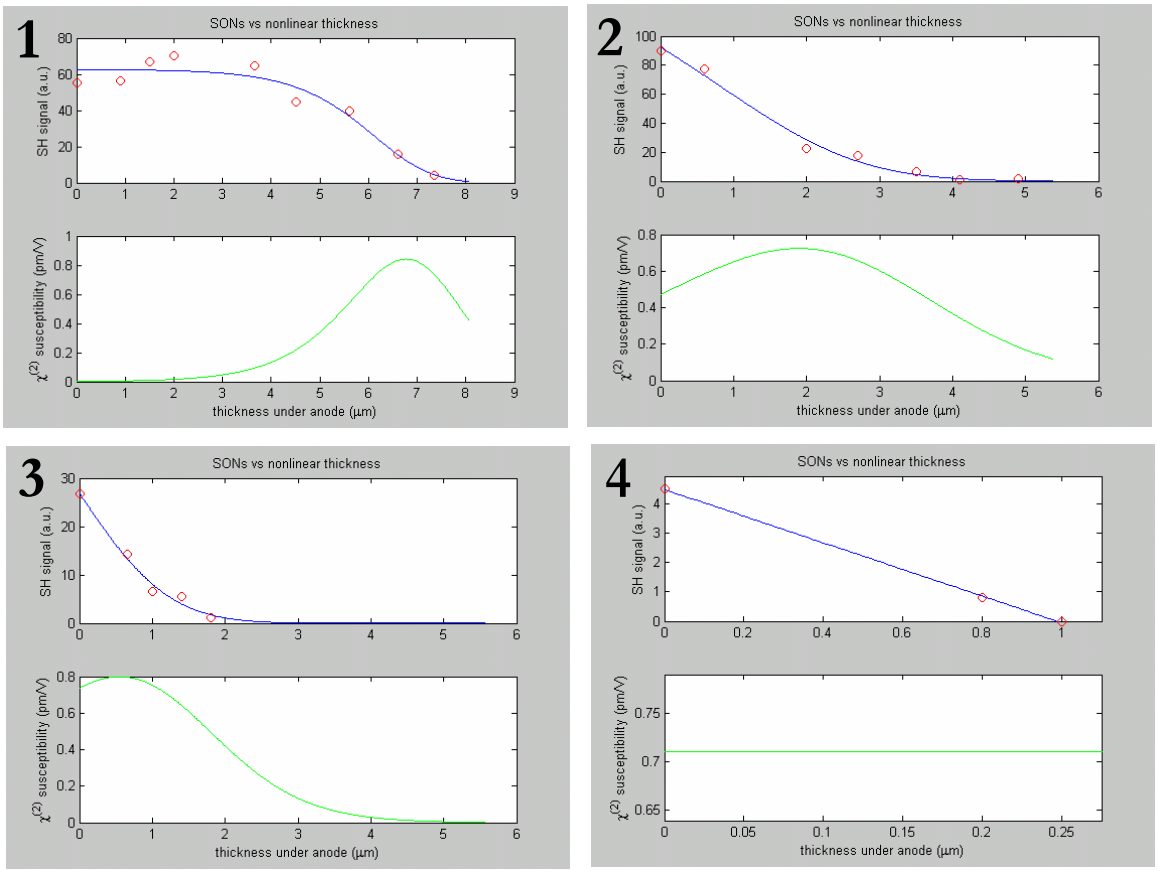


FIGURE 5.13: *SH* signal after successive etching of $BZH7$ for $L = 0.2\,mm$ (1), $L = 0.3\,mm$ (2), $L = 0.5\,mm$ (3) and $L = 1.0\,mm$ (4), respectively. The circles represent experimental data. The blue line represents the best theoretical function (Equation 5.4). Bottom: Reconstructed nonlinear $\chi^{(2)}$ susceptibility as a function of the depth under the anode.

indications that the $\beta$-value of $BZH7$ compounds is rather small (less than 10 in Figure 4.15), or in other words the electronic conductivity is not as low as desired. New $BZH7$ batches with lowered electronic conductivity must be investigated in order to enhance $\chi^{(2)}$. The poling induced electric field may be enhanced in the depletion region only when the electronic conductivity is lower than the ionic conductivity, as concluded in Section 4.2.5.1. Based on this hypothesis, the $NSG$ manufacturers fabricate a $BZH7$ samples with various melting points ($900^oC$, $950^oC$, $1000^oC$ (see Figure 5.13), $1100^oC$, respectively): lower electronic conductivities are expected in same glass compounds fabricated at lower melting temperature, as empirically discovered by Johnston (1965). To verify this assumption, $0.3\,mm$ thick $BZH7$ samples with different melting temperatures are poled under the same conditions described in Section 5.3.1.

The highest $\chi^{(2)}$ value is measured on the $BZH7$ glass having a melting point at $950^oC$. The relative reconstructed profile is displayed in Figure 5.14.

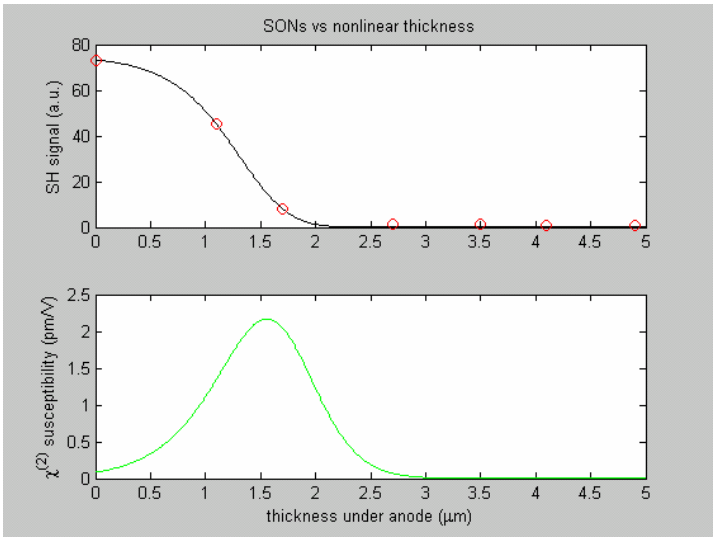


FIGURE 5.14: $SH$ signal after successive 0.2% $HNO_3$ etching of a $0.3\,mm$ thick $BZH7$ glass with melting point at $950^oC$. The circles represents experimental data. The black line represent the best theoretical function (Equation 5.4). Bottom: Reconstructed nonlinear $\chi^{(2)}$ susceptibility as a function of the depth under the anode: peak value $\chi^{(2)} = (2.3 \pm 0.2)pm/V$.

A peak $\chi^{(2)} = (2.3 \pm 0.2)pm/V$ value is estimated at about $1.5\,\mu m$ from the anodic surface. Samples having a melting point at $900^oC$ fail to validate the trend, likely due to imperfections in the glass matrix and/or macroscopic air bubbles introduced in the batch during the fabrication process, still to be optimized.

In conclusion, poling $BZH7$ by employing the variable-voltage procedure during cooling yields a reproducible second-order nonlinearity as high as $\chi^{(2)} = (2.3 \pm 0.2)pm/V$, which is very uniform across the anode region. Comparing these results with those described in Section 4.2.2, the technique with time-varying voltage succeeds in enhancing the poling induced second order nonlinearities of bismuth-borate glasses at temperature as low as $290^oC$ by adjusting the final voltage. Furthermore, accurate monitoring of current and voltage throughout the poling process avoids breakdown, thus preserving the glass quality after the treatment. In this direction, the availability of a full range of $BZH7$ glass samples with different melting point and consequently different electronic conductivities, has allowed the achievement of the highest value of $\chi^{(2)}$ reported on thermally poled bismuth-based glasses. Finally, along with the know-how acquired on poling $BZH7$ glass, the accurate reconstruction of the $\chi^{(2)}$ profile guarantees control on the nonlinear spatial distribution in specific guiding geometries. These achievements

make $BZH7$ compound a suitable material for the development of all-optical active devices based on poled $Bi_2O_3$-based glass.

#### 5.3.1.2 The effect of poling atmosphere: poling assisted deposition

Experimental evidence of an irreversible change in the chemical properties of bismuth-containing $BZH7$ glasses after poling is given in this section. Photographs of identically poled $BZH7$ samples in air (left hand side) and vacuum atmosphere (right hand side) are shown in Figure 5.15, respectively. The poling temperature is $300^oC$ and the applied voltage is $5\,kV$ for the first $15\,min$, and then increased up to $6.5\,kV$ during cooling.

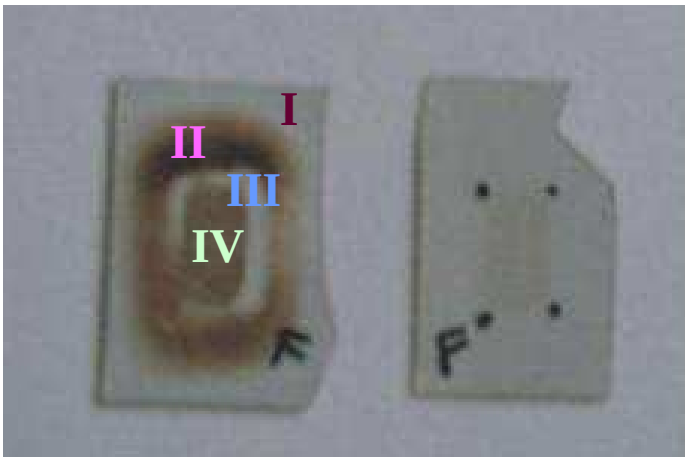


FIGURE 5.15: Evidence of precipitate on $BZH7$ samples poled in air (left hand side) and vacuum (right hand side), respectively.

The dark area (precipitate $IV$ in Figure 5.15) is confined within the electrode edges ($4 \times 7\,mm$) in both poled samples. However, its optical absorption is verified to increase with temperature and poling time after poling in air (Deparis et al., 2005b), whereas becomes weaker when poling is carried in vacuum. The precipitate spreads out of the poled region when the voltage is gradually increased in air during the cooling phase. Its distribution is not confined within the electrode edges as for poling in vacuum, and tends to assume a typical inner-ring shape (precipitate $II$ in Figure 5.15). No similar features are observed for constant $5\,kV$ applied during standard poling. Unexpectedly, detection of $SHG$ signal outside the electrode size is observed only where there is precipitate.

The formation of this permanent dark-colored area on poled $BZH7$ samples is in contrast with the fleeting character of the poling induced second-order optical nonlinearity, which is known to be erased by annealing at elevated temperature or UV-exposure treatment (Kameyama et al., 2001).

$XPS$ measurements performed at the $NSG$ labs evidence local nonuniformities in the atomic concentrations at the surface of the poled samples, as summarized in Table 5.1. The $Si\,(2p)$ atomic concentration is revealed to be about three times higher in the

| *zone* | $C\,(1s)$ | $O\,(1s)$ | $Zn\,(2p3)$ | $B\,(1s)$ | $Si\,(2p)$ | $Bi\,(4f5)$ |
|---|---|---|---|---|---|---|
| $I$ | 71.1 | 18.6 | 0.7 | 0.9 | 7.6 | 1.1 |
| $II$ | 45.8 | 33.8 | 0.7 | 0 | 19.6 | 0.1 |
| $III$ | 51.5 | 30.6 | 0.9 | 0 | 19.6 | 0.1 |
| $IV$ | 68.3 | 20.1 | 2.8 | 3.9 | 1.2 | 3.7 |

TABLE 5.1: Concentration of atoms at the surface in the regions highlighted in Figure 5.15. The above values are calculated from the $XPS$ signal counts with the assumption that the total concentrations of $C$, $O$, $Zn$, $B$, $Si$ and $Bi$ is 100%. For the sake of clarity, a relative comparison only is possible.

zones $II$ and $III$, all around the anode. Moreover, from the photo-electron spectra in Figure 5.16, the $O\,(1s)$ binding energy is measured to peak around $532\,eV$, which is comparable to non-bridging oxygen $Si-O^{-}$ values. By associating it with the oxygen-deficient form of silicon oxides ($SiO_{2-x}$), the variable-voltage poling procedure is believed responsible for silica film deposition on bismuth-borate glasses.

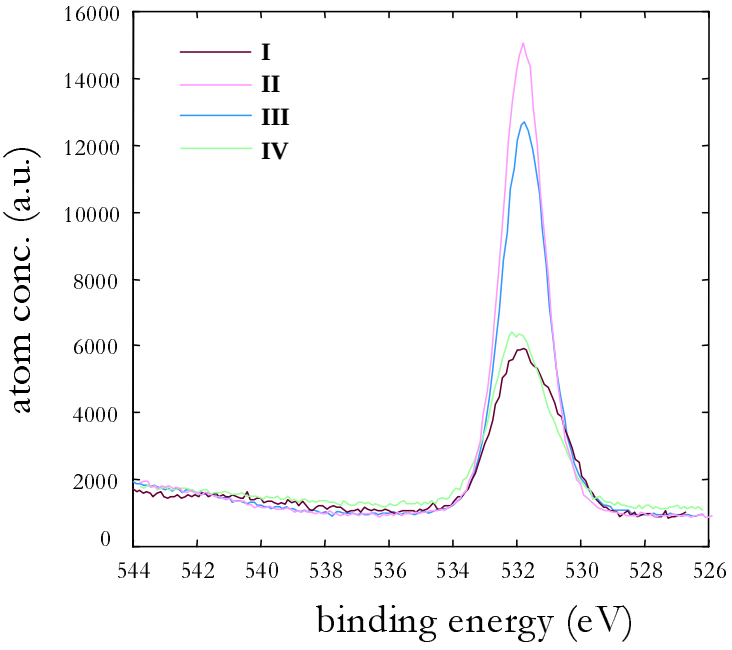


FIGURE 5.16: Photo-electron spectra for $O\,(1s)$

Figure 5.17 gives a schematic of how silica film deposition would modify the poled glass surface. During the cooling phase, increasing the voltage delivered to gold-on-silicon

electrodes may trigger reduction-oxidation chemical reactions at the glass-electrode interfaces (see Section 4.2.5). Thus, silica deposit would cover almost completely the glass surface, as darkened in the picture.

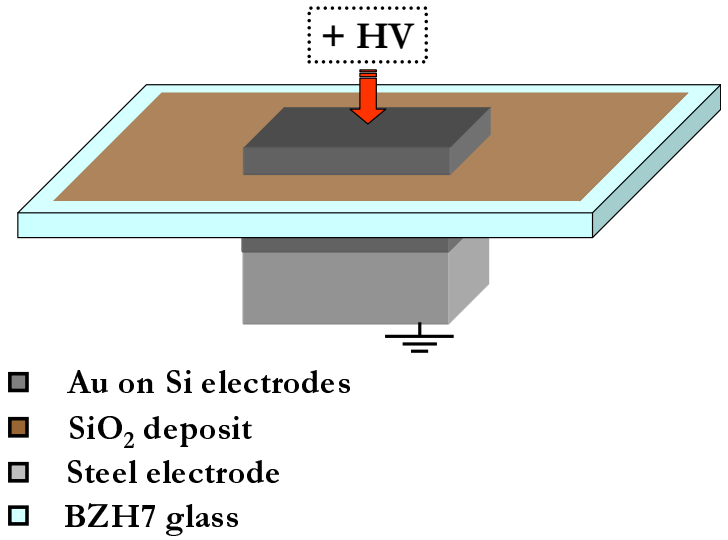


FIGURE 5.17: Schematic of the silica film deposition during poling of $BZH7$ glass.

The silica thin film as-deposited on the $BZH7$ surface prevents 0.2% $HNO_3$ etching to occur on a wide area around the anode, as experienced only after variable-voltage poling. In particular, highly diluted nitric acid etches virgin samples as well as both anodic and cathodic area 'protected' by the electrode during the poling treatment. On the contrary, the same etchant solution does not affect the highlighted area in Figure 5.17, but some small regions at the cathode side, very close to the electrode. This represents a clear evidence of silica deposition, poling induced by the time-varying voltage technique.

The creation of the dark precipitate could potentially be associated to sputtering or thermal deposition. The sputtering process takes place normally while the cathode is kept bombarded by heavy ions, whereas the silica deposition is revealed mainly at the anode side. On the other hand, thermal deposition begins at higher temperature than poling, depending on the material. Ono and Hirose (2004) reported field evaporation at around $300^oC$. Applying high voltage ($\cong 5\,kV$) to a sharp needle created extremely high field which drove the evaporation. Analogously, electric fields as high as air breakdown strength may be locally achieved here to deposit silica film during variable-voltage poling of bismuthate glasses.

In conclusion, a new deposition technique named 'Poling Assisted Deposition' is described. After specific poling treatments in air atmosphere, a $\approx 1\,\mu m$ thick silica film is detected for first time at the surface of poled bismuthate $BZH7$ glass. The investigation of the mechanism behind this unique way of depositing thin layers on glass surface is considered object for further research.

## 5.4 Conclusion

The establishment of the innovative variable-voltage poling technique is described in this chapter. A comparative study of variable-voltage and standard thermal poling is carried out in air on Herasil1 samples, Infrasil disks, twin-hole fibre and $BZH7$ compounds. In all cases, experimental evidence of in-built electric field strengthening is provided when the voltage is increased during cooling in comparison with the standard poling procedure, for identical conditions at the start of it. Furthermore, investigations on the spatially resolved evolution of the depletion region shows improved control on the space-charge distribution after poling. Thus, the second order susceptibility $\chi^{(2)}$ doubly benefits from increasing voltage when the ion mobility decreases during cooling, owing to the combined result of both reduced nonlinear depth and enhancement of the frozen-in electric field. A peak value of $\chi^{(2)} = 2.3\,pm/V$ is reproducibly recorded in $BZH7$ glasses, after adjustment of its electronic conductivity, which plays a role in preventing high values of the built-in electric field. The accurate knowledge of the $\chi^{(2)}$ profile will be exploited in the next chapter to tailor the integration of second-order nonlinearity in waveguiding regions.

Finally, a $\approx 1\,\mu m$ thick silica film is detected on bismuth-containing $BZH7$ glass surface after specific poling treatments in air. Experimental observations have been discussed. The investigation of the mechanism behind this unique way of depositing thin layers on glass surface is considered object for further research.

# Chapter 6

# Thermally poled waveguides in bismuth-based glasses

The results achieved so far on employing the variable-voltage procedure during cooling and accurately reconstructing the $\chi^{(2)}$ profile lead in this chapter to the development of active devices based on thermally poled $Bi_2O_3ZnOB_2O_3$ compounds.

Two device designs are investigated, an electro-optic ($EO$) modulator and a frequency converter, relying on two different technologies to fabricate waveguides on $BZH7$ glasses: sputtering and femtosecond laser direct writing, respectively. The demonstration of second-order nonlinearity induced by thermal poling in radio-frequency sputtered $BZH7$ glass film is given in Section 6.1.4. Efficiently poled channel waveguides written by tight focusing femtosecond laser pulses are reported in Section 6.2.1. New opportunities to realizing more complex on-chip structures towards enhancing the performance of integrated all-optical devices are also outlined.

## 6.1 Sputtered waveguiding geometries

In order to study how high electric fields may affect waveguiding structures, work on spatially resolved measurements of $SHG$ induced on poled slab waveguides is described in this section.

The optical guiding structures under examination are planar slabs of $BZH7$ glass sputtered on top of various substrates. Several parameters, such as substrate conductivity, surface morphology, refractive index, adhesion properties, have to be taken in account to succeed in poling those devices and to guarantee efficient second order nonlinearities and good guidance conditions. Menzel borosilicate glass slides ($n(@532\,nm) = 1.472$), $BZH6$, $BZH2$ and Herasil $He1$ ($n(@532\,nm) = 1.458$) samples of identical thickness and shape $(22{\times}22{\times}0.1)\,mm^3$ are used as substrates.

Thin films are prepared by radio-frequency magnetron sputter deposition of a $BZH7$ compound (melting point @ $1000^oC$) target $100\,mm$ in diameter and $5\,mm$ in thickness (as photographed in Figure 6.1).

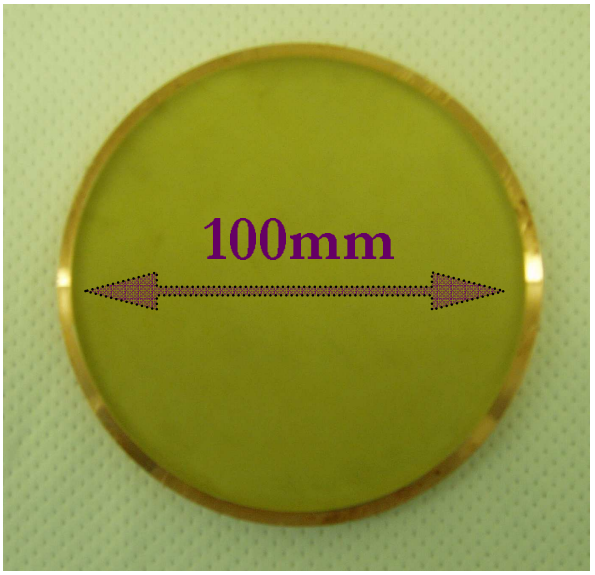


FIGURE 6.1: $BZH7$ target used for sputtering deposition. Diameter: $100\,mm$, thickness: $5\,mm$.

The sputtering chamber is evacuated to less than $20 \times 10^{-3}\,Torr$ prior to sputtering, and backfilled with the sputtering gas which consists of mixtures of argon and oxygen with a partial pressure ratio of $Ar/O_2 = 10/1$. The rf power is $100\,W$. Various sputtering times are tested with the substrate temperature kept constant during deposition at $293^oK$ ($20^oC$): in the hypothesis of linear behavior, a deposition rate has been estimated to be of the order of $500\,nm/hour$. The final thickness of the $BZH7$ guiding layers is chosen to be more than $2\,\mu m$, thick enough to support a guided mode at $\lambda = 1550\,nm$ for both polarizations. After sputtering, the waveguiding devices maintain their original transparency and show no surface damage under microscope inspection ($63\times, NA = 0.80$). In order to enhance their optical properties, the films are annealed after fabrication, keeping the samples at $180°C$ for 24 hours in a dry $O_2$ furnace ambient. Post-deposition oxygen annealing treatments are known to desorb the hydrocarbon contamination and reduce oxygen deficiency observed in $rf$ sputtered thin films (Atanassova et al., 2002). Annealing time and temperature are to be optimized, although the latter is intentionally kept below the $BZH7$ poling temperature adopted in Section 5.3.1.

The opto-electronic properties of such double-layer systems are characterized in the next sections. In particular, the thickness and refractive index of $BZH7$ thin films are measured by the prism coupling technique (Section 6.1.1) and the dielectric breakdown strength is estimated by high-frequency capacitance-voltage ($C-V$) and current-voltage ($I-V$) measurements (Section 6.1.2). Results on variable-voltage poling are finally

collected in Section 6.1.4 along with work towards integrating $SON$ in heterodyne (homodyne) Mach-Zehnder interferometer geometry (see Section 6.1.5).

### 6.1.1 Prism coupling measurements

Experimental work devoted to characterize the slab waveguides made by sputtering the $BZH7$ glass on top of borosilicate substrate is presented in these two subsections. The enhanced second-order nonlinearity in poled $BZH7$ material compared to silica would probably be compensated by poorer performance in terms of loss or maximum power sustainable. Coupling loss, propagation loss and damage threshold are parameters to take in account for fabricating competitive $Bi_2O_3$-based active devices.

Waveguides are characterized by prism coupling to determine thickness and refractive index of the $BZH7$ thin film. A schematic of the prism coupling setup is shown in Figure 6.2.

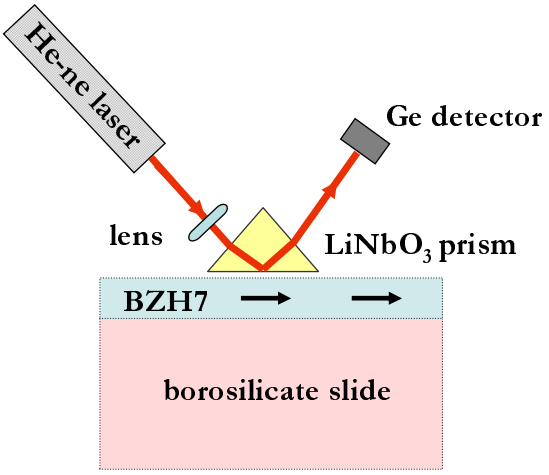


FIGURE 6.2: Prism coupling apparatus.

A He-Ne laser beam emitting at a wavelength of 632.8 $nm$ is coupled into the $BZH7$ layer using a lithium niobate prism ($LiNbO_3$) through the evanescent field in the air-film gap. The laser beam is linearly polarized ($TE$ or $TM$). A lens focuses the beam into the prism so that the beam waist coincides with the prism base. The point where the beam strikes the prism base is the coupling spot. At this point, the film thickness and refractive index are being measured. Set the substrate refractive index at $n = 1.472$ and the prism $n(@632.8\,nm) = 1.9648$, the sputtered film thickness is calculated to be $(1.1702 \pm 0.0002)\,\mu m$, in accordance with $SEM$ observations. Using the calculation procedure reported by Ulrich and Torge (1973), the ordinary refractive index for $TM$ polarization is determined as $1.7482 \pm 0.004$ and the extraordinary index for $TE$ polarization is $1.7459 \pm 0.006$, in excellent agreement with the value in Table 4.2 as inferred by optical transmission spectra.

By measuring the reflected intensity versus the angle of incidence, the guided-mode spectrum of the samples can be drawn. With the optical axis normal to the surface, the ordinary and extraordinary modes are respectively excited using transverse electric ($TE$) and transverse magnetic ($TM$) polarized light. In Figure 6.3, the $TE$ coupling curve of the laser beam into $BZH7$ film is plotted. The $TE$ mode spectrum shows one sharp reflectivity dip at the scanning angle which correspond to the excitation of guided mode . These can be identified as the fundamental mode $TE_o$.

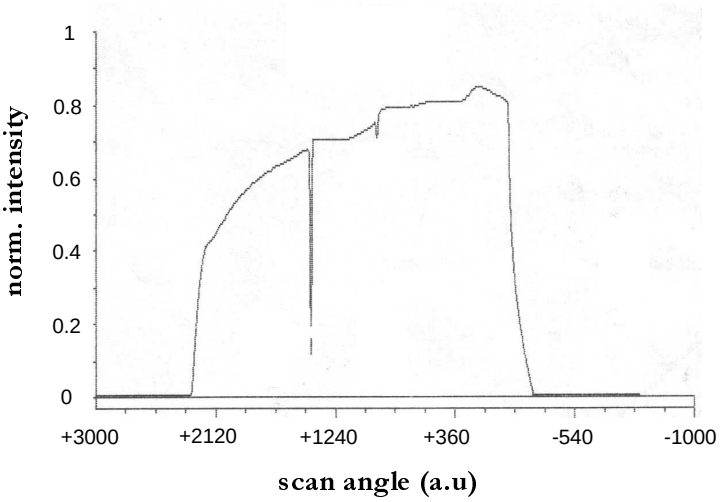


FIGURE 6.3: $TE$ mode spectrum of $BZH7$ sputtered film.

Likewise, the slab waveguide is measured to be both $TE$ and $TM$ mono-mode guiding at $632.8nm$. Finally, propagation loss measurements are performed by scanning a wide face detector across the sample surface to collect scattered radiation. Figure 6.4 shows the measured signal as a function of the position on the surface.

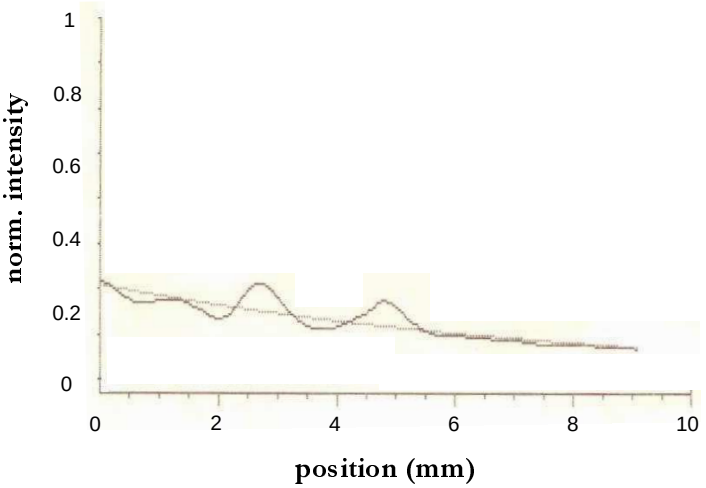


FIGURE 6.4: Intensity ($I$) as a function of the position, $x$, on the sample surface. The best-fit curve is: $ln(I) = 4.706 - 1.154x$.

The estimated loss of $5.01\,dB/cm$ is inferred from the intensity decay *vs* distance, best-fitted by an exponential curve ($\chi^2 = 0.784$). In order to achieve good guidance, this value is aimed to be reduced by optimizing both the sputtering and the post-deposition annealing process.

### 6.1.2 $C-V$ and $I-V$ measurement

Both capacitance-voltage ($C-V$) and current-voltage ($I-V$) high-frequency ($1MHz$) measurements were performed on the $MOS$ structure shown in Figure 6.5, where a $BZH7$ film is sandwiched between aluminum electrodes and a silicon wafer.

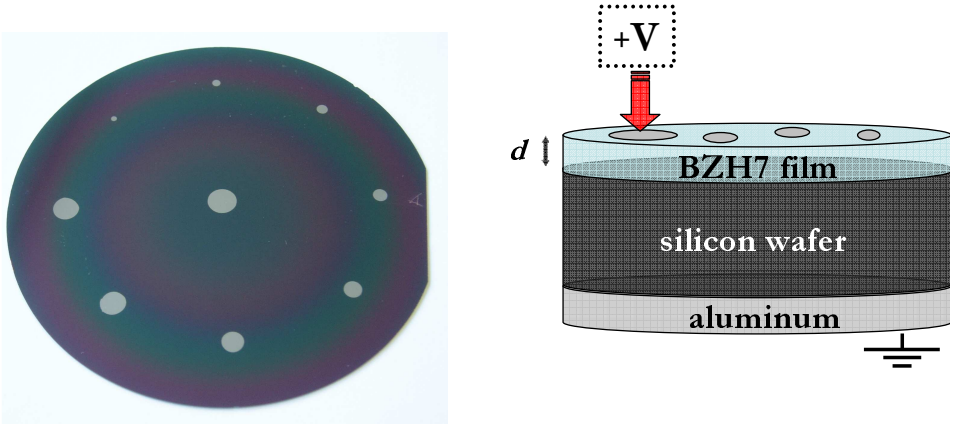


FIGURE 6.5: Top-view of a 3′ n-doped silicon. The cross section of the device is shown, where $d$ is the thickness of the $BZH7$ glass and $V$ is the applied field.

Circular aluminum electrodes of various diameters are evaporated on top of a $d = 1.01\,\mu m$ thick $BZH7$ layer sputtered on a n-doped silicon wafer ($\phi = 3$ inches). The silicon wafer is carefully washed in $HF$ and ammonium fluoride bath before the glass deposition to reduce the interface-trapped charge density. The bottom metalization of the silicon wafer (aluminum in Figure 6.5) is intended to prevent its surface oxidation and guarantee good ohmic contact.

Given the $BZH7$ glass thickness, a dielectric constant $\epsilon_r \cong 6.22$ can be estimated in $BZH7$ glasses ($12.5\,mol\%\,Bi_2O_3$) by:

$$C = \frac{\epsilon_o \epsilon_r \cdot A}{d} \tag{6.1}$$

where the free-space permittivity $\epsilon_o = 8.85 \times 10^{-12}\,F/m$ and the electrode area ($A$) is incrementally varying ($\phi = 1-5\,mm$ by steps of $0.5\,mm$ in Figure 6.5) in order to allow capacitance ($C$) measurements within the instrument detectable range ($100-1500\,pF$). The measured $BZH7$ permittivity is significantly higher than silica ($\epsilon_r^{SiO_2} = 3.9$), which

would imply a lower voltage drop across the sample, according to the conductivity model in Section 4.2.5.1.

Information on the dielectric breakdown strength can be deduced from the current-voltage ($I-V$) measurements. The thickness of the bismuth glass layer is set to be $d = 48 \pm 2\,nm$, and comparative tests are performed on circular electrode with diameter varying by steps of $0.1\,mm$ between $1\,mm$ and $1.5\,mm$, respectively. Occurrence of soft breakdown breaks the linearity of the $I-V$ curve at $(29 \pm 1)\,V$, as shown in Figure 6.6 for $1.2\,mm$ diameter electrodes.

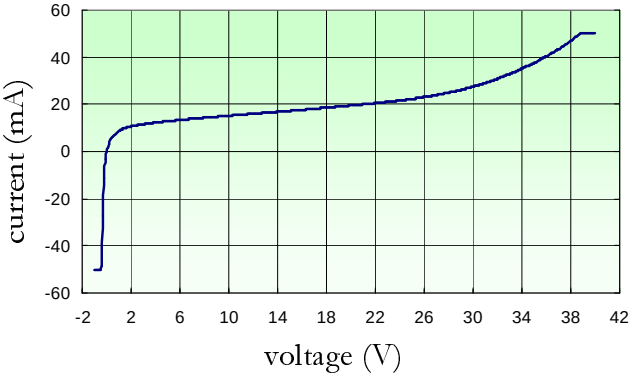


FIGURE 6.6: Soft-breakdown breaks the linearity of the $I-V$ curve at around $30\,V$.

Its threshold can be estimated to be around $6 \times 10^8\,V/m$ at lab temperature ($25^oC$), more than three times lower than the dielectric breakdown strength of silica (see Section 2.2).

More experiments are required to establish how the soft breakdown threshold may be influenced by temperatures in the range used for poling. Moreover, it is crucial to investigate the effect of different bismuth-oxide content ($BZH2$, $BZH4$, etc.) upon the dielectric breakdown strength to determine whether there is an intrinsic limitation in achieving frozen-in electric field as high as in silica during poling of $BZH\diamond$ glass compounds.

In conclusion, monomode $BZH7$ slab waveguides have been realized by sputtering technique and their optoelectronic properties have been characterized. Waveguiding structure designs must be investigated in order to realize competitive active devices based on thermally poled bismuth-based glasses. In the next section, a speculative approach is provided towards enhancing the poling efficiency in highly conductive $Bi_2O_3$-based guiding layer, taking into account that their dielectric breakdown strengths is few times lower than silica-based glasses.

### 6.1.3 Conductivity model for two-layer bismuth glass structures

The model proposed in Section 4.2.5.1 to describe the electronic response of highly conductive glass during poling is now extended to evaluate the inducible second-order

nonlinearity when a multilayer device is realized. The theoretical approach aims to allow the design of a glass structure suitable for poling, by assembling materials with different ionic and electronic conductivities. In particular, the conductivity of the glass is believed to inhibit the voltage drop across the depletion layer, prohibiting large $\chi^{(2)}$ values.

The scheme of the double-glass structure being studied after thermal poling is shown on the right hand side in Figure 6.7. The $BZH7$ layer is in contact with the anode, through which the external field is applied: if its conductivity is lower than the substrate, the depletion layer and bulk may be localized as sketched on the right hand side in Figure 6.7.

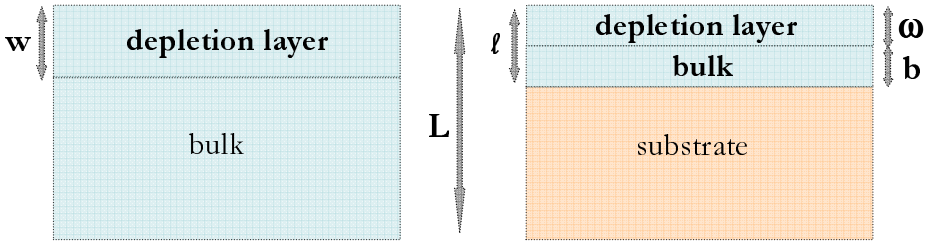


FIGURE 6.7: Schematic of different glass structure after poling (not in scale). Left: cross-section of a single-glass device. Right: cross-section of a two-glasses device. The $BZH7$ layer is deposited on top of a substrate glass.

In the hypothesis of electronic conductivities of bulk and depletion layer being equivalent in the $BZH7$ layer (i.e. $\sigma_{eb} = \sigma_{ed}$), the expected $\chi^{(2)}$ as a function of $\beta$ in both single and two-glasses devices is compared in Figure 6.8.

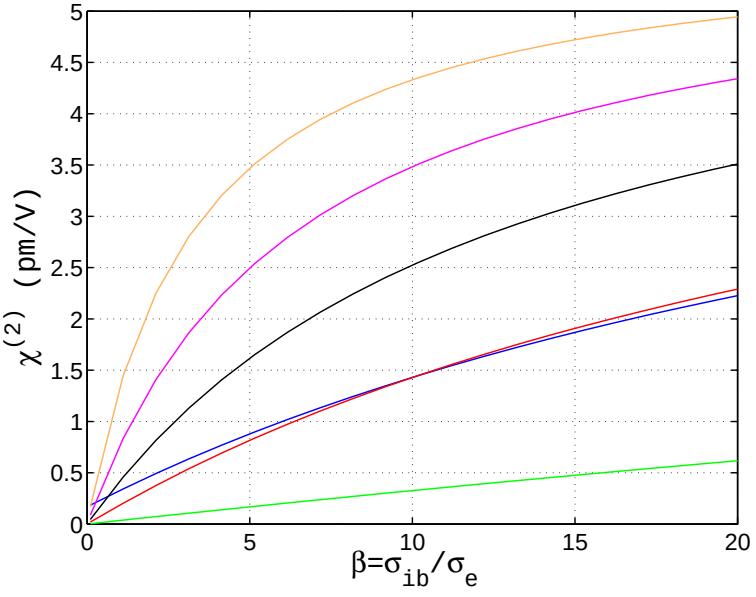


FIGURE 6.8: Extension of the conductivity model (Section 4.2.5.1). The predicted second-order nonlinearity as a function of $\beta$ for a single (*blue*) and double-layer structure, when the substrate ionic conductivity $\sigma_{is} = 10^{-1} \times \sigma_{ib}$ (*green*), $\sigma_{is} = \sigma_{ib}$ (*red*), $\sigma_{is} = 2 \times \sigma_{ib}$ (*black*), $\sigma_{is} = 5 \times \sigma_{ib}$ (*pink*), $\sigma_{is} = 10 \times \sigma_{ib}$ (*orange*), respectively. The substrate electronic conductivity $\sigma_{es}$ is set equal to $\sigma_{ib}$.

The *blue* curve reproduces results as in Figure 4.15 for a $L = 0.103\,mm$ thick $BZH7$ compound, where the nonlinear thickness is $w = 3\,\mu m$ in Equation 4.6 and the dielectric breakdown strength is set according to the outcomes in Section 6.1.2. In the double-layer structure, the thickness of the $BZH7$ layer on top is $l = \omega + b = 3\,\mu m$ and the predicted second-order nonlinearity is plotted as a function of:

$$\beta = \frac{\sigma_{ib}}{\sigma_e} \tag{6.2}$$

where $\sigma_{ib}$ and $\sigma_e$ are defined as the bulk ionic conductivity and electronic conductivity of the upper $BZH7$ glass layer. The substrate electronic conductivity $\sigma_{es}$ is here set equal to $\sigma_{ib}$, whereas the substrate ionic conductivity $\sigma_{is} = 10^{-1} \times \sigma_{ib}$ $(green)$, $\sigma_{is} = \sigma_{ib}$ $(red)$, $\sigma_{is} = 2 \times \sigma_{ib}$ $(black)$, $\sigma_{is} = 5 \times \sigma_{ib}$ $(pink)$, $\sigma_{is} = 10 \times \sigma_{ib}$ $(orange)$, respectively.

In order to pole the double-layer system more efficiently, the substrate material has to possess higher conductivity than the $BZH7$ thin film, in accordance with Figure 4.14. In this case, the external voltage applied during poling is expected to drop only across the depletion region in the upper layer ($BZH7$ glass). Moreover, by extrapolating the $\beta$ value from the experimental $\chi^{(2)} = (0.85 \pm 0.09)\,pm/V$ measured on poled $0.2\,mm$ thick $BZH7$ bulk samples, having melting point at $1000^oC$ (see Section 5.3.1.1), the second order generated signal increases with the ratio $\sigma_{is}/\sigma_{ib}$ and a $\chi^{(2)}$ value of $3.5\,pm/V$ may be predicted in the double-layer device, provided that the substrate material exhibits a 10 times higher conductivity than the waveguiding $Bi_2O_3$-based layer.

As a conclusion, the theoretical approach employed to describe the role played by conductivity during poling of bismuth-based glass considers the effect of the electronic conductivity in preventing high built-in electric field after poling. An extension of the bulk glass model has been implemented to investigate a double-layer structure. The results show that a low resistivity substrate should be used in waveguide structure to be poled.

### 6.1.4 Poling slab

In this section, the variable-voltage technique is employed to induce second-order nonlinearity in poled sputtered thin waveguiding films. The guiding structure to be poled consists of planar slab of $BZH7$ glass identically deposited on top of various types of substrate. Menzel borosilicate slides ($n(@532\,nm) = 1.472$), $BZH6$, $BZH2$ and Herasil $He1$ ($n(@532\,nm) = 1.458$) samples of identical thickness and shape $(22\times22\times0.1)\,mm^3$ are used as substrate. The film thickness is chosen equal to $3\,\mu m$ as for the simulation in Figure 6.8. In all case, constant-current poling at $I_{LIM} = 100\,\mu A$ is performed for 5 minutes in air atmosphere at $290^oC$, followed by cooling phase, during which the voltage is increasingly delivered to Au on silicon electrodes ($6 \times 9mm$), up to $2.5\,kV$. The poling

conditions dramatically differ from the $BZH7$ bulk case (Section 5.3), and depend on the substrate conductivity, as expected.

After poling, the $BZH7$ thin film is irreversibly damaged under the electrodes with $BZH6$ and $BZH2$ substrates and no $SHG$ signal can be detected. Lack of adhesion at the interface film-substrate is shown by microscope inspection. The poling treatment is instead successful on thin $BZH7$ film sputtered on borosilicate, $Bor(BZH7)$, and Herasil substrates, $He1(BZH7)$. The homogeneity of the nonlinearity across the electrode area is measured by scanning the focused fundamental beam across the sample for a fixed incident angle on the apparatus in Figure 3.1. The as-recorded variations in the $SH$ signal are shown in Figure 6.9.

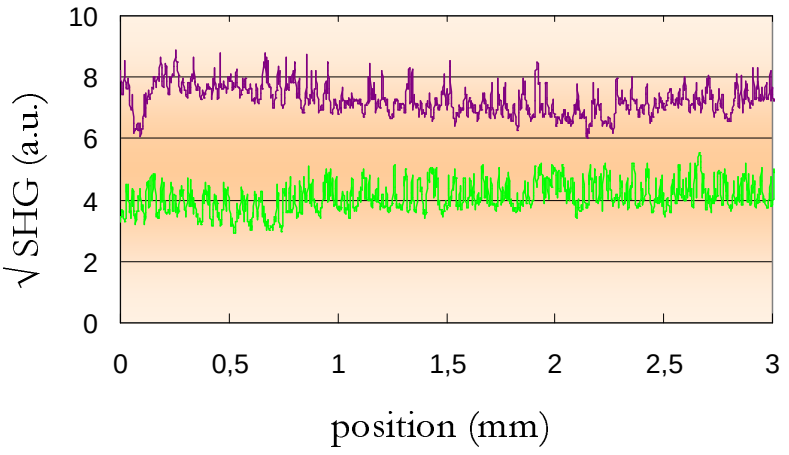


FIGURE 6.9: Square root of the $SHG$ signal as a function of the position under the anodic electrode after poling: $He1(BZH7)$( green), $Bor(BZH7)$ (violet).

The square root of the generated $SH$ signal for the slab $Bi_2O_3$-based waveguide with borosilicate substrate (*violet* in Figure 6.9) is 7.25, almost twice the value measured on the $He1$ substrate (*green* curve), which is about 4. The measured $SHG$ signal is uniformly distributed under the electrodes as expected (Section 5.3.1), which is a great advantage in waveguide applications. Both the substrate materials present lower refractive index than $BZH7$, thus fulfilling the guiding conditions.

To quantify the genuine nonlinear contribution coming from the thin bismuthate film only, the $SHG$ signal is measured after etching off the $BZH7$ thin layer by highly diluted (0.2 %) $HNO_3$. The Herasil glass itself exhibits a residual $SHG$ signal after etching the $BZH7$ glass, probably owing to its resistivity and ions mobility during poling. No second order nonlinearity can be measured from the borosilicate substrate.

To check the reliability of this poling process, high quality films deposited by sputtering $BZH7$ on borosilicate slides are identically poled and the induced $SHG$ signal tested after successive 0.2 % $HNO_3$ etching. Figure 6.10 shows the measured $SH$ signal as a

function of the removed thickness of the poled region. Also shown is the reconstructed nonlinear susceptibility profile: a maximum value of $\chi^{(2)}$=$(2.0 \pm 0.2)pm/V$ is recorded.

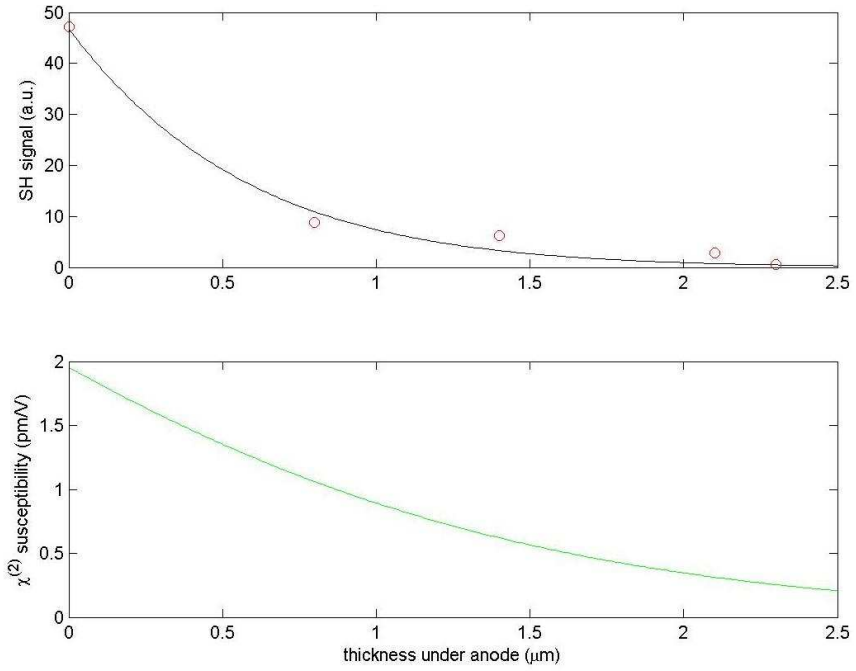


FIGURE 6.10: Top: $SH$ signal after successive 0.2 % $HNO_3$ etching of $BZH7$(1000) waveguide on top of borosilicate substrate. The red circles represents experimental data. The black line represents the best theoretical function. Bottom: Reconstructed nonlinear susceptibility as a function of the depth under the anode.

To summarize, $3\,\mu m$ thick slab waveguides obtained by sputtering $BZH7$ glass on a borosilicate substrate are successfully poled. A peak of second-order nonlinearity as high as $2.0\,pm/V$ is recorded by adjusting the poling voltage during the cooling phase. The $\chi^{(2)}$ profile reconstruction after thermal poling shows that the nonlinear region is localized in the waveguiding layer, thus allowing to optimize its spatial location where the higher refractive index maximizes the third order nonlinearity. This result represents a turning point towards the development of active devices based on poled bismuth-borate channel waveguide. In the next section, the first evidence of guidance is reported in a rib waveguide out of a sputtered $3\,\mu m$ thick slab.

### 6.1.5 *EO* modulator: strip-loaded and rib waveguides geometry

The following section reports on the achievements towards developing an integrated-optical Mach-Zehnder modulator. The device based on the linear electro-optic effect is designed to integrate poling-induced second order nonlinearity (Section 6.1.4) in a sputtered waveguiding geometry.

The design of a strip-loaded Mach-Zehnder interferometer with high-index poled $Bi_2O_3$-based glasses is shown in Figure 6.11.

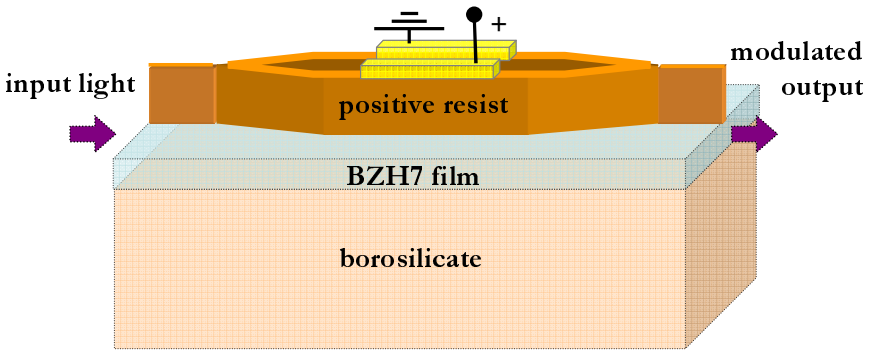


FIGURE 6.11: Mach-Zehnder intensity modulator in form of an integrated optical device

The strip-loaded technology allows flexibility in defining waveguides by etching only the over-cladding layer (in this case, positive photoresist), which in turn isolates the guiding region from the electrodes. Most importantly the guiding layer is not etched, eliminating sidewall roughness and reducing scattering losses; furthermore, few photolithographic steps are required, which lowers the risk of '$\chi^{(2)}$ degradation' during the fabrication process.

Beam propagation software is used to design strip-loaded waveguides. Given a Gaussian input wave field and known refractive index profile, the propagation modes through the Mach-Zehnder interferometer are simulated. It is shown that the waveguide geometry has to be adjusted to confine the mode profile: in particular, the plots in Figure 6.12 are relative to a $BZH7$ guiding layer $3\,\mu m$ thick, when the distance between the arms of the $MZI$ is $20\,\mu m$ and the entire length is $15\,mm$.

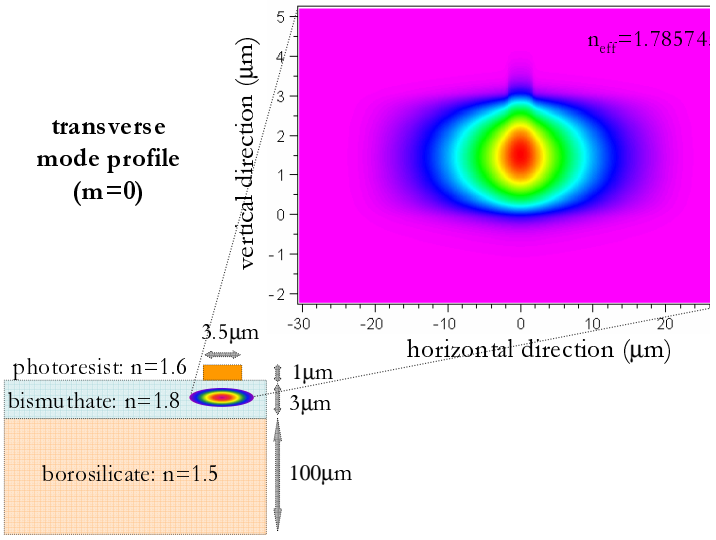


FIGURE 6.12: Waveguiding geometry cross section and simulated transverse mode profile (inset) for the Mach-Zehnder interferometer based on the strip-loaded geometry.

The interferometer structure is defined by a standard photolithography process on a thin layer of negative resist developed on top of sputtered bismuthate film. Then, the electrode pattern is transferred by depositing aluminum first, covering it with positive photoresist and finally etching off the unexposed region by ion milling technique. However, the use of the dry etching unexpectedly leads to loss of definition of the electrode shape, mainly due to aluminum adhesion to the sputtered bismuthate slab. The metal adhesion to $BZH7$ glasses depends on the affinity metal/oxygen and it is related to the reduction potential ($E_o$) of the metal itself. Among the metals listed in Table 6.1, gold would give the poorest adhesion to the glass.

| *metal* | $E_o$ $(V)$ |
|---|---|
| $Al$ | $-1.662$ |
| $Ti$ | $-1.630$ |
| $Cr$ | $-0.744$ |
| $Ni$ | $-0.257$ |
| $Cu$ | $+0.342$ |
| $Au$ | $+1.498$ |

TABLE 6.1: Reduction potentials for glass-metal adhesion.

New electrode materials are to be tested and more experimental investigation are required to optimizing both mask design and fabrication steps.

In parallel to this approach, a different technology is under investigation aiming to fabricate a Mach-Zehnder interferometer based on rib waveguides. Photolithography and ion milling etching process are employed to define rib waveguides out of a $3\,\mu m$ thick $BZH7$ slab on top of a $100\,\mu m$ thick borosilicate slide (lower cladding). The $SEM$ image in Figure 6.13 shows in details the polished end-face of the rib geometry, whose roughness is inspected in the inset and might cause losses in light propagation through the guiding layer.

The first demonstration of mode profile measurements is reported from a Mach-Zehnder interferometer based on rib waveguide geometry. A $632.8\,nm$ single mode $TM$ polarized beam is coupled by a $25\times$ microscope objective into the polished facade of the input waveguide. The outlet coupling (a $16\times$ microscope objective and a progressive filter) focuses onto a $CCD$ camera, as in Figure 6.14.

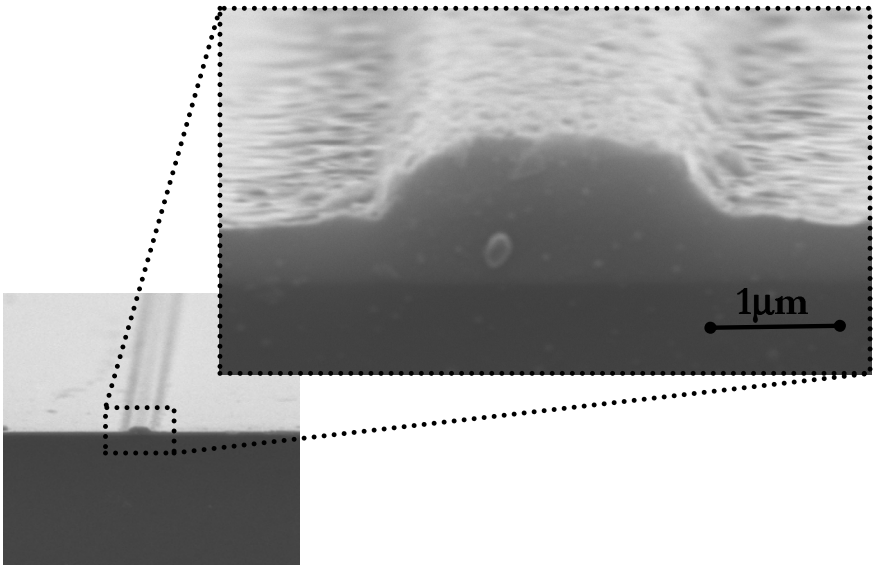


FIGURE 6.13: *SEM* image of the polished end-face of a 100 $\mu m$ thick borosilicate slide (lower cladding) with etched rib waveguide on top (highlighted in the inset)

FIGURE 6.14: Mode intensity profile from sputtered thin film bismuth-based rib waveguides.

The top view of three out of six $MZI$ devices built on a $(22\times22\times0.1)\,mm^3$ borosilicate slide is photographed below (Figure 6.15). The aim of this experimental work is to guarantee comparison and confirm reproducibility of performance between identically made devices. The small dots are bits of wax used for polishing the sample end-face and still randomly distributed on the surface after 48 hours in ecoclear bath.

Work has to be devoted to optimize all the photolithographic process before etching. Furthermore, electrode mask design and evaporation for poling are in progress.

In conclusion, the design of integrated all-optical active devices employing strip-loaded and rib waveguides have been investigated. The first evidence of guidance is reported in a rib waveguide out of a sputtered $BZH7$ thin film on top of a borosilicate slide. Further research is required to measure the switching voltage on integrated Mach-Zehnder interferometer fabricated by thermally poled bismuth-based waveguides.

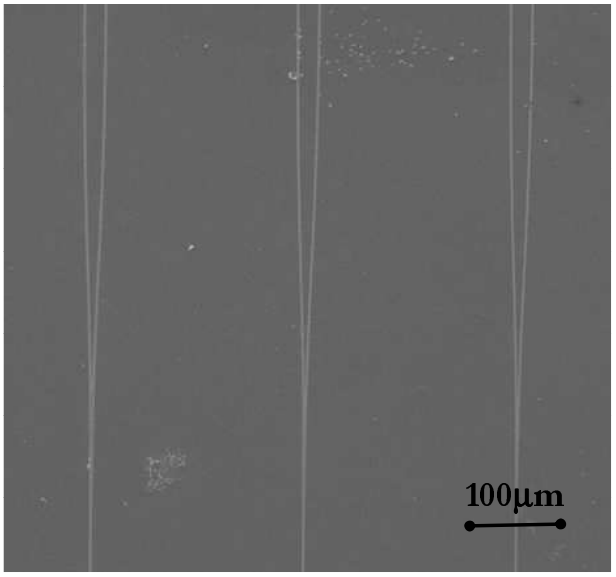


FIGURE 6.15: *SEM* top-view image of three out of six *MZI* devices.

## 6.2 Waveguides by femtosecond laser pulses direct writing technique

Femtosecond laser pulses are widely used as micromachining tool for transparent silica-based materials, 'writing' three-dimensional embedded devices in one-step fabrication process. This route opens new opportunity of fabricating on-chip waveguides of arbitrary length and design to realize high performance integrated all-optical devices.

The femtosecond laser pulses direct writing technique is here successfully tested by Weijia Yang from the ORC to write waveguiding channels on $BZH7$ glasses, near the surface of the sample. Multiphoton absorption in the bulk glass occurs by collimating the beam delivered by an amplified Ti:sapphire laser ($\lambda$= 798$nm$, $f$ = 250$kHz$, $T(FWHM)$ = 160$fs$) and focusing it through a 50× long working distance microscope objective with $NA = 0.55$. The sample is mounted on a $3D$ computer controlled stage and moved in the $x$-axis direction, perpendicular to the direction of beam propagation (Figure 6.16). Different groups of channels are direct-written with sample-speed ranging from 100 to 400 $\mu m/s$ and average beam power either 166 or 200 $mW$.

Glass matrix modifications caused by tightly focused $fs$-pulses induces a refractive index change, which is measured using the interferometric technique in Figure 6.17. The phase shift, proportional to the refractive index, can be calculated by the interference pattern generated from a motorized displacement of the mirror $M_3$. The refractive index change on a $BZH7$ glass sample having a melting point at 1000$^oC$ is measured to be $\approx 3.0\times10^{-3}$.

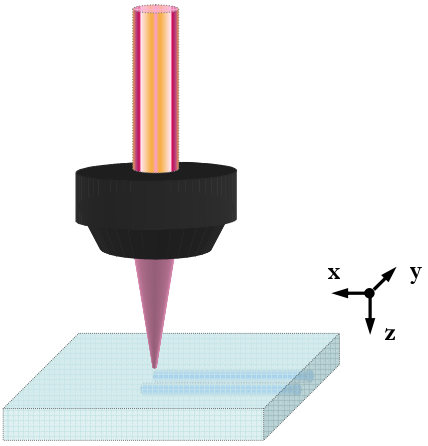


FIGURE 6.16: Schematic of the waveguide writing setup.

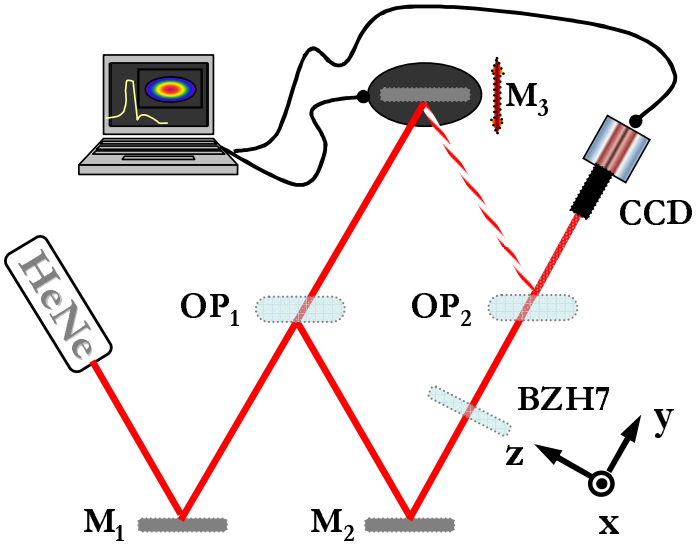


FIGURE 6.17: Schematic of the interferometer used to measure the phase shift of the directly written sample, where $M$ denotes a mirror and $OP$ an optical plate. The mirror $M_3$ is mounted on a computer controlled piezoelectric stage.

The end face of the sample is polished after the writing process to inspect the depth and shape of the waveguides. The polished cross-sections of a channel waveguide written by $fs$-pulses in $0.5\,mm$ thick $BZH7$ bulk are photographed in Figure 6.18. Using a $40\times$ optical microscope, the waveguides are revealed to be elliptical in shape, with a typical size of $(20 \times 100)\,\mu m^2$, as shown on the left hand side in Figure 6.18. The waveguides are multimode when $He - Ne$ laser light ($\lambda = 632.8\,nm$) is launched through. Before poling, the glass surface is polished to reduce the distance between channel and air to below $10\,\mu m$ (right hand side in Figure 6.18), to maximize the spatial matching between the guiding region and the second order nonlinearity induced by poling.

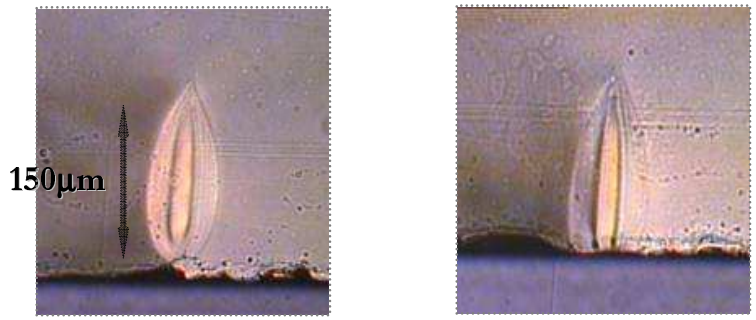


FIGURE 6.18: Cross-section images of a guiding channel ($zy$ plane) before and after poling, respectively. The glass surface was polished to optimize the spatial overlap between nonlinearity and higher-index area, as shown on the right hand side.

No glass damage in the guiding region are revealed by optical microscope inspection after poling at $290^oC$ for 5 minutes with voltage increased during cooling up to a final value $V_{LIM} = 6.5\,kV$, as set on these glass compounds in Section 5.3.1. The recorded $SHG$ signal is uniformly detected all across the electrode area and results comparable to the bulk case in Section 5.3.1.1. The reconstructed $\chi^{(2)}$ profile is expected to be distributed throughout the nonlinear region similarly to the profile 3 in Figure 5.13, with a peak value of around $0.8\,pm/V$.

As a conclusion, the feasibility of direct and cost-effective structuring of embedded all-optical active devices in high index glasses is demonstrated. By appropriate adjustment of the experimental conditions used with silica-based devices, the direct femtosecond pulse laser writing technique is adapted to create a set of waveguiding channels on bismuth-borate glasses. The waveguides are elliptically shaped and multimode in the visible range ($632.8\,nm$). Further investigations are needed to gain control on the cross sectional shaping, to optimize the guiding conditions and to characterize the waveguides index profile, their loss and birefringence.

### 6.2.1 Frequency doubler

The success in poling femtosecond pulse-laser written waveguides leads to the first demonstration of a wavelength converter device in $Bi_2O_3$-based system. In what follows, the conversion efficiency is estimated on a poled $BZH7$ glass with embedded $fs$-written waveguides. The second harmonic signal is expected to be generated when the coupled mode overlaps with the nonlinearity induced by thermal poling, which in turn should be similar to the profile 3 in Figure 5.13. The main issue, while poling waveguiding structures, is to optimize the spatial overlap between the guided mode and the nonlinearity. In twin-hole fibers, for instance, the recorded nonlinearity in the germanium doped core is lower than in bulk silica glasses, as described in Section 3.4.4.

The $1.064\,\mu m$ beam of a Q-Switched (repetition rate $f = 1.004\,kHz$, pulse width $200\,ns$) and mode-locked (pulse width $\tau \cong 300\,psec$) *Nd:YAG* laser is butt-coupled into the end face of poled waveguiding channel. The schematic of the frequency doubler is shown in Figure 6.19.

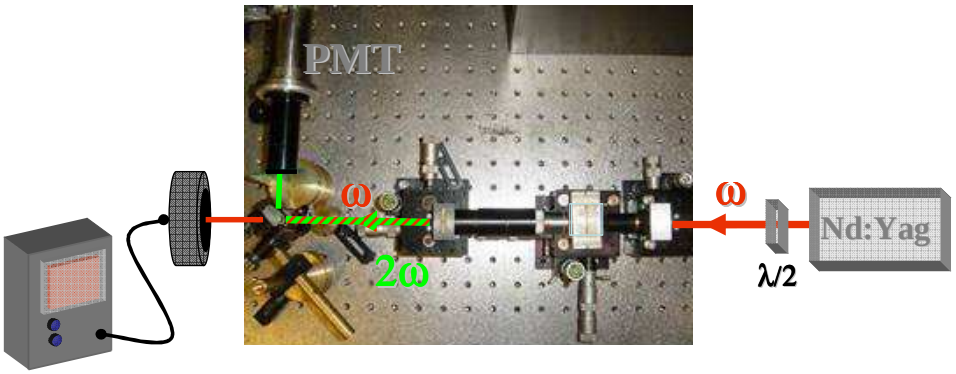


FIGURE 6.19: Schematic of the frequency doubling apparatus to test $fs$-written waveguiding channel.

The power generated at $532\,nm$ is detected by means of the photomultiplier tube (*PMT*) after spectral selection by appropriate laser line filters (minimum peak transmission of 50% at $532 \pm 2\,nm$). The *SH* light power is measured to be three times higher when the polarization of the pump beam is parallel to the electric field induced by poling, than for the orthogonal polarization. Theoretically, the *SH* polarization dependance is expected with a ratio of 9 : 1 between the two orthogonal states, but deviations from such a value have been already reported in waveguides.

Figure 6.20 shows the quadratic dependence of the *SH* power versus the fundamental pump power, which confirms that the signal generated is frequency doubling the infrared incident radiation. Surface damage at the end-face caused by the focused light beam for input pump power above $25 - 30mW$ prevents further increase in the signal.

If the average pump power in the bulk ($P^{\omega}_{bulk}$) and waveguide ($P^{\omega}_{wg}$) are $150\,mW$ and $5\,mW$, respectively, the ratio between the measured *SH* signal intensity is:

$$\frac{P^{2\omega}_{bulk}}{P^{2\omega}_{wg}} \propto \frac{\frac{(P^{\omega}_{bulk})^2}{\pi\,\omega^2_{bulk}} d^2_{bulk}}{\frac{(P^{\omega}_{wg})^2}{\pi\,\omega^2_{wg}} d^2_{wg}} \cong 14.2 \tag{6.3}$$

The poled waveguides exhibit virtually the same nonlinear coefficient ($d_{wg} \cong \chi^{(2)}_{wg}/2$) as the poled bulk bismuthate glass, which is indicative of a predictable overlap between the guided mode and the nonlinear region created by poling. In the calculation used to compare the nonlinear coefficients $d_{wg}$ and $d_{bulk}$ in the Equation 6.3, the mode radius $\omega_{bulk}$ refers to the spot size of the $Nd:YAG$ laser on the bulk sample. The beam

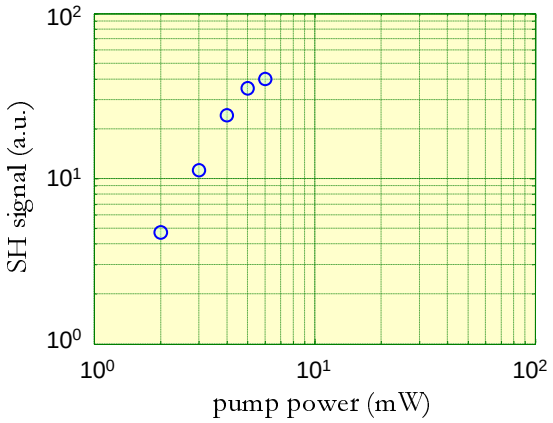


FIGURE 6.20: *SHG* signal dependence with the pump power for the poled $fs$-written waveguide in $BZH7$ glass having a melting point at $1000^oC$.

size has been measured before the focusing lens ($f = 15\,cm$) by knife-edge method. The measurement gave a beam waist radius @$1/e$ equal to $\omega_o = (1.487 \pm 0.02)\,mm$. Gaussian optics propagation enables the spot size in the focal point to be determined according to $\omega_{bulk} = (\lambda \cdot f)/(\pi \cdot \omega_o) = 34.2\,\mu m$. The value of the mode radius $\omega_{wg} \cong 5\,\mu m$ is evaluated from the measured size of the waveguide (i.e. $20 \times 100\,\mu m$): in the case of step-index waveguides, it is $\omega_o = 0.65\times$(core radius), in first approximation. An estimate of the actual $\chi^{(2)}$ value can be derived by the measurement of the electro optic coefficient. Future works aiming at implementing an heterodyne Mach-Zehnder interferometer described in Section 5.2.4 and previously used for the characterization of the poled twin-hole fibre have already been scheduled.

The route to fabricate competitive wavelength converter based on poled bismuth-borate glass is now straightforward. In Figure 5.14, $\chi^{(2)}$ values higher than $\cong 2pm/V$ have already been achieved and there are not fundamental limitations in the implementation of quasi-phase matching ($QPM$) technique (Pedersen et al., 2005).

To summarize, in this section a frequency doubler device based on a poled femtosecond written waveguide on bismuthate high-index glasses has been demonstrated. With the use of thermal poling, the applications can be extended to include new functionality such as frequency mixing and linear electro-optic modulation/switching.

## 6.3 Conclusion

The development of integrated all-optical active devices based on the second-order non-linearity induced in bismuth-based $BZH7$ material by thermal poling is described in this chapter. Two different guiding devices are fabricated, an electro-optic modulator and a frequency converter, based on sputtering and femtosecond laser direct writing,

respectively. Building the results achieved on poling bulk $BZH7$ compounds, work on spatially resolved measurements of $SHG$ induced on slab waveguides is reported. The first demonstration of second-order nonlinearity induced by thermal poling in sputtered $BZH7$ glass films is given. New designs to realizing on-chip structure even more efficiently towards high performance monolithic devices are also provided. Finally, $SON$ generated in poled channel waveguides written by tight focusing femtosecond laser pulses is demonstrated. Further characterization of these devices was rendered impossible because of their destruction, and the destruction of the laboratories, by fire.

# Chapter 7

# Nanocomposite glass

Thermal poling of nanoncomposite silicate glasses is studied as a mean to enhance second-order nonlinearity further, as doping with metal nanoclusters dramatically increases the third-order susceptibility compared to the bulk value. $\chi^{(3)}$ resonant enhancement at the surface plasmon resonance wavelength has been observed at $390 - 420\,nm$ for silver nanoparticles, at $520 - 540\,nm$ for gold nanoparticles and at $560 - 570\,nm$ for cupper nanoparticles. In particular, $\chi^{(3)}$ is resonantly enhanced up to $10^{-7} esu$ in the case of $Ag$ nanoclusters in glass (Chakraborty, 1998), compared to $\chi^{(3)} \cong 10^{-14} esu$ for silica. Assuming that the effective $\chi^{(2)}$ induced in thermally poled glass results from the rectification of the glass third-order susceptibility (Section 2.3.1), second order nonlinearity may be dramatically increased through resonant enhancement of $\chi^{(3)}$.

In this work, local field resonances occurring in $Au$ nanoparticles embedded in a low conductivity sol-gel glass film on a soda-lime glass substrate are aimed to generate higher $\chi^{(2)}$ induced by thermal poling. Unexpectedly, electric-field-assisted dissolution of gold nanoparticles dispersed in the glass matrix is demonstrated. The phenomenon is explained by the ionisation of the $Au$ nanoparticles and the redistribution of gold ions in the glass matrix due to the action of the high electric field locally developed during poling.

## 7.1 Motivation

Dielectric materials showing surface plasmon resonances by inclusion of metallic nanoparticles into their matrix have attracted considerable interest due to unique flexibility in engineering their optical properties (K.L. Kelly and Schatz, 2003). The surface plasmon resonance of the delocalised electrons in the metal (plasmon) dramatically increases the local fields. Specifically, a surface plasmon consists of a resonant excitation, commonly induced by optical radiation, of the electrons at the surface of the metal resulting in a

surface-bound and evanescent electromagnetic wave of optical frequency. The evanescent wave peaks at the interface between the metal nanoparticle and the dielectric and decays exponentially away from the interface such that, in the dielectric, the evanescent wave is mostly confined within a fraction of wavelength. The optical properties of plasmonic composite materials are highly sensitive to the chemical composition of the nanoparticle ($Ag$, $Au$, $Cu$, etc.), the particle geometry (shape, size, etc.), the interface between particle and surrounding and the topology of the metal clusters (Kreibig and Vollmer, 1995). Achieving control of these optical properties is desirable for development of optical devices based on the surface plasmon resonance (Maier et al., 2001).

The discovery of resonant enhancement of $\chi^{(2)}$ at the surface plasmon resonance in thermally poled silica glass doped with silver (Arentoft et al., 2000a) opened up a variety of applications involving the physics behind surface plasmons (Zayats and Smolyaninov, 2003). Deparis et al. (2004b) reported poling-assisted dissolution of silver nanoparticles embedded in ion conducting glass and bleaching of silver-doped nanocomposite materials. As a result of poling, Deparis et al. (2005a) reported a significant change in the plasmon resonance absorbance peak, which led to total or partial bleaching of the initially coloured glass under the anode. It was proposed that the intense electrostatic field, which built-up under the anodic surface during poling, induced the ionization of the silver nanocluster, and subsequently promoted the $Ag^{+}$ ion drifting into the depth of the glass.

A structure made of a highly resistive thin layer containing metal nanoparticles on a ion-conductive substrate is explored here, where gold clusters are embedded in a sol-gel film on top of a soda-lime glass substrate. In spite of its larger thickness, the substrate is expected to be more conductive than the thin film. Within this structure, dissolution of gold nanoparticles by $DC$ electric-field poling is demonstrated only if specific conductivity conditions are satisfied.

## 7.2 Glass under study

The nanocomposite film is fabricated at the NSG facilities by the sol-gel method through the coating of a solution containing an organic silicon compound and a salt of gold onto a glass plate. As a result, the nanoparticles are randomly distributed within the film and no gradient of Au-particle concentration across the depth is observed when the Scanning Electron Microscope ($SEM$) image of an etched sample cross section is examined. In Figure 7.1 the film structure reveals nanoparticles uniformly dispersed in the matrix of silicate glass.

Two sets of $3\,mm$ thick substrates with different sol-gel film compositions (type I and type II) are investigated (Mezzapesa et al., 2006). The sol-gel layer is $130\,nm$ and $140\,nm$ in thickness, the volume fraction of $Au$ is estimated to be 2.3% and 5.2% and the $Au$

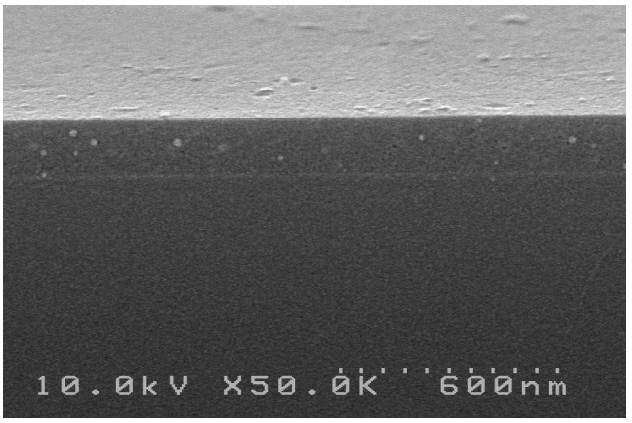


FIGURE 7.1: SEM image of a pink sample (type I): etched cross section (magnification: 50000×, tilt angle: $10deg$). The gold nanoparticles can be seen as white spots randomly distributed in the $130\,nm$ thick sol-gel film.

particle diameter is $15\,nm$ and $8.5\,nm$ for type I and type II samples, respectively. Iron oxide is also present in the substrate of type I ($0.1wt\%$) and type II ($0.6wt\%$) samples.

| Glass Colour | Refractive Index | Sol-gel Film Composition | wt% | Film Thickness |
|---|---|---|---|---|
| Pink (type#1) | 1.46 | $SiO_2$<br>$TiO_2$<br>$CeO_2$<br>Au | 75.7<br>3.3<br>5.0<br>16.0 | 130 nm |
| Blue (type#2) | 1.87 | $SiO_2$<br>$TiO_2$<br>$CeO_2$<br>Au | 19.5<br>25.9<br>38.6<br>16.0 | 140 nm |

FIGURE 7.2: Characteristics of thin sol-gel films doped with $Au$ nanoparticles.

According to the film composition, the samples are either pink (type I) or blue (type II) tinted, which is explained by the shift of the surface plasmon resonance towards the red with increasing host refractive index in these gold nanocomposite glasses (Tsujino et al., 2000), as predicted by the Maxwell-Garnett effective medium theory. Details on poling treatments are given in the next section.

## 7.3 Electric-field driven bleaching

In order to perform a comparative study on the two types of nanocomposite sol-gel film, both pink and blue coloured samples are identically poled at $280^oC$ in air atmosphere by applying up to $1\,kV$ through pressed-contact steel electrodes ($9 \times 7mm$), with the sol-gel film surface facing the anode. The procedure used for poling soda-lime glass (Garcia et al., 1998) is employed because of the high ionic conductivity of the substrate. Assuming that the resistivity of the film ($\rho_{film}$) is five orders of magnitude higher than that of the substrate ($\rho_{sub}$), more than 80% of the applied voltage would drop across the film according to:

$$V_{film} = \frac{1}{1 + \frac{\rho_{sub} d_{sub}}{\rho_{film} d_{film}}} \tag{7.1}$$

in spite of the ratio between the thickness of the film ($d_{film}$) and substrate ($d_{sub}$) being only $\approx 4.5 \times 10^{-5}$.

The voltage is increased in steps of $200\,V$ for a fixed period of time ($10\,min$ each step). During each step, the current is limited in order to avoid runaway. When the final poling voltage is reached, the sample is cooled to room temperature whilst the voltage is applied. The temporal evolution of the poling current is shown in Figure 7.3.

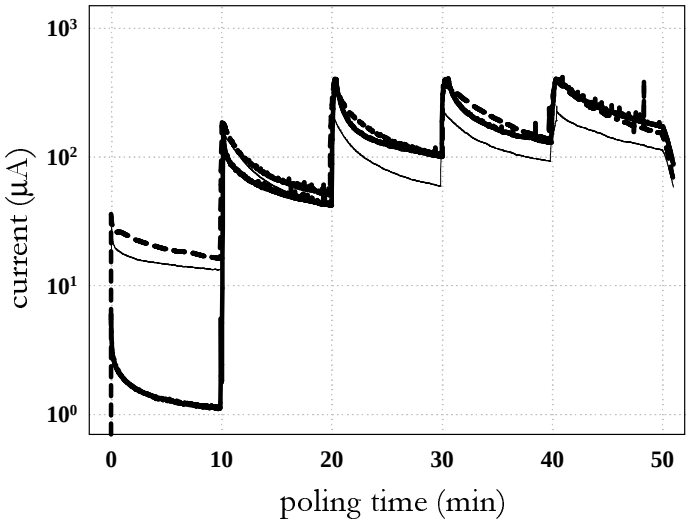


FIGURE 7.3: Time evolution of the current during poling at $280^oC$ with the voltage increased in steps of $200\,V$ ($10\,min$ each step) up to $1\,kV$ (thick solid line: pink sample, thin solid line: blue sample). A type I sample is also poled with inverted polarity, i.e. with the film surface facing the cathode (dashed line).

The current dynamics can be understood in terms of ion depletion which takes place in the two-layer dielectric structure during poling. At the beginning of poling, the level of current in the pink sample is an order of magnitude lower than in the same sample

poled with reverse polarity, i.e. with the film facing the cathode. This observation is in accordance with a lower resistivity of the bulk (substrate) relative to the sol-gel glass film. When the film faces the anode, there is no supply of cations from the anode (blocking electrode). Conversely, when the film faces the cathode the film may not block the movement of the cations (sodium ions, mainly) from the bulk. The asymmetry in the current evolution with respect to polarity is therefore explained by considering thermally activated cations injected from the bulk into the film, thus enhancing the conductivity of the film. Moreover, after the first voltage step, the current evolution in the pink sample trends towards the behavior of the inverted-poled pink sample. This result is interpreted as an indication of film conductivity increase, which may be associated with the onset of $Au$ nanoparticle dissolution. Conductivity changes have already been reported for silver nanoparticle dissolution (Deparis et al., 2005a). However, the mobility of gold ions is not believed to contribute to the conductivity of the sol-gel layer in the present case. A possible explanation is the formation of defects in the sol-gel film, such as broken bonds, which could result in the increase of electron mobility. The blue sample follows a behavior similar to the inverse-poled pink sample throughout the poling process, both in terms of current level and decay rate.

After poling, no $SHG$ signal is detected across the electrode area, although the film becomes colourless within the region of the pink sample delimited by the anode geometry, as reported in Figure 7.4. The electric-field-driven dissolution of randomly distributed gold nanoparticles ($15\,nm$ in diameter) has taken place. It is separately verified that the sample become colourless when the thin film is removed by chemical etching.

FIGURE 7.4: Photograph of pink sample after poling at $280^oC$ and $1\,kV$. The bleached (i.e. colourless) region under the anode is well defined by the electrode size.

### 7.3.1 Dissolution of Au nanoparticles

As reported for silver nanoparticles embedded in soda-lime glass (Deparis et al., 2004b), we propose that, under the action of the high electric field which develops in the sol-gel film during poling, ionization of the gold nanoparticles occurs with a subsequent migration of monovalent $Au^+$ ions into the glass substrate.

The measured absorbance spectra of unpoled and poled regions of the pink sample are shown in Figure 7.5, where the poling induced suppression of the main absorbance band in the visible range, is the evidence of the bleaching effect. The peak of the absorption band is located at $520\,nm$, as reported for surface plasmon resonance of such $Au$ particles (Doremus, 1964). The absorption band centred at $376\,nm$ is attributed to $Fe^{3+}$ content in the host material, as confirmed by the manufacturers.

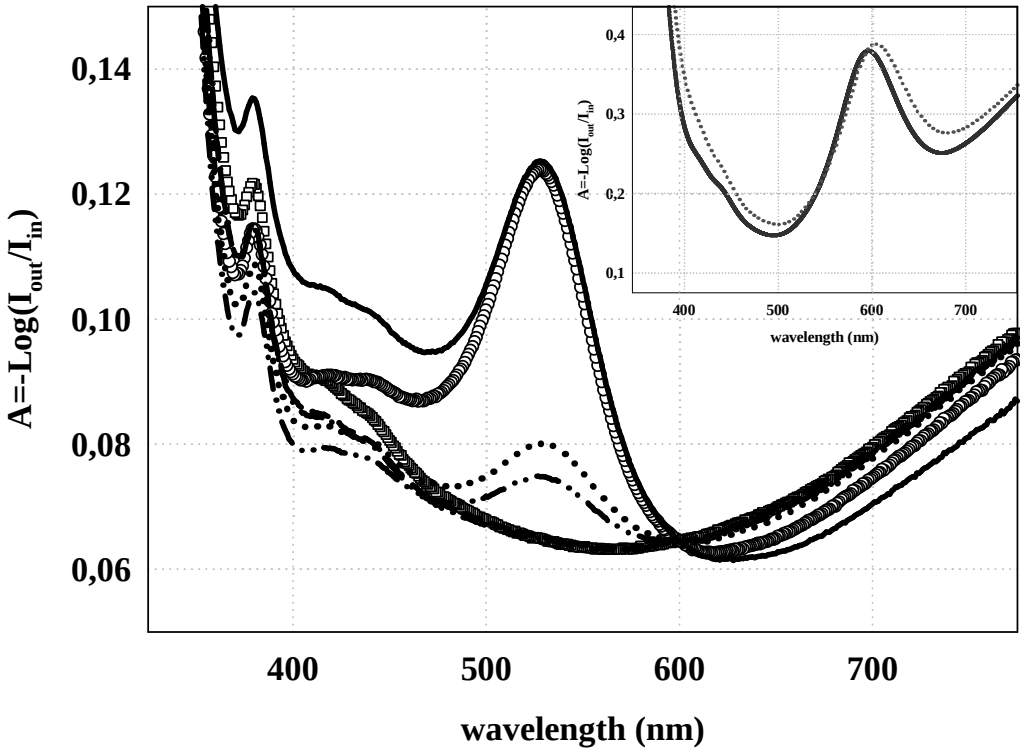


FIGURE 7.5: Evolution of the optical absorbance spectrum of pink samples after poling with stepwise increasing voltage: $5 \times 200\,V$ (thick solid line), $4 \times 200\,V$ (dashed line), $3 \times 200\,V$ (dashed-dotted line), $2 \times 200\,V$ (dashed-double-dotted line), $1 \times 400\,V$ (dotted line). The absorbance of the sample poled with reverse polarity (symbols) retraces the absorbance of the pristine sample (thin solid line) above $500\,nm$. Inset: absorbance spectra of the pristine (solid line) and $1\,kV$ poled (dotted line) blue sample.

No change in the surface plasmon resonance is measured after poling the pink sample with reversed polarity (symbols in Figure 7.5), with the film facing the cathode. This is not surprising, since the static electric field ($E_{DC}$) distribution induced by cation migration is localized under the anodic surface. When the film faces the anode, the value of $E_{DC}$ can be estimated by assuming, for simplicity, a uniform field distribution across

the $130\,nm$ film thickness. By taking the smallest voltage value of $200\,V$, an $E_{DC}$ as high as $1.5\times10^9\ V/m$ can be obtained in the thin film. When compared with the electric field necessary to dissolve $Ag$ particles embedded in glass ($E_{DC}\cong\ 1kV/5\,\mu m = 2\times10^8 V/m$ reported by Deparis et al. (2004b)), the electric field evaluated for the dissolution of $Au$ particles results higher by one order of magnitude. The reason for such a difference might be sought in the standard potential $E_o$, which indicates the degree of metal ionisation at room temperature (at $25^oC$). As a general rule, the greater the normal electrode potential, the more difficult the ionisation of the metal. The normal electrode potential $E_o$ is $0.80\,V$ and $1.83\,V$ for silver and gold, respectively (Bard et al., 1985).

Additional experiments are also performed in order to evaluate the voltage threshold for electric-field-assisted dissolution of gold nanoparticles. Pink samples are poled following the same poling procedure as described in Section 7.3 but varying the final voltage ($400\,V$, $600\,V$, $800\,V$ and $1\,kV$). Figure 7.5 shows the absorbance spectra measured as a function of final poling voltage. For a final voltage as low as $400\,V$, more than 50% reduction of the gold surface plasmon resonance is revealed, regardless of the number of voltage applied steps.

In contrast to the observations in the pink sample, no bleaching was observed in the blue sample after identical poling conditions; in the inset of Figure 7.5 the absorbance spectra of the pristine and poled blue samples are compared. This striking difference in behaviour of pink and blue samples is thought to be due to variations of resistivity and dielectric constant with the film composition. This allows for a greater $E_{DC}$ electric field to develop in the pink sample film under the same poling conditions.

### 7.3.2 Discussion

The mechanism of gold cluster dissolution is as follows. In the presence of a high electric field, the cluster is ionized; electrons are ejected and extracted at the anode via tunnelling from one cluster to the nearest one; the positively charged gold ions are stripped off from the cluster by Coulomb forces and then migrate towards the cathode, leaving uncharged gold cluster behind (Podlipensky et al., 2004). This process could cycle until the cluster is totally destroyed and the gold ions are dissolved in the matrix. In this framework, the average distance between clusters could also influence the electronic conductivity via the potential barrier height for tunnelling. The estimated filling fraction is 2.3% in the pink $Au$ doped sol-gel film, much lower than the reported value for the $Ag$ doped glass (tens of percent), thus justifying the more intense electric field strength required for gold dissolution.

## 7.4 Conclusion

The demonstration of electric-field driven bleaching of *Au*-doped nanocomposite sol-gel films on top of ion-conducting glass substrate represents the starting point in extending the bleaching of glasses with various compositions. Along with the poling procedure, the sol-gel film composition is shown to play a crucial role in the dissolution process. Furthermore, on the contrary to the previously reported results on silver nanoparticles, dissolution of gold nanoparticles is observed despite their much lower filling factor. Finally, the perspective of being able to dissolve even less mobile particles embedded in thin films, such as platinum and palladium, broadens the application of poling-assisted bleaching towards optical device fabrication.

# Chapter 8

# Conclusions and Further Work

## 8.1 Overview

Active nonlinear optical components based on poled glasses are promising candidates for low-cost applications in the next generation optical communications and integrated optics. The poling technique does effectively break the inversion symmetry of the glass matrix, allowing otherwise vanishing even-order nonlinear interactions, such as second harmonic generation, electro-optical modulation, wavelength conversion, routing and switching. In thermally poled silica-based devices, second order nonlinearity as high as $1\,pm/V$ are recorded and spatially confined in a few micron thick layer beneath the anodic surface (Section 5.2.2), a feature that is compatible with planar waveguide designs and fibre geometries. However, the rectification of the intrinsic third-order nonlinear optical susceptibility, $\chi^{(3)}$, by the built-in electrostatic field (see Section 2.3.1), sets an upper limit to $\chi^{(2)}$ values, given by the dielectric breakdown strength of the glass compound. To account for more efficient second order susceptibility, research on thermal poling is progressively moving from silica-based to high-index glass systems. Among the others, heavy-metal oxide glasses with higher third order nonlinearity than silica, such as lead glasses, $TiO_2-$ and $WO_2$- containing glasses, have already permitted $\chi^{(2)}$ to scale up proportionally (Section 1.1.3).

The aim of this thesis was to induce efficient second-order nonlinearity in newly patented bismuthate glass compounds and pursuing the development of active optoelectronic prototypes based on thermally poled bismuth-based waveguiding device. In particular, an electro-optic modulator and a frequency converter have been targeted, based on sputtering and femtosecond laser direct writing technique, respectively.

The state of the art on both glasses for poling and characterisation techniques for spatially resolved $SON$ measurement have been established as a foundation for this research (Chapter 2-3). The experimental reproducibility has been guaranteed through a detailed

work on optimizing poling conditions for novel bismuth-based glass compounds along with their chemical composition (see Chapter 4). Furthermore, peak $\chi^{(2)}$ values as high as $2.3\,pm/V$ in bulk bismuth-based glasses have been achieved by employing the innovative poling technique described in Chapter 5. The accurate knowledge of the $\chi^{(2)}$ profile has allowed to tailor the integration of second-order nonlinearity in waveguiding regions. The first demonstration of $\chi^{(2)} \cong 2.0\,pm/V$ induced by thermal poling in radio-frequency sputtered $BZH7$ glass thin film is finally reported in Chapter 6 along with efficient poling on channel waveguides written by tight focusing femtosecond laser pulses. The full characterization of the poled Mach-Zehnder interferometers was curtailed as all devices, and the equipment to fabricate and characterize them, were destroyed in the fire.

## 8.2 Principal results of the thesis

The originality of this thesis work consists on having generated understanding of poling novel bismuth-based glass structures. Inducing permanent and large second order nonlinearity in bismthate glasses, quantifying the processes and then establishing the technology to integrate the nonlinearity in waveguiding layers have contributed to engineering and developing bismuth-based active devices, such as frequency doubler and eletro-optic modulator. The project strategic plan is outlined as follows:

**Establishment of characterization techniques for $SON$ distribution**

In this thesis, characterization techniques to determine the nonlinear formation dynamics and resolve nonlinear thickness and profile have been evaluated and applied to thermally poled glass to quantify the magnitude and distribution of poling induced second order nonlinearity in bismuthate glasses for the first time. Detailed informations about the $SON$ distribution in depth have been crucially important for understanding and optimizing all the parameters affecting the poling process of these novel glasses, such as the dependence on temperature, poling field, electrode materials, sample chemical composition, etc. In particular, advantages and drawbacks are outlined when the Maker Fringe method, the layer peeling procedure and scanning optical microscopy, are all employed to investigate and characterize the poling induced second order nonlinearity in thin guiding regions.

**Thermal poling on novel high-index glass compounds to enhance $\chi^{(2)}$**

The fundamental research on poling induced nonlinearity has been extended to investigation on high-index bismuth-based glass (Chapter 4), since the second-order susceptibility is predicted to enhance in proportion to the intrinsic third-order optical nonlinearity, for a given frozen-in electric field strength (Equation 2.9). After poling, $SHG$ powers as high as in silica have been measured for the first time from novel bismuth-borate

glass systems ($Bi_2O_3$-$ZnO$-$B_2O_3$). The $\chi^{(2)}$ value is shown to scale linearly with $\chi^{(3)}$, whose value is measured to increase with the bismuth oxide content (Section 4.1.2). A poling mechanism relying on proton migration and glass ionization has been proposed to account for all the experimental evidence leading to $\chi^{(2)}$ formation. Based on the proposed poling mechanism, a simple model relating the second-order nonlinear susceptibility induced in poled bismuthate glasses to their electronic and ionic conductivity has been developed. It has been found that bulk electronic conductivity higher than ionic conductivity prevents the achievement of a frozen-in electric field large enough to generate efficient second order nonlinearities in $Bi_2O_3$-based glasses. The observation that the dielectric breakdown strength decreases with increasing $Bi_2O_3$ content leads to the proposal that poling efficiency may be increased in conductive bismuthate glass by optimizing the poling conditions and selecting glass compositions on the basis of both $\chi^{(3)}$ and the intrinsic property of the bulk material.

**Improved processes for poling**

The establishment of an innovative variable-voltage poling technique has allowed to record a peak $\chi^{(2)} = 2.3\,pm/V$, the highest value ever reported on thermally poled bismuth-based glasses (see Section 5.3). The assisted-voltage treatment leads to enhance the built-in electric field inside the nonlinear region during the cooling phase, when the dielectric breakdown point of the sample tends to increase. Furthermore, by increasing the voltage when the ion mobility decreases during cooling yields to controlling the nonlinear spatial distribution and thickness, thus optimizing the spatial overlap of second-order nonlinearity in waveguiding devices. More efficient optical interactions in glass-based active planar waveguides and optical fibres may now be achieved.

**Waveguide devices employing poling**

The first demonstration of a peak second-order nonlinearity as high as $2.0\,pm/V$ induced by thermal poling in sputtered monomode bismuth-based slab waveguides is reported in this thesis. This value is 3 times higher than quartz and approximately 10 times higher than in poled silica fibres. Mode profile measurements from a Mach-Zehnder modulator based on bismuthate rib waveguide geometry are also provided. The first demonstration of a frequency doubler device based on poled channel waveguides written by tight focusing femtosecond laser pulses on $Bi_2O_3$-based system is given. New opportunities of fabricating on-chip waveguides of arbitrary length and design are opened. The applications can be extended to include new functionality such as frequency mixing and linear electro-optic modulation/switching. New designs to realize efficient monolithic structures leading to high performance active devices are investigated.

**Enhancement of material nonlinearity**

Thermal poling of nanoncomposite silicate glasses is investigated as a further study on materials possessing high third order nonlinearity. Local field resonances occurring at

gold nanoparticles dispersed in the glass matrix are aimed to generate higher $\chi^{(2)}$ after poling. Although no *SHG* signal could be generated, the first electric-field assisted bleaching and dissolution of *Au* nanoparticles is demonstrated.

## 8.3 Future work

A definitive conclusion that can be drawn from the results described in this thesis is that, owing to the large $\chi^{(3)}$ of bismuth-based glass system compared to silica (see Table 4.2), even higher nonlinearities are theoretically achievable. Optimization of poling of bismuth-based glasses with higher bismuth oxide content, and hence high refractive index and $\chi^{(3)}$, would be expected to lead to observation of higher second-order nonlinearity. The conventional characterization of the third order nonlinear optical susceptibility before and after poling may also permit to reveal local $\chi^{(3)}$ modification, as already reported in silica based systems.

More effort is desirable to be spent on reliable fabrication of planar waveguides: along with the spatially resolved measurements of *SHG* in poled waveguides, a detailed characterization of complete channel waveguide circuits needs to be carried out, with particular emphasis towards a systematic study of a range of both electrodes and substrate materials. As the induced *SON* requires a refined detection system to be unambigously revealed, it would be convenient to assemble in-situ monitoring of the evolution of the linear electro-optic coefficient with poling parameters on bismuth-based waveguiding devices, as done for twin-hole fibres in Section 5.2.4. Future work might therefore concentrate on the study of the effect of high fields thermal poling upon waveguides in glass. Acquiring such a kind of knowledge is fundamental to starting speculations on which parameters may be varied to optimizing the device performances.

### 8.3.1 Immediate targets

Based on the achievements on poled bismuthate glass waveguide, both a wavelength converter and electro-optical modulator design are proposed and their performance simulated.

**Frequency conversion via quasi-phase-matching**

Frequency conversion can be achieved by exploiting optical parametric processes. The figure of merit for a wavelength converter is given by $(\chi^{(2)}LI)^2$, where $L$ is the length of the device and $I$ the pump intensity. Only $0.43\,dB$ of splicing losses were already reported for bismuth-erbium doped and standard silica SM fibres (Ohara et al., 2003), comparable with the typical coupling losses from monomode fibre into Ti-diffused lithium niobate waveguides. Lower nonlinearity in glass compared to modulator based on

$LiNbO_3$ crystal, can be compensated by using a longer waveguide length and/or quasi-phase-matching in periodically poled waveguides. The latter is a route towards more efficient interaction, since it implies a partial modulation of the optical nonlinearity through periodic poling. The resulting nonlinearity has an effective value which is about one third of the starting value in a uniform-poled structure, but with the advantage of providing phase-matching for the interaction.

As an example, a $10\,cm$ long periodically-poled bismuthate glass waveguide is considered. The mode radius is taken equal to $1.5\,\mu m$ in the simulation and the effective nonlinearity is $\chi_{eff} \approx 2\,pm/V$ (in the uniformly-poled structure would need to be $6\,pm/V$). The wavelength conversion is generated from $\lambda_i = 1503\,nm$ to $\lambda_s = 1509\,nm$ or vice versa using a pump at $753\,nm$. A conversion efficiency from $\lambda_i$ to $\lambda_s$ of 50% for a pump power of $500\,mW$ can be obtained. This efficiency scales with the square of the nonlinearity. Moreover, the estimated efficiency in Figure 8.1 for a $25\,cm$ long frequency doubler features a linear dependence with the fundamental peak power and can achieve values bigger than 30% for a pump power smaller than $500\,mW$ (top and bottom, respectively). By integrating very small mode-size waveguiding nanowire of high-index bismuthate glass with oxidized silicon cladding layers would finally allow to increase the efficiency for lower input power.

**Electro-optic modulators and switches**

The switching voltage for an electro-optical modulator based on a $2 \times 2$ Mach-Zehnder interferometer is estimated for a device operating at a wavelength of $1550\,nm$, with an active length of $24\,cm$ and electrode spacing of $10\,\mu m$. The optical limit on the bandwidth of a poled glass modulator is about $2\,GHz \cdot cm$ for a lumped-electrode configuration ($LEC$) and $10\,GHz \cdot cm$ for a travelling-wave electrode configuration ($TWC$). By using periodic poling it is possible to compensate the phase-mismatch between the driving microwave signal and the optical wave in the $TWC$, thus shifting the bandwidth of the device towards even higher frequency. The requirement for the driving voltage-length product can be estimated to be $14\,V \cdot cm$ for an electro-optic coefficient of $r = 10\,pm/V$, although the switching voltage required in the configuration push-pull can be lowered to $12\,V$ for just $\chi^{(2)} = 2.5\,pm/V$. This value can be 10 times smaller if $\chi^{(2)} = 25\,pm/V$, theoretically achievable in bismuth-based glass devices.

These figures indicate that the development of active waveguide devices based on bismuth-glass is a promising technology towards wide spread integration of poled competitive glasses on compact chips containing for instance broad-band bismuth doped amplifiers.

### 8.3.2 Potentially "polable" nonsilicate glass

Further increases in $\chi^{(2)}$ and understanding of poling processes, greater flexibility in materials composition, and improved integration may be achieved by studying alternative

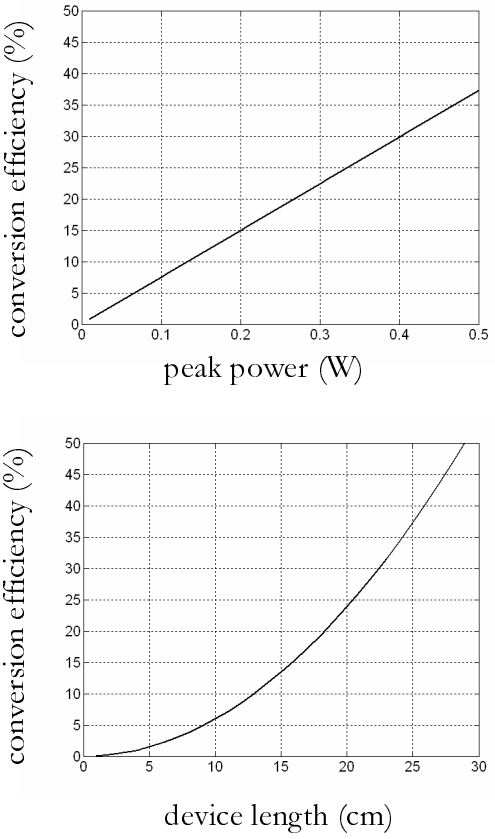


FIGURE 8.1: Estimates of conversion efficiency for a frequency doubler based on a periodically poled bismuthate waveguide. The nonlinearity is assumed to be $2.5\,pm/V$, the refractive index $n = 1.8$ and the pump and $SH$ modes overlapping area $A_{OVL} = 17.46\,\mu m^2$. (Top): The efficiency is plotted against the pump peak power. A $25\,cm$ long periodically poled waveguide is assumed. (Bottom): The efficiency is plotted against the waveguide length. Fundamental peak power of $500\,mW$ is assumed.

glass systems such as:

- thin dielectric films of material with high $\chi^{(3)}$ sandwiched between silica cladding layers, to inducing second order nonlinearity preferably inside these waveguiding thin layers
- bulk glass containing more than one alkali or alkaline-earth ion to realizing channel waveguides by differential ionic drift and simultaneous applying high electrostatic fields
- glass matrix doped with rare earth ions for the understanding of the presence of localized dopants upon poling

In the last case, the experimental investigation of poling induced $SON$ upon local concentration distributions of dopants must require the ability to introduce a predictive $\chi^{(2)}$ in glasses for their potential use in all-optical waveguide devices. An example of such a device is an integrated frequency-doubled laser. In this device, a glass waveguide in

a rare-earth-doped glass substrate is combined with Bragg gratings, serving as cavity mirrors, and a $\chi^{(2)}$ grating to double the frequency of the fundamental beam. Phosphate glasses are substrates of choice because they can incorporate a large concentration of rare-earth ions to work in optical communications technology. Indeed, Erbium-doped glasses act as a three level system at $1.5\,\mu m$ and codoping with ytterbium is generally used (Laporta et al., 1999) to decrease the threshold pump power required, owing to an effective ytterbium to erbium transfer mechanism of the excitation energy. Considerable interest is aimed to achieving optical $SHG$ in $Er/Yb$ doped planar waveguides, having in mind the miniaturized single-chip realization of integrated amplifiers and lasers, key component in all modern optical transmission system.

# Bibliography

M. Abe, T. Kitagawa, K. Hattori, A. Himeno, and Y. Ohmori. Electro-optic switch constructed with a poled silica-based waveguide on a Si substrate. *Electron. Lett.*, 32 (10):893–894, 1996.

R. Adair, L. L. Chase, and S. A. Payne. Nonlinear refractive index measurement of glasses using three-wave frequency mixing. *J. Opt. Soc. Am. B*, 4(6):875–881, 1987.

R.R. Alfano. *Semiconductors Processes Probed by Ultrafast Laser Spectroscopy, Volume I.* Academic, New York, 1984.

T.G. Alley and S.R.J. Brueck. Visualization of the nonlinear optical space-charge region of bulk thermally poled fused-silica glass. *Opt. Lett.*, 23(15):1170–1172, 1998.

T.G. Alley, S.R.J. Brueck, and R.A. Myers. Space charge dynamics in thermally poled fused silica. *J. Non-Cryst. Sol.*, 242(2), 1998.

T.G. Alley, S.R.J. Brueck, and M. Wiedenbeck. Secondary ion mass spectrometry study of space-charge formation in thermally poled fused silica. *J. Appl. Phys.*, 86(12): 6634–6640, 1999.

J. Arentoft, M. Kristensen, K. Pedersen, S. Bozhevolnyi, and P. Shi. Poling of silica with silver-containing electrodes. *Electron. Lett.*, 36(19):1635–1636, 2000a.

J. Arentoft, K. Pedersen, S.I. Bozhevolnyi, M. Kristensen, P. Yu, and C.B. Nielsen. Second-harmonic imaging of poled silica waveguides. *Appl. Phys. Lett.*, 76(1):25–27, 2000b.

E. Atanassova, N. Novkovski, A. Paskaleva, and M. Pecovska-Gjorgjevich. Oxygen annealing modification of conduction mechanism in thin rf sputtered $Ta_2O_5$ on Si. *Solid-State Electronics*, 46:1887–1898, 2002.

N. P. Bansal and R. H. Doremus. *Handbook of Glass Properties.* Academic Press, New York, 1986.

A.J. Bard, R. Parsons, and J. Jordan. *Standard Potentials in Aqueous Solution.* Marcel Dekker, New York, 1985.

P. Becker. Thermal and optical properties of glasses of the system $Bi_2O_3B_2O_3$. *Crystal Research and Technology*, 38:74–82, 2003.

H. Behrens, R. Kappes, and P. Heitjans. Proton conduction in glass: an impedance and infrared spectroscopic study on hydrous $BaSi_2O_5$ glass. *J. Non-Cryst. Sol.*, 306: 271–281, 2002.

M.V. Bergot, M.C. Farries, M.E. Fermann, L. Li, L.J. Poyntz-Wright, P.S.J. Russell, and A. Smithson. Generation of permanent optically induced second-order nonlinearities in optical fibers by poling. *Opt. Lett.*, 13(7):592–594, 1988.

R. J. Barczynski B.Kusz, K. Trzebiatowski. Ionic conductivity of bismuth silicate and bismuth germanate glasses. *Sol. State. Ionics*, 159:293–299, 2003.

N. Bloembergen and P.S. Pershan. Light waves at the boundary of nonlinear media. *Phys. Rev.*, 128(2):606–622, 1962.

R.W. Boyd. *Nonlinear Optics*. Academic, London, 1992.

A.L.R. Brennand and J.S. Wilkinson. Planar waveguides in multicomponent glasses fabricated by field-driven differential drift of cations. *Opt. Lett.*, 27(11):906–908, 2002.

C. Cabrillo, F.J. Bermejo, J.M. Gibson, J.A. Johnson, D. Faccio, V. Pruneri, and P.G. Kazansky. Thermally poled silica samples are structurally heterogeneous: Electron diffraction evidence of partial crystallization. *Appl. Phys. Lett.*, 78(14):1991–1993, 2001.

C. Cabrillo, G.J. Cuello, P. Garcia-Fernandez, F.J. Bermejo, V. Pruneri, P.G. Kazansky, S.M. Bennington, and W.S. Howells. Emergence of structural anisotropy in optical glasses treated to support second harmonic generation. *Phys. Rev. Lett.*, 81(20):4361–4364, 1998.

A. Canagasabey, F.P. Mezzapesa, C. Corbari, P.G. Kazansky, and M. Ibsen. 75% enhancement of the second order nonlinearity in twin-hole fibres through voltage assisted cooling during poling. *Proc. CLEO*, 2006.

D.E. Carlson. Anodic proton injection in glasses. *J. Non-Cryst. Sol.*, 57(11):461–465, 1974.

P. Chakraborty. Metal nanoclusters in glasses as non-linear photonic materials. *Journal of Materials Science*, 33(9):2235–2249, 1998.

G. Chen, Y. Tanaka, T. Takada, and L. Zhong. Effect of polyethylene interface on space charge formation. *IEEE Transactions on Dielectrics and Electrical Insulation*, 11(1): 113–121, 2004.

B.V.R. Chowdari and Z. Rong. Role of $Bi_2O_3$ as a network modifier and a network former in $xBi_2O_3(1-x)LiBO_2$ glass system. *Solid State Ionics*, 90:151–160, 1996.

C. Corbari, A. Canagasabey, M. Ibsen, F. Mezzapesa, C. Codemard, J. Nilsson, and P.G. Kazansky. All-fibre frequency conversion in long periodically poled silica fibres. *Proc. OFC*, 2005.

C. Corbari, O. Deparis, B.G. Klappauf, and P.G. Kazansky. Practical technique for measurement of second-order nonlinearity in poled glass. *Electron. Lett.*, 39(2):197–198, 2003.

C. Corbari, J.D. Mills, B.G. Klappauf, and P.G. Kazansky. Thermal poling of glass modified by femtosecond laser irradiation. *Appl. Phys. Lett.*, 81(9):1585–1587, 2002.

O. Deparis, C. Corbari, P. G. Kazansky, and K. Sakaguchi. Enhanced stability of the second-order optical nonlinearity in poled glasses. *Appl. Phys. Lett.*, 84(24):4857–4859, 2004a.

O. Deparis, P.G. Kazansky, A. Abdolvand, A. Podliensky, G. Seifert, and H. Graener. Poling-assisted bleaching of metal-doped nanocomposite glass. *Appl. Phys. Lett.*, 85 (2):872–874, 2004b.

O. Deparis, P.G. Kazansky, A. Podliensky, A. Abdolvand, G. Seifert, and H. Graener. Evolution of poling-assisted bleaching of metal-doped nanocomposite glass with poling conditions. *Appl. Phys. Lett.*, 86(261109), 2005a.

O. Deparis, F.P. Mezzapesa, C. Corbari, P. G. Kazansky, and K. Sakaguchi. Origin and enhancement of the second-order non-linear optical susceptibility induced in bismuth borate glasses by thermal poling. *J. Non-Cryst. Sol.*, 351(36):2166–2177, 2005b.

R. DeSalvo, A.A. Said, D.J. Hagan, E.W. Van Stryland, and M. Sheik-Bahae. Infrared to ultraviolet measurements of two-photon absorption and $n_2$ in wide bandgap solids. *IEEE J. Quant. Electron.*, 32(8):1324–1333, 1996.

E.M. Dianov, P.G. Kazansky, and D.Yu Stepanov. Problem of the photo-induced second harmonic generation in optical fibers. *Sov. J. Quantum Electron*, 19(5):575–576, 1989.

R. H. Doremus. Optical properties of small gold particles. *J. Chemical Physics*, 40(8): 2389–2396, 1964.

M. Dussauze, E. Fargin, M. Lahaye, V. Rodriguez, and F. Adamietz. Large second harmonic generation of thermally poled sodium borophosphate glasses. *Opt. Express*, 13(11):4065–4069, 2005.

H. Ebendorff-Heidepriem, P. Petropoulos, V. Finazzi, S. Asimakis, J. Leong, F. Koizumi, K. Frampton, R.C. Moore, D.J. Richardson, and T.M. Monro. Heavy metal oxide glass holey fibers with high nonlinearity. *Proc. OFC*, 4:103–106, 2005.

D. Faccio, A. Busacca, D.W.J. Harwood, G. Bonfrate, V. Pruneri, and P.G. Kazansky. Effect of core-cladding interface on thermal poling of germano-silicate optical waveguides. *Opt. Commun.*, 196(1), 2001a.

D. Faccio, V. Pruneri, and P.G. Kazansky. Noncollinear Maker's fringe measurements of second-order nonlinear optical layers. *Opt. Lett.*, 25(18):1376–1378, 2000.

D. Faccio, V. Pruneri, and P.G. Kazansky. Dynamics of the second-order nonlinearity in thermally poled silica glass. *Appl. Phys. Lett.*, 79(17):2687–2689, 2001b.

Y. Fujii, B. Kawasaky, K.O. Hill, and D.C. Johnson. Sum frequency light generation in optical fibres. *Opt. Lett.*, 5(4):48–52, 1980.

T. Fujiwara, S. Matsumoto, M. Ohama, and A. J. Ikushima. Origin and properties of second-order optical non-linearity in ultraviolet-poled $GeO_2$-$SiO_2$ glass. *Journal of Non-Crystalline Solids*, 273:203–208, 2000.

T. Fujiwara, D. Wong, Y. Zhao, S.Fleming, S. Poole, and M. Sceats. Electro-optic modulation in germanosilicate fibre with UV-excited poling. *Electron. Lett.*, 31(7): 573–575, 1995.

F.C. Garcia, I.C.S.Carvalho, E. Hering, W.Margulis, and B. Lesche. Inducing a large second-order optical nonlinearity in soft glasses by poling. *Appl. Phys. Lett.*, 72(25): 3252–3254, 1998.

F.C. Garcia, L. Vogelaar, and R. Kashyap. Poling of a channel waveguide. *Optics Express*, 11(23):3041–3047, 2003.

A.S.L. Gomes, E.L. Falco Filho, C.B. de Arajo, D. Rativa, R.E. de Arajo, K. Sakaguchi, F.P. Mezzapesa, I.C.S. Carvalho, and P.G. Kazansky. Third-order nonlinear optical properties of bismuth-borate glasses obtained by conventional and thermally managed eclipse Z-scan. *J. Appl. Phys.*, 101(033115), 2007.

M. Guignard, V. Nazabal, J. Troles, F. Smektala, H. Zeghlache, Y. Quiquempois, A. Kudlinski, and G. Martinelli. Second-harmonic generation of thermally poled chalcogenide glass. *Opt. Express*, 13(3):789–795, 2005.

M. Guignard, V. Nazabal, J. Troles, F. Smektala, H. Zeghlache, Y. Quiquempois, A. Kudlinski, and G. Martinelli. High second-order nonlinear susceptibility induced in chalcogenide glasses by thermal poling. *Opt. Express*, 14(4):1524–1532, 2006.

K. Hagimoto and A. Mito. Determination of the second order susceptibility of ammonium dihydrogen phosphate and $\alpha$-quartz at 633 and 1064 $nm$. *Appl. Opt.*, 36(2): 8276–8282, 1995.

T.F. Heinz. *Nonlinear Surface Electromagnetic Phenomena*. Elsevier, Amsterdam, 1991.

N. Ho, J.M. Laniel, R. Vallee, and A. Villeneuve. Photosensitivity of $As_2S_3$ chalcogenide thin films at 1.5 $\mu m$. *Opt. Lett.*, 28(12):965–967, 2003.

S. K. Kurtz J. Jerphagnon. Maker fringe: a detailed comparison of theory and experiment for isotropic and uniaxial crystals. *J. Appl. Phys.*, 41(4):1667–1681, 1970.

W.D. Johnston. Oxidation-Reduction Equilibria in Molten $Na_2O - 2SiO_2$ Glass. *J. Am. Ceram. Soc.*, 48:184–190, 1965.

A. Kameyama, E. Muroi, A. Yokotani, K. Kurosawa, and P. Herman. X-ray radiation effects on second-harmonic generation in thermally poled silica glass. *J. Opt. Soc. Am. B*, 14(5):1088–1092, 1997.

A. Kameyama, A. Yokotani, and K. Kurosawa. Identification of defects associated with second-order optical nonlinearity in thermally poled high-purity silica glasses. *J. Appl. Phys.*, 89(9):4707–4713, 2001.

A. Kameyama, A. Yokotani, and K. Kurosawa. Generation and erasure of second-order optical nonlinearities in thermally poled silica glasses by control of point defects. *J. Opt. Soc. Am. B*, 19(10):2376–2383, 2002.

P.G. Kazansky, P.S.J. Russell, and H. Takebe. Glass fiber poling and applications. *J. Lightwave Tech.*, 15(8):14841493, 1997.

P.G. Kazansky and P.St.J. Russell. Thermally poled glass: Frozen-in electric field or oriented dipoles? *Opt. Commun.*, 110(2):611–614, 1994.

P.G. Kazansky, A.R. Smith, P.St.J. Russell, G.M. Yang, and G.M. Sessler. Thermally poled silica glass: laser induced pressure pulse probe of charge distribution. *Appl. Phys. Lett.*, 68(2):269–271, 1996.

J. Khaled, T. Fujiwara, M. Ohama, and A. J. Ikushima. Generation of second harmonics in Ge-doped $SiO_2$ thin films by ultraviolet irradiation under poling electric field. *J. Appl. Phys.*, 87(5):2137–2141, 2000.

L.L. Zhao K.L. Kelly, E. Coronado and G.C. Schatz. The optical properties of metal nanoparticles: The influence of size, shape, and dielectric environment. *J. Phys. Chem. B*, 107:668–677, 2003.

Y.N. Korkishko, V.A. Fedorov, and F. Laurell. The *shg*-response of different phases in proton exchanged lithium niobate waveguides. *IEEE Journal of Selected Topics in Quantum Electronics*, 6(1):132–142, 2000.

U. Kreibig and M. Vollmer. *Optical Properties of Metal Clusters*. Springer, Berlin, 1995.

A. Kudlinski, Y. Quiquempois, M. Lelek, H. Zeghlache, and G. Martinelli. Complete characterization of the nonlinear spatial distribution induced in poled silica glass with a submicron resolution. *Appl. Phys. Lett.*, 83(17):3623–3625, 2003a.

A. Kudlinski, Y. Quiquempois, H. Zeghlache, , and G. Martinelli. Evidence of second-order nonlinear susceptibility sign reversal in thermally poled samples. *Appl. Phys. Lett.*, 83(16):3242–3244, 2003b.

P. Laporta, S. Taccheo, S. Longhi, O. Svelto, and C. Svelto. Erbium-Ytterbium microlaser: optical properties and lasing characteristics. *Optical Materials*, 11, 1999.

A. LeCalvez, E. Freysz, and A. Ducasse. Second harmonic field generated in reflection by an inhomogeneous nonlinear polarization. *Opt. Commun.*, 145:135–140, 1997.

B. Lesche, F. C. Garcia, E. N. Hering, W. Margulis, I. C. S. Carvalho, and F. Laurell. Etching of silica glass under electric fields. *Physical Review Letters*, 78(11):2172–2175, 1997.

A.C. Liu, M.J.F. Digonnet, and G. S. Kino. Electro-optic phase modulation in a silica channel waveguide. *Opt. Lett.*, 19(7):466–468, 1994.

A.C. Liu, M.J.F. Digonnet, G.S. Kino, and E.J. Knystautas. Improved nonlinear coefficient (0.7 pm/V) in silica thermally poled at high voltage and temperature. *Electron. Lett.*, 36(6):555–556, 2000.

Q. Liu, F. Gan, X. Zhao, K. Tanaka, A. Narazaki, and K. Hirao. Second-harmonic generation in $Ge_{20}As_{25}S_{55}$ glass irradiated by an electron beam. *Opt. Lett.*, 26(17): 1347–1349, 2001.

E. Lopez-Lago, V. Couderc, L. Griscom, F.Smektala, and A. Barthelemy. All optical poling of a chalcohalogenide glass. *Optical Material*, 16:413–416, 2001.

S.A. Maier, M.L. Brongersma, P.G. Kik, S. Meltzer, A.A.G. Requicha, B.E. Koel, and H.A. Atwater. Plasmonics: Towards subwavelength optical devices. *Advanced Materials*, 13:1501–1505, 2001.

P.D. Maker, R.W. Terhune, R. Nisenhoff, and C.M. Savage. Effect of dispersion and focusing on the production of optical harmonics. *Phys. Rev. Lett.*, 8(1):21–22, 1962.

M. Mansuripur. Distribution of light at and near the focus of high-numerical-aperture objectives. *J. Opt. Soc. Am. A*, 3(12):2086–2093, 1992.

W. Margulis and F. Laurell. Interferometric study of poled glass under etching. *Opt. Lett.*, 21(21):1786–1788, 1996.

G. Martinelli, Y. Quiquempois, A. Kudlinski, and H. Zeghlache. Method to improve thermal poling efficiency in silica glasses. *Electron. Lett.*, 38(12):570–571, 2002.

C.J.S. Matos, I.C.S. Carvalho, E.F. da Silveira, W. Margulis, R.R. Pinho, and B. Lesche. Charge emission in thermal poling of glasses with carbon film anode. *J. Non-Cryst. Sol.*, 273:25–29, 2000.

F.P. Mezzapesa, I.C.S. Carvalho, C. Corbari, P.G. Kazansky, J.S. Wilkinson, and G. Chen. Voltage-assisted cooling: a new route to enhance $\chi^{(2)}$ during thermal poling. *Proc. CLEO*, 1(1):408–410, 2005.

F.P. Mezzapesa, I.C.S. Carvalho, P.G. Kazansky, O. Deparis, M. Kawazu, and K. Sakaguchi. Bleaching of sol-gel glass film with embedded gold nanoparticles by thermal poling. *Appl. Phys. Lett.*, 89(183121), 2006.

F.P. Mezzapesa, C. Corbari, O. Deparis, P.G. Kazansky, and J.S. Wilkinson. Second-order nonlinearity profile in thermally poled twin-hole fibre. *Proc. CLEO*, 2004.

A. Michie, I. Bassett, and J. Haywood. Electric field and voltage sensing using thermally poled silica fibre with a simple low coherence interferometer. *Meas. Sci. Technol.*, 17, 2006.

N. Mukherjee, R.A. Myers, and S.R.J. Brueck. Dynamics of second-harmonic generation in fused silica. *J. Opt. Soc. Am. B*, 11(4):665–669, 1994.

R.A. Myers, N. Mukherjee, and S.R.J. Brueck. Large second-order nonlinearity in poled fused silica. *Opt. Lett.*, 16(22):1732–1734, 1991.

N. Myren, H. Olsson, L. Norin, N. Sjodin, P. Helander, J. Svennebrink, and W. Margulis. Wide wedge shaped depletion region in thermally poled fiber with alloy electrodes. *Opt. Express*, 12(25):6093–6099, 2004.

A. Narazaki, K. Tanaka, and K. Hirao. Surface structure and second-order nonlinear optical properties of thermally poled $WO_3$-$TeO_2$ glasses doped with $Na^+$. *J. Opt. Soc. Am. B*, 19(1):54–62, 2002.

A. Narazaki, K. Tanaka, K. Hirao, and N. Soga. Induction and relaxation of optical second-order nonlinearity in tellurite glasses. *J. Appl. Phys.*, 85(4):2046–2051, 1999.

S. Ohara, N. Sugimoto, K. Ochiai, H. Hayashi, Y. Fukasawa, T. Hirose, and M. Reyes. Extra-broadband and highly efficient short length $Bi_2O_3$-based EDF. *Proc. OFC*, 2: 635–636, 2003.

A. Okada, K. Ishii, K. Mito, and K. Sasaki. Phase-matched second-harmonic generation in novel corona poled glass waveguides. *Appl. Phys. Lett.*, 60(23):2853–2855, 1992.

T.R. Oliveira, L. de S. Menezes, E.L. Falcao-Filho, A.S.L. Gomes, Cid B. de Arajo, K. Sakaguchi, F.P. Mezzapesa, I.C.S. Carvalho, and P. G. Kazansky. Optical limiting behavior of bismuth oxide-based glass in the visible range. *Appl. Phys. Lett.*, 89 (211912), 2006.

T. Ono and Anda K. Hirose. First-principles study on field evaporation for silicon atom on Si(001) surface. *J. Appl. Phys.*, 95(3):1568–1571, 2004.

U. Osterberg and W. Margulis. Dye-laser pumped by Nd-YAG laser-pulses frequency doubled in a glass optical fiber. *Opt. Lett.*, 11(8):516–518, 1986.

A. Ozcan, M. Digonnet, and G. Kino. Improved technique to determine second-order optical nonlinearity profiles using two different samples. *Appl. Phys. Lett.*, 84(5): 681–683, 2004a.

A. Ozcan, M. Digonnet, G. Kino, F. Ay, and A. Aydinli. Characterization of thermally poled germanosilicate thin films. *Opt. Express*, 12(20):4698–4708, 2004b.

A. Ozcan, M.J.F. Digonnet, and G.S. Kino. Inverse Fourier transform technique to determine second-order optical nonlinearity spatial profiles. *Appl. Phys. Lett.*, 82(9): 1362–1364, 2003.

J. Pedersen, R. Jacobsen, and M. Kristensen. Planar glass devices for efficient periodic poling. *Opt. Express*, 13(21):8514–8520, 2005.

A. Podlipensky, A. Abdolvand, G. Seifert, H. Graener, O. Deparis, and P.G. Kazansky. Dissolution of silver nanoparticles in glass through an intense dc electric field. *J. Phys. Chem. B*, 108, 2004.

V. Pruneri, G. Bonfrate, P. G. Kazansky, D. J. Richardson, N. G. Broderick, J. P. de-Sandro, C. Sommineau, P. Vidakovic, and J. A. Levenson. Greater than 20% efficient frequency doubling of 1532 $nm$ pulses in quasi-phase-matched germanosilicate fibres. *Opt. Lett.*, 24(3):208–210, 1999a.

V. Pruneri, F. Samoggia, G. Bonfrate, P.G. Kazansky, and G.M. Yang. Thermal poling of silica in air and under vacuum: The influence of charge transport on second harmonic generation. *Appl. Phys. Lett.*, 74(17):2423–2425, 1999b.

M. Qiu, T. Mizunami, Y. Takagagi, R. Vilaseca, and J. Martorell. Study of the second-order susceptibility from the cathode-side face of poled glasses. *J. Non-Cryst. Sol.*, 255(2–3):250–253, 1999a.

M. Qiu, Y. Takagaki, S. Egawa, T. Mizunami, and R. Vilaseca. Large second-order susceptibility generated in the cathodic face of silica by doping $F^-$ anions. *Opt. Commun.*, 172:97–101, 1999b.

M.X. Qiu, T. Mizunami, R. Vilaseca, F. Pi, and G. Orriols. Bulk and near-surface second-order nonlinearities generated in a BK7 soft glass by thermal poling. *J. Opt. Soc. Am. B*, 19(1):37–42, 2002.

Y. Quiquempois, N. Godbout, and S. Lacroix. Model of charge migration during thermal poling in silica glasses: Evidence of a voltage threshold for the onset of a SONL. *Phys. Rev. A*, 65(4):043816, 2002.

Y. Quiquempois, A. Kudlinski, and G. Martinelli. Zero-potential condition in thermally poled silica samples: evidence of a negative electric field outside the depletion layer. *J. Opt. Soc. Am. B*, 22(3):598–604, 2005a.

Y. Quiquempois, A. Kudlinski, G. Martinelli, W. Margulis, and I. C. S. Carvalho. Near-surface modification of the third-order nonlinear susceptibility in thermally poled Infrasil glasses. *Appl. Phys. Lett.*, 86(181106), 2005b.

Y. Quiquempois, G. Martinelli, P. Dutherage, P. Bernage, P. Niay, and M. Douay. Localisation of the induced second-order non-linearity within Infrasil and Suprasil thermally poled glasses. *Opt. Commun.*, 176(4–6):479–487, 2000a.

Y. Quiquempois, A. Villeneuve, D. Dam, K. Turcotte, J. Maier, G. Stegeman, and S. Lacroix. Second-order nonlinear susceptibility in $As_2S_3$ chalcogenide thin glass films. *Electron. Lett.*, 36(8):733–734, 2000b.

Y.T. Ren, C.J. Marckmann, J. Arentoft, and M.T. Kristensen. Thermally poled channel waveguides with polarization-independent electrooptic effect. *IEEE Phot. Tech. Lett.*, 14(5):639–641, 2002.

M. Sheik-Bahae, A.A. Said, T.H. Wei, D.J. Hagan, and E.W. Van Stryland. Sensitive measurements of optical nonlinearities using a single beam. *IEEE J. Quantum Electron.*, 26(4):760–769, 1990.

Y.R. Shen. *The principles of non-linear optics.* Wiley, New York, 1992.

J.E. Sipe. New Green-function formalism for surface optics. *J. Opt. Soc. Am. B*, 4(4): 481–489, 1987.

F. Smektala, C. Quemard, L. Leneindre, J. Lucas, A. Barthlmy, and C. De Angelis. Chalcogenide glasses with large non-linear refractive indices. *J. Non-Cryst. Sol.*, 239: 139–142, 1998.

G.I. Stegeman. *Nonlinear Optics of Organic Molecules and Polymers.* H.S. Nalva and S. Miyata Eds., CRC Press, Boca Raton, Fla., 1997.

R.H. Stolen and C. Lin. Self-phase-modulation in silica optical fibers. *Phys. Rev. A*, 17 (4):1448–1453, 1978.

R.H. Stolen and H.W.K. Tom. Self-organized phase-matched harmonic-generation in optical fibers. *Opt. Lett.*, 12(8):585–587, 1987.

N. Suarez and M. Puma. Aging effects in poly (DTH succinate) observed with thermal-stimulated polarization and depolarization experiments. *J. Appl. Polymer Science*, 69 (2):293–301, 1998.

N. Sugimoto, H. Kanbara, S. Fujiwara, K. Tanaka, Y. Shimizugawa, and K. Hirao. Third-order optical nonlinearities and their ultrafast response in $Bi_2O_3$-$B_2O_3$-$SiO_2$ glasses. *J. Opt. Soc. Am. B*, 16(11):1904–1908, 1999.

H. Takebe, P.G. Kazansky, P.S.J. Russell, and K. Morinaga. Effect of poling conditions on second-harmonic generation in fused silica. *Opt. Lett.*, 21(7):468–470, 1996.

K. Tanaka, A. Narazaki, and K. Hirao. Large optical second-order nonlinearity of poled $WO_3$-$TeO_2$ glass. *Opt. Lett.*, 25(4):251–253, 2000a.

K. Tanaka, A. Narazaki, Y. Yonezaki, and K. Hirao. Poling-induced structural change and second-order nonlinearity of $Na^+$-doped $Nb_2O_5$-$TeO_2$ glass. *J. Phys.: Condens. Matter*, 12(30):L513–L518, 2000b.

A.L.C. Triques, C.M.B. Cordeiro, V. Balestrieri, B. Lesche, W. Margulis, and I.C.S. Carvalho. Depletion region in thermally poled fused silica. *Appl. Phys. Lett.*, 76(18): 2496–2498, 2000.

T. Tsujino, M. Kawazu, and K. Maeda. Control of optical properties of thin films doped with au fine particles by the sol-gel method. *J. Sol-Gel Sci. Tech.*, 19:825–828, 2000.

R. Ulrich and R. Torge. Measurement of thin film parameters with a prism coupler. *Appl. Opt.*, 12(12):2901–2908, 1973.

G. Wallis and D.I. Pomerantz. Field assisted glass-metal sealing. *J. Appl. Phys.*, 40(10): 3946–3949, 1969.

Y.G. Xi, Z.L. Xu, Z.J. Hou, L.Y. Liu, L. Xu, W.C. Wang, M. Affatigato, and S. Feller. Second-order optical nonlinearity in bulk $PbO/B_2O3$ glass. *Opt. Commun.*, 210(3), 2002.

W. Xu, P. Blazkiewicz, D. Wong, S. Fleming, and T.Ryan. Specialty optical fibre for stabilising and enhancing electro-optic effect induced by poling. *Electron. Lett.*, 36 (15):1265–1266, 2000a.

Z.L. Xu, L.Y. Liu Y. Fei, P. Yang, Z.J Hou, L. Xu, W.C. Wang, J.W. Lim, M. Affatigato, and S. Feller. Nonuniform bulk second-order optical nonlinearity in $PbO/B_2O_3$ glass. *Appl. Phys. Lett.*, 77(1):70–72, 2000b.

S.P. Yawale and S.V. Pakade. DC conductivity and hopping mechanism in $Bi_2O_3 - B_2O_3$ glasses. *Journal of Materials Science*, 28(20):5451–5455, 1993.

A.V. Zayats and I. I. Smolyaninov. Near-field photonics: surface plasmon polaritons and localized surface plasmons. *Journal of Optics A: Pure and Applied Optics*, 5:S16–S50, 2003.